Ollscoil na hÉireann

The Operation of Multiquantum-Well Barriers

A thesis presented to
the
National University of Ireland
for the degree of
Doctor of Philosophy

by

Alan P. Morrison, B.E.

Supervised by: Dr J. D. Lambkin (NMRC)
Dr C. J. van der Poel (Philips Research Laboratories)

National Microelectronics Research Centre,
University College, Cork.

December 1996

Abstract

The multiquantum barrier (MQB), proposed by Iga *et al* in 1986, has been shown by several researchers to be an effective structure for improving the operating characteristics of laser diodes. These improvements include a reduction in the laser threshold current and increased characteristic temperatures. The operation of the MQB has been described as providing an increased barrier to electron overflow by reflecting high energy electrons trying to escape from the active region of the laser. This is achieved in a manner analogous to a Bragg reflector in optics. This thesis presents an investigation of the effectiveness of the MQB as an electron reflector. Numerical models have been developed for calculating the electron reflection due to a MQB. Novel optical and electrical characterisation techniques have been used to try to measure an increase in barrier height due to the MQB in AlGaInP. It has been shown that the inclusion of MQB structures in bulk double heterostructure visible laser diodes can halve the threshold current above room temperature and the characteristic temperature of these lasers can be increased by up to 20 K. These improvements are shown to occur in visible laser diodes even with the inclusion of theoretically ineffective MQB structures, hence the observed improvement in the characteristics of the laser diodes described above cannot be uniquely attributed to an increased barrier height due to enhanced electron reflection. It is proposed here that the MQB improves the performance of laser diodes by preventing the diffusion of zinc into the active region of the laser. It is also proposed that the trapped zinc in the MQB region of the laser diode locally increases the p-type doping bringing the quasi-Fermi level for holes closer to the valence band edge thus increasing the barrier to electron overflow in the conduction band.

This thesis is dedicated to the loving memory of my Mother, Anne.

Acknowledgements

I would like to thank Prof. G. T. Wrixon for making the facilities of the NMRC available to me throughout the course of this work and Prof. Liam Kelly for his support and encouragement throughout my time in the III-V Group. Special thanks must go to my thesis supervisor Dr John Lambkin for his unwavering support and for his ability to keep me on the straight and narrow. His supervision of this thesis is exemplary. It is difficult to express in words the debt of gratitude I owe to my co-supervisor Dr Carel van der Poel. Without the numerous discussions and thought provoking questions from him I don't think that this thesis would have progressed as far as it did. Extended thanks go to prof. dr Gerard Ackett and all the staff at Philips Optoelectronics Centre (POC) who made my stay there an enjoyable and productive one. People who deserve special mention from the POC include Ad Valster for growing all the n-i-n and laser samples described in this thesis, Jan de Poorter for numerous helpful discussions, Dr Leo Weegels for assistance with some of the laser measurements, A. J. Corbijn and A. A. Brouwer for fabricating the n-i-n and laser devices and of course Hans Lenssinck who was always on hand with a joke to lift the spirits when things were low.

Dr Stephen Fahy, Eoin O'Sullivan and Paul Tangney of the Physics Department at U.C.C. deserve many thanks for the hard work they put into developing the , $-X$ mixing and scattering models. Thanks to Liz Daly and Dr Ger O'Connor from U.C.G. for performing the PL measurements of Chapter 5.

I would like to thank Susan Walsh and Laurence Considine for growing many samples for me throughout the course of this work. I am also indebted for the phenomenal amount of help I've received from Nicolàs Cordero with all my modelling, postscript and computing problems. Thanks to Brian Corbett, Jules Braddell, Dave Mac and all the other staff of the III-V Group for making my time there a memorable one.

Where would I be without the empathy of my fellow students and friends, Oliver Gough, John Hayes and Áine Twomey. Thanks a million guys for all your help and encouragement. Thanks also to all the other postgrads, both past and present who have helped make my time as a student here a predominantly happy one, especially Flavio, Susan, Peter, JJ, Bill, Sean and Brendan.

I guess that the list of people I am indebted to is bounding on the infinite so in one stroke of the printer I'd like to thank anybody I've omitted to thank personally for all their help in the realisation of this thesis.

Finally, I'd like to thank my family for their unending patience and support and Moira for suffering through the completion of this thesis.

Publications and Presentations from this Work

Published Papers

- A. P. Morrison, J. D. Lambkin, C. J. van der Poel and A. Valster. *"Evaluation of Multiquantum Barriers in Bulk Double Heterostructure Visible Laser Diodes".* IEEE Photonics Technology Letters, Vol. 8, No. 7, pp. 849-851, July 1996.

- A. P. Morrison, J. D. Lambkin, E. O'Sullivan and S. Fahy. *"Simple Effective Mass Model to include the Effects of Gamma-X Mixing in Multiquantum Barriers".* Optical Engineering, Vol. 33, No. 12, pp. 3926-3930, Dec. 1994.

Published Conference Presentations

- A. P. Morrison, J. D. Lambkin, C. J. van der Poel and A. Valster. *"Performance of Multiquantum Barriers in Bulk Double Heterostructure Visible Laser Diodes as a Function of Temperature".* Paper CMN5 at Conference on Lasers and Electro-Optics Europe (CLEO), Congress Centrum Hamburg, Germany. 8-13 September 1996.

- J. D. Lambkin, A. P. Morrison, L. Considine, G. M. O'Connor, C. J. McDonagh, E. Daly and T. J. Glynn. *"Energy-Band Structure of Type I and Type II InGaP/InAlP Short Period Superlattices".* 22^{nd} International Conference on The Physics of Semiconductors, Volume 1, pp. 707-710, Vancouver, Canada. August 15-19, 1994.

Conference Presentations

- J. D. Lambkin, A. P. Morrison, C. J. van der Poel and A. Valster. *"Multiquantum Barriers in Bulk Double Heterostructure Visible Laser Diodes".* Post-deadline paper at 20^{th} Workshop on Compound Semiconductor Devices and Integrated Circuits (WOCSDICE), Vilnius, Lithuania, May 1996.

- A. P. Morrison, J. D. Lambkin, E. O'Sullivan and S. Fahy. *"Design of a Multiquantum Barrier using an Extended Effective Mass Model to include the effects of Gamma-X Mixing".* Proceedings of the 18^{th} European Workshop on Compound Semiconductor Devices and Integrated Circuits (WOCSDICE), Kinsale, Ireland. pp. 91, May 1994.

- J. D. Lambkin, A. P. Morrison, L. Considine, G. M. O'Connor and C. J. McDonagh. *"Energy-Band Structure of Type I and Type II InGaP/InAlP Short Period Superlattices".* Proceedings of the 18^{th} European Workshop on Compound Semiconductor Devices and Integrated Circuits (WOCSDICE), Kinsale, Ireland. pp. 91, May 1994.

- A. P. Morrison, J. D. Lambkin, L. Considine, S. Walsh and W. M. Kelly. *"Development of 634nm Laser Diodes for Optical Storage Applications".* Irish Optoelectronics Group Annual Meeting, Trinity College, Dublin. 12/13 May 1994.

Papers Submitted for Publication

- A. P. Morrison, L. Considine, S. Walsh, N. Cordero, J. D. Lambkin, G. M. O'Connor, E. M. Daly, T. J. Glynn and C. J. van der Poel. *"Photoluminescence Investigation of the Carrier Confining Properties of Multiquantum Barriers".* Submitted for publication in IEEE J. Quantum Electronics.

Papers in Preparation

- A. P. Morrison, J. D. Lambkin, C. J. van der Poel and A. Valster. *"Measuring the , $-X$ Transition in AlGaInP using n-i-n Diodes".* In preparation.

- A. P. Morrison, J. D. Lambkin, C. J. van der Poel and A. Valster. *"Electron Transport in n-i-n Diodes with AlGaInP Intrinsic Barriers".* In preparation.

- A. P. Morrison, J. D. Lambkin, C. J. van der Poel and A. Valster. *"Systematic Measurement of the Barrier Height of the Multiquantum Barrier Intrinsic Region in AlGaInP n-i-n Diodes".* In preparation.

Glossary of Abbreviations and Symbols in the Text

CCD	charge coupled device
CD	compact disc
CW	continuous wave
DH	double heterostructure
DVD	digital versatile disc
DVD-RAM	digital versatile disc random access memory
E_{fn}	quasi-Fermi level for electrons
E_{fp}	quasi-Fermi level for holes
F-N	Fowler-Nordheim
FWHM	full width at half maximum
I-V	current-voltage
LD	laser diode
LED	light emitting diode
L-I	light-current
LO	longitudinal optical
MBE	molecular beam epitaxy
MOVPE	metal organic vapour phase epitaxy
MQB	multiquantum barrier
MQW	multiquantum well
P-F	Poole-Frenkel
PL	photoluminescence
PLE	photoluminescence excitation
SADP	selected area diffraction pattern
SMASH	strain-modulated aperiodic superlattice heterobarrier
SQW	single quantum well
TE	thermionic emission
TEM	transmission electron microscopy
TISE	time independent Schrödinger equation
T_0	characteristic temperature
VCSEL	vertical cavity surface emitting laser
WKB	Wannier-Kronig-Brillouin

Chapter 1

λ	wavelength

Chapter 2

g	modal gain
J	current density
γ	optical confinement factor
h	active layer thickness
A	gain coefficient
J_0	transparency current density
T_0	characteristics temperature

Chapter 3

V(x)	potential barrier
$\Psi(x)$	1-D electron wavefunction
m	electron mass
$\hbar$	Planck's constant divided by 2π
E	electron energy
k	wave vector
x	position
A, B	wave amplitudes in the +x direction
A', B'	wave amplitudes in the -x direction
V_0	height of potential step/barrier
q	electron charge
m^*	electron effective mass
T	transmission coefficient
R	reflection coefficient
l	width of potential barrier
T_{n-1}	transfer matrix for an n-layer barrier system

Chapter 4

ΔE_C	conduction band offset
ΔE_V	valence band offset
m_0	free electron mass

Δ	mixing parameter
α	scattering parameter
r	reflected fraction of wavefunction amplitude
t	transmitted fraction of wavefunction amplitude
n_0	electron population
n	portion of electron population not scattered
λ	mean free path of electron

Chapter 5

T	absolute temperature
I_0	initial light intensity
I_{PL}	photoluminescence intensity
k	Boltzmann's constant
E_A, E_B	activation energies for mechanisms A and B
C_A, C_B	ratio of 4.2 K radiative lifetime to high temperature non-radiative lifetime for mechanisms A and B

Chapter 6

Δ^*	apparent barrier height
F	electric field
f(E,T)	Fermi distribution
T(E)	tunnelling probability
N_D	electron density in conduction band
v_n	electron thermal velocity
A^*	effective Richardson constant
N_T	density of defects in a given thickness w of a barrier
e_n	electron emission rate from defect to barrier conduction band
E_i	trap ionisation energy
σ	electron capture cross section
N_C	density of states in barrier conduction band
E_{i0}	defect ionisation energy under zero field
ϵ	dielectric constant

Contents

Chapter 1

Introduction

1.1 Motivation and Objectives

Laser diodes emitting in the visible region of the electromagnetic spectrum are of major importance due to their large application base in areas such as high density optical storage [1], bar code readers [2], scanners, laser printers [3], short haul communications [4, 5], replacements for He-Ne gas lasers [6] and head-up displays. There is a significant commercial demand for lasers emitting at increasingly short wavelengths, to take advantage of the reduced diffraction limited spot-size. For example, lasers for use with audio compact discs (CDs) emit at a wavelength of 780 nm. These lasers use established AlGaAs technology and are both cheap and reliable in performance. On the other hand, the next generation of laser diodes for optical storage emit at 650 nm. The reduced wavelength allows a higher density of information to be stored on an optical disc than its audio CD counterpart. The principal difference between these two laser types is the semiconductor material used in their manufacture. The 780 nm lasers are made from AlGaAs which is incapable of reaching the short wavelengths required by the new commercial optical storage standards. The recently announced Digital Versatile Disc (DVD) optical storage system employs both the advantages of a short laser diode wavelength (λ=650 nm) and new ways of compressing digital information to give up to a 14 fold increase in disc capacity when compared to the conventional CD-format. A natural extension, to be expected in the near future, would be write/erasable DVD (DVD-RAM) versions demanding high power output at 650 nm. To reach wavelengths below 700 nm the lasers are fabricated using the $(Al_xGa_{1-x})_{0.5}In_{0.5}P$ quaternary alloy. Lasers emitting at 650 nm have been commercially available for several years now and the technology has matured sufficiently that these lasers are now capable of operating at high powers (>50 mW). [6]

It is expected that future generations of optical storage standards will call for even shorter wavelengths, with 630 nm being the current commercial goal. Unfortunately

$(Al_xGa_{1-x})_{0.5}In_{0.5}P$ lasers suffer from increasingly poor thermal characteristics as the wavelength is reduced. [3] These poor characteristics manifest themselves as increased threshold current densities, lower characteristic temperatures and higher leakage currents and all of these have been attributed to the relatively small conduction band offset of the $Ga_xIn_{1-x}P$ / $(Al_xGa_{1-x})_{0.5}In_{0.5}P$ heterojunction [3, 7], although it has also been proposed that leakage of holes over the smaller valence band offset is a major contributor to the leakage current. [8] The practical implication of this is the inability to make high power, high temperature 630 nm laser diodes. To overcome this deficiency, at least in the conduction band, Iga *et al* [9] proposed a novel confinement structure known as a multiquantum barrier (MQB). The MQB is designed to enhance the barrier in the conduction band by reflecting high energy electrons in a manner analogous to the reflection of photons by an optical Bragg reflector. This is achieved by the constructive interference of the electron wavefunctions in a superlattice region while loss of low energy electrons is prevented by means of a thick (> 150 Å) anti-tunnelling layer. Any improved carrier confinement would not only improve the high temperature performance of these lasers but also their degradation behaviour, both by decreasing the operating current densities at elevated temperature and suppressing the injection of hot electrons into the p-type cladding region. [10]

Several groups have already demonstrated an improvement in the operating characteristics of visible laser diodes with the inclusion of MQB structures. [1, 6, 11, 12, 13, 14, 15] The improvement in performance is invariably attributed to the MQB producing a virtual barrier, although the work of Rennie *et al* [16] as well as the work presented here, shows that the measured barrier height is typically much less than the theoretically predicted value. [13, 16] It is also difficult to uniquely attribute the improvements in laser diode performance to the MQB producing an increased barrier height. Laser diodes are very complex structures and the inclusion of any additional structure (such as a MQB) in the p-cladding of the laser could significantly alter its performance characteristics. It is therefore important to investigate the MQB effect by using simple test structures to probe the theory of Iga *et al* and test its validity.

The aims of this thesis are to investigate the leakage mechanisms in red lasers, to experimentally evaluate MQBs in a systematic way and to test the validity of the MQB concept as proposed by Iga. To achieve these aims numerical models were developed to study the design and operation of MQB structures in AlGaInP. Using this software, MQB structures were designed and investigated using optical (photoluminescence) and electrical (measurement of the barrier heights in n-i-n diodes) characterisation techniques. Finally the operation of MQB structures in bulk double heterostructure visible laser diodes has been demonstrated and an explanation of the role of the MQB in improving laser performance is proposed.

1.2 Thesis Outline

In Chapter 2 the semiconductor laser is introduced with particular emphasis on the difficulties associated with poor electrical confinement within the active region. Techniques described in the literature for improving the electrical confinement in visible laser diodes are reviewed. The MQB is highlighted as a successful structure for improving the thermal characteristics of visible laser diodes. In addition, methods for measuring the barrier height improvement due to a MQB in laser diodes are discussed.

Chapter 3 presents a qualitative description of the MQB operation. The theory of quantum mechanical reflection and transmission for both a potential step and a single barrier system is described. This provides the necessary background for progressing to the more complicated multi-barrier model where the idealised effective mass model used by Iga for calculating multi-barrier transmission is explained.

In Chapter 4 the limitations of Iga's model are outlined and two new models which extend the simple model used by Iga are presented. These models overcome the limitations of the single conduction band approximation and qualitatively illustrate the effects of scattering within the semiconductor on the performance of a MQB. Using these models, different aspects of MQB design such as the influence of , $-X$ mixing, variations in structural parameters due to growth fluctuations and uncertainty variations in electron effective mass are investigated. Extracts from this chapter have been published in Optical Engineering [17] and presented at both the 18^{th} European Workshop on Compound Semiconductor Devices and Integrated Circuits [18] and the 22^{nd} International Conference on the Physics of Semiconductors. [19]

A photoluminescence (PL) investigation of the carrier confining properties of MQB structures is presented in Chapter 5. The PL measurements are taken over a range of temperatures from 4K to 300K and Arrhenius plots are used to determine the thermal activation energies of electrons escaping from a quantum well over both a bulk barrier and over a MQB. Extracts from this chapter have been submitted for publication in the IEEE Journal of Quantum Electronics. [20]

The electron transport over a variety of different barrier types is examined in Chapter 6. From measurements of the I-V characteristics of n-i-n diodes between 60K and 300K the transport mechanisms across both bulk and MQB barriers are determined along with measurements of the barrier height derived from activation energies extrapolated from the experimental data. The work presented in this chapter is novel in that it is the first time that such measurements have been presented for AlGaInP and also the first time a systematic approach has been presented to measure the barrier height of MQB structures. Three papers are in preparation from the work summarised in this chapter. [21, 22, 23]

The effect of incorporating MQB structures into simple bulk double heterostructure

laser diodes is the subject of Chapter 7. The threshold current as a function of temperature from 70K to 350K is measured for three lasers each having the same optical confinement in the active region. The cladding region of each however, consists of a bulk barrier, an optimised MQB structure and a *leaky* MQB structure respectively. A relative comparison is made between the devices in terms of characteristic temperature (T_0), activation energy and threshold current. Extracts from the work presented in this chapter have appeared in IEEE Photonics Technology Letters [13] and have been presented at the 20^{th} Workshop on Compound Semiconductor Devices and Integrated Circuits [24] and the IEEE/IOP Conference on Lasers and Electro-Optics Europe. [25] Some novel aspects to the MQB lasers presented in this chapter include ensuring a constant optical confinement in all the lasers, reversing the MQB from its normal orientation and leaving the MQB structures nominally undoped.

In Chapter 8 the conclusions of the thesis are presented along with suggested areas of future work to build on the work performed here.

Chapter 2

AlGaInP for Visible Laser Diodes

2.1 Introduction

This chapter describes the operating principles of bulk double heterostructure lasers. The technological limitations of AlGaInP are discussed and the techniques used to overcome these limitations are presented. The MQB is shown to be a very effective structure for improving the operating characteristics of laser diodes in general and AlGaInP lasers in particular. The theory of the MQB is explained, however convincing experimental evidence of the MQB effect (a virtual increase in the barrier height due to constructive interference of the electron wavefunction) has yet to be presented in the literature.

2.2 Double Heterostructure (DH) Lasers

2.2.1 Principle of Operation

The main requirements for lasing in a compound semiconductor such as AlGaInP are a direct bandgap (i.e. the conduction band minimum and the valence band maximum occur at the same position in k-space), a population inversion and a means of optical feedback. [26] The population inversion in a DH semiconductor laser is provided by the injection of carriers in a forward biased p-n junction. The electrons in the conduction band are confined to the intrinsic active region by means of a p-doped cladding layer which has a band-gap that is wider than that of the active region. Similarly the holes are confined to the active region by means of an n-doped cladding layer.

The spontaneous recombination of electrons and holes in the intrinsic active region of the diode with the emission of a photon can result in two further processes. These

processes are absorption, where the photon produced promotes an electron in the valence band of the semiconductor to the conduction band, and stimulated emission, where an electron-hole pair is stimulated to recombine producing a photon that is of the same phase and frequency as the photon which stimulated the recombination. [27] The process of stimulated emission provides the necessary gain to support lasing action. Optical feedback is also required to generate sufficient optical flux density in the active region so that stimulated emission becomes the dominant recombination mechanism. This feedback is provided by placing the gain region in a Fabry-Perot resonator formed from partially reflecting mirrors which are made by cleaving atomically flat planes at either end of the optical cavity. The reflectance of this semiconductor/air interface is $\sim$0.32. The onset of lasing is determined by the condition that the round-trip gain in the laser cavity must exceed the losses. The injection current density at which the round-trip gain overcomes the losses is known as the threshold current density of the laser. This is one of the most important characteristic parameters that define the laser's performance. The spectral output from the device changes from broad-band incoherent spontaneous emission below threshold to sharp coherent peaks of laser radiation above threshold. The emission wavelength is essentially determined by the bandgap of the material in the active region of the laser, although the emission wavelength also varies with injection current density and cavity length.

2.2.2 AlGaInP DH Lasers

For light emission at visible wavelengths the material used is AlGaInP. This material has the widest direct bandgap of all the III-V semiconductors (apart from the nitride compounds) and is suitable for fabricating lasers in the 600-700 nm range. [14, 28] A typical schematic of an AlGaInP laser's epitaxial structure is shown in Fig. 2.1. In this

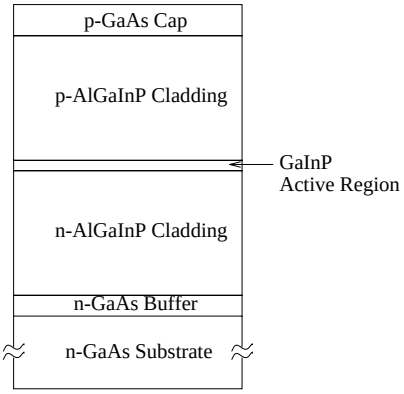

Figure 2.1: Layer structure of a typical AlGaInP double heterostructure laser diode.

device, under forward bias conditions, (see Fig. 2.2) electrons from the n-type material

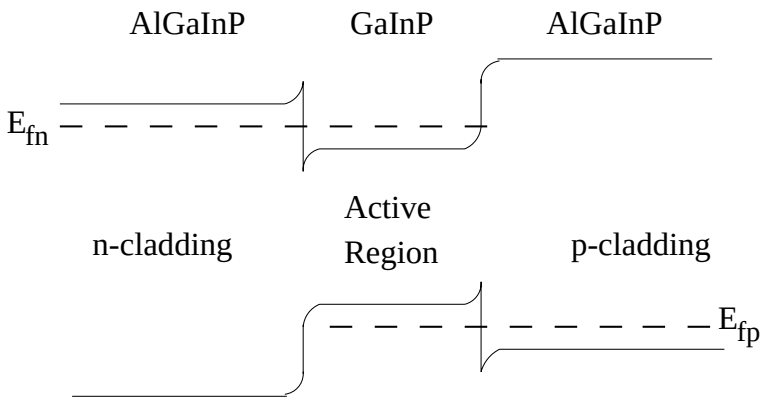

Figure 2.2: Schematic band-structure under forward bias of an AlGaInP/GaInP Bulk DH laser diode.

and holes from the p-type material are injected into the GaInP active region. In this region, at low bias, the electrons and holes recombine spontaneously with the emission of photons. These photons create more electron-hole pairs through absorption and the emission of further photons in phase and of the same frequency by stimulated emission. When the injected carrier density is sufficiently high (i.e. when a population inversion has been reached) stimulated emission is the dominant emission process and the diode is said to be lasing.

At low drive current densities (J), the modal gain (g) versus current relationship for DH lasers is given by

$$g = \left(\frac{\gamma}{h}\right) A(J - J_0),$$

where γ is the optical confinement factor, h is the active layer thickness, A is a gain coefficient and J_0 is the transparency current density. [29] The optimum active layer thickness in GaInP/AlGaInP DH lasers is that for which the modal gain is the greatest, and occurs when the quantity γ/h is maximised. The AlGaInP cladding region of the laser has a lower refractive index than the active region. This refractive index change confines most of the generated optical field to the active region in a similar way to the confinement of light within the core of an optical fibre by its cladding material. This waveguiding effect ensures that the optical flux density in the active region is sufficient to sustain the stimulated emission.

Once the active region thickness is fixed, achieving adequate carrier confinement becomes crucial to optimising the performance of AlGaInP DH lasers. The AlGaInP cladding regions provide the necessary barriers to confine the electrons and holes to the active region ensuring that a population inversion can be achieved. It has been

extensively reported that the small height of the AlGaInP/GaInP heterobarrier is the source of several problems in the operation of this type of visible laser. [3, 30, 31, 32] These problems include large threshold current densities, poor temperature performance and increased threshold current densities with reducing wavelength. [3] Carrier leakage over the heterobarrier (see Fig. 2.3) is reported to be the major loss mechanism in these lasers. This is generally attributed to leakage of electrons, although hole leak-

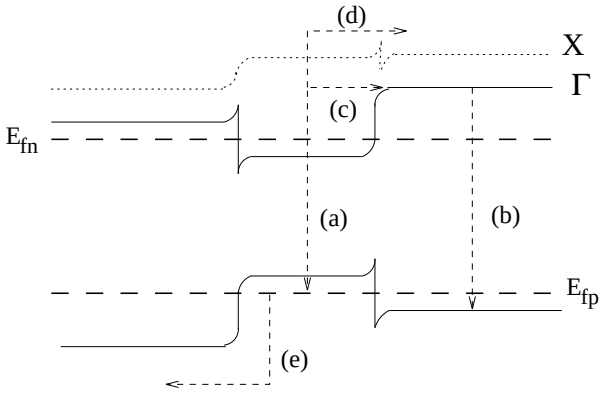

Figure 2.3: Diagram showing the possible current paths in bulk DH AlGaInP laser diodes: (a) Radiative Recombination (b) , Barrier Recombination (c) Leakage into , Barrier (d) Leakage into X Barrier and (e) Leakage of holes.

age has also been noted as a significant leakage mechanism. [8] Recently Smowton and Blood [4] have established that electron leakage into the X-minima is also a major loss mechanism because of the proximity of the X-minima and , -minimum at aluminium compositions around 50%.

In laser diodes efficient carrier confinement is characterised by a high characteristic temperature (T_0), which indicates that the thermal energy is insufficient to excite a large fraction of carriers over the confinement barrier. [29] A high T_0 also indicates low levels of non-radiative recombination, such as Auger recombination and intervalence band absorption[1], which is often a very temperature sensitive carrier loss mechanism. Typical T_0 values for AlGaInP DH lasers lie in the range T_0 = 80-140 K. [29] However, the T_0 value does not remain constant over large ranges of temperature. In general there are two distinct characteristic temperatures with the T_0 value decreasing at elevated temperatures, usually between 20 and 80°C. This behaviour is attributed to the leakage of electrons over the heterobarrier, which increases rapidly with temperature, and reduces T_0. Although there are several leakage mechanisms working simultaneously in AlGaInP laser diodes, a significant effort has been put into reducing the electron

[1] These are not significant in visible laser diodes because the split-off valence bandgap ($\Delta_0 \sim 0.1$ eV) is much smaller than the direct bandgap energy ($E_\Gamma \sim 1.9$ eV) [31]

leakage over the cladding barrier in the conduction band. This is the leakage mechanism that will be given the most attention in this thesis. The techniques described in the literature for suppressing electron leakage are outlined in the next section.

2.2.3 Techniques for Suppressing Electron Leakage in Laser Diodes

The performance of DH lasers has been improved by increasing the doping in the p-cladding layer which reduces both the electron leakage current and the series resistance. [31] Fig. 2.4 shows schematic energy band diagrams of an AlGaInP DH laser

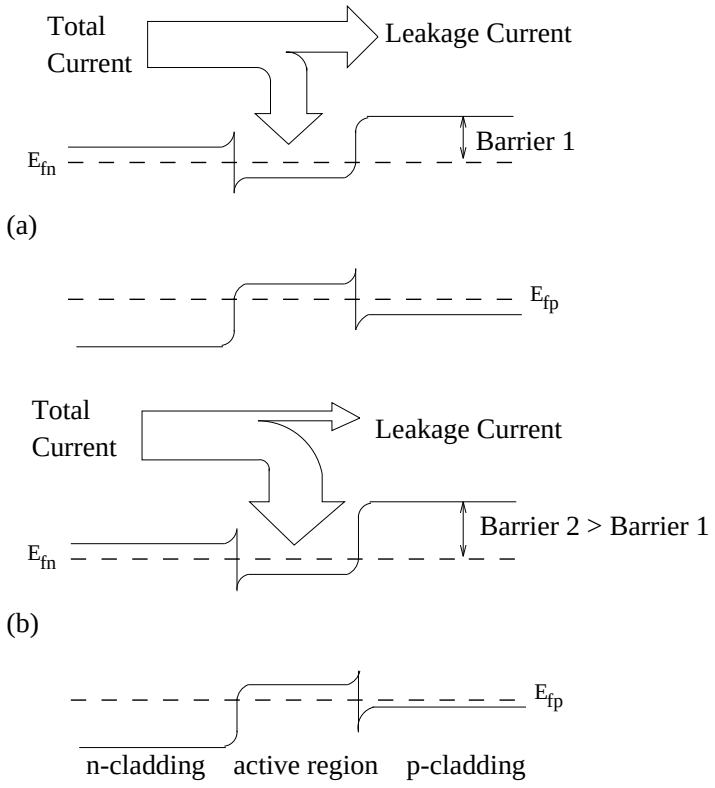

Figure 2.4: Diagram showing the effect of high p-type doping on electron confinement in AlGaInP lasers. (a) normal p-doping, (b) high p-doping.

with (a) low and (b) high p-type doping. When the p-cladding layer is highly doped, the Fermi level on the p-cladding side moves towards the valence band. This causes an increase in the heterobarrier between the active layer and the p-cladding layer in the conduction band, thus reducing the electron overflow. [33, 34]

The use of misoriented substrates in the growth of visible lasers has also yielded improved device performance. Watanabe *et al* [2] show that by using a (100) GaAs substrate misoriented 15^o towards the [011] direction the maximum continuous wave (CW) operating temperature was increased by 10^oC for a multiquantum well (MQW)

laser operating at 632 nm. The improvement is attributed to an increased bandgap of the cladding material due to the suppression of sublattice ordering and improved MQW heterointerfaces. The increased bandgap of the cladding helps to reduce carrier leakage over the barrier. Hamada *et al* [35] explain that the use of (100) GaAs substrates with a misorientation of 5–7^o towards the [011] direction increases the bandgap of the AlGaInP layers by 50–60 meV and also enables a doubling of the maximum p-carrier concentration. Here the combined effect of a larger barrier to carrier overflow in conjunction with the effects of higher p-doping contributes to the improved temperature characteristics of 660 nm lasers. Other groups that have reported improved temperature characteristics and reduced threshold current densities with the use of misoriented substrates include Tanaka *et al* [36], Nakano *et al* [37] and Kikuchi *et al* [38].

The most successful attempts at realising high temperature and short wavelength operation in AlGaInP lasers use a multiquantum barrier in the p-cladding region of the laser. This is shown schematically in Fig. 2.5. The MQB works by behaving like a Bragg

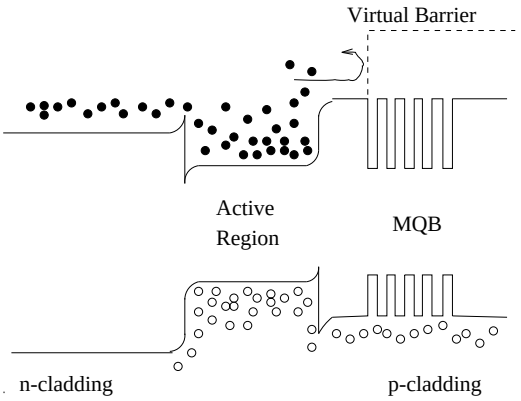

Figure 2.5: Schematic representation of the effect of including a MQB in the p-cladding of a DH laser.

reflector for electrons and in doing so produces a virtual barrier that is higher than the intrinsic barrier in the cladding region. The MQB concept was originally proposed by Iga *et al* as a means of increasing the barrier height of the laser diode cladding region. [9] Esaki and Tsu's study of the properties of superlattices [39, 40] led Iga *et al* to propose that a suitably designed superlattice in series with a thick ($>$ 150 Å) anti-tunnelling layer would produce a forbidden zone above the highest point of the barrier where the electron could not exist. The width of this forbidden zone appears as a virtual barrier to the electron and the intrinsic barrier appears to be increased in height equal to the width of the forbidden zone. [41] There have been several reports of large improvements in the operating characteristics of laser diodes by including a MQB in the p-cladding region of the laser [1, 6, 12, 11, 14, 42] and these improvements have not been limited

to visible laser diodes. For example, Fukushima *et al* [11] have demonstrated a larger characteristic temperature and slope efficiency in 1.55 μm strained GaInAs/AlGaInAs quantum well lasers when MQBs are used. However, the increase in characteristic temperature is less than 10^{o}C. Takagi *et al* [12] have shown that the inclusion of a MQB in a GaAs/AlGaAs DH laser can improve the characteristic temperature by as much as 54^{o}C and halve the threshold current when compared to bulk lasers. In visible lasers the improvement in operating characteristics is also dramatic. Kishino *et al* [14] report a threshold current density reduction from 1.2 kA/cm^2 to 0.84 kA/cm^2 when a MQB was used in a 660 nm GaInP/AlInP laser. The high temperature characteristic temperature also showed an increase of 26^{o}C in comparison with a bulk DH reference laser. Rennie *et al* [1] use a MQB to shorten the room temperature CW operating wavelength of an AlGaInP MQW laser to 625 nm, while Shono *et al* [6] have made use of both misoriented substrates and MQBs to give sufficient electrical confinement to allow high power (40 mW CW) operation in 630 nm strained QW AlGaInP laser diodes. Although the reported improvements in laser performance are large, there is no quantifiable measure of the barrier height improvement due to the MQB in these lasers. Several attempts have been made to verify the MQB effect by trying to show an increase in barrier height due to the presence of a virtual barrier. These experiments are discussed in the next section.

2.3 Verifying the MQB effect

As discussed in the previous section when a MQB is incorporated into the cladding region of a diode laser it can significantly improve its operating characteristics. However, there is no direct means of measuring the barrier height improvement due to the MQB in these devices and hence no direct way of verifying the MQB effect. The various techniques for trying to measure the barrier height improvement due to the MQB are discussed in this section.

2.3.1 Photoluminescence Investigation of MQB's

Takagi *et al* [43, 44] claim to have experimentally measured the effect of electron-wave confinement of a GaAs/AlGaAs MQB. In their work they have tried to observe the effect of the MQB by evaluating the photoluminescence (PL) peak intensity from a quantum well sandwiched between an $Al_{0.7}Ga_{0.3}As$ barrier and an $Al_{0.5}Ga_{0.5}As$ barrier layer. The photoexcited carriers should escape over the $Al_{0.5}Ga_{0.5}As$ barrier layer, so the PL intensity from the quantum well should reflect the amount of overflowing electrons (hole leakage is considered negligible). The MQB is evaluated by comparing the PL peak intensities from the quantum well of two samples with and without a MQB in the $Al_{0.5}Ga_{0.5}As$ barrier layer. Both the excitation power dependence of the

PL intensity from 100 mW to 1W and the temperature dependence from 20°C to 160°C at an excitation power of 500 mW from the 488 nm line of an Ar^+ laser are examined. From these experiments an increase in PL intensity of about one order of magnitude for the sample with the MQB and an 8°C increase in characteristic temperature was measured. There is no reported direct measurement of any barrier height improvement and hence no direct verification of the MQB effect.

A similar experimental approach is taken in this work where the normalised PL intensity is measured as a function of temperature from 4 K to 300 K. The differences between Takagi's approach and the approach taken in this work are the use of resonant excitation from a dye laser (Rhodamine 3-G) in addition to 488 nm excitation and Arrhenius plots to directly determine the thermal activation energy of carriers escaping from quantum well. Additionally, MQBs are placed on either side of the MQB to ensure that that barrier height is the same on either side of the quantum well. This has its own associated problems which will be discussed in Chapter 5.

2.3.2 Comparison of MQB and Bulk Barriers using n-i-n Diodes

The method most frequently described in the literature for attempting to verify the MQB effect is a comparison between the I-V characteristics of n-i-n diodes with bulk and MQB intrinsic regions. This method was first employed by Takagi *et al* [45, 46] where the current-voltage characteristics for n-GaAs/i-barrier/n-GaAs diodes were measured. The i-barrier in that work was either bulk AlGaAs or a GaAs/AlGaAs MQB. The measurements were made at 77 K and the characteristics were compared with theoretical I-V characteristics obtained using a WKB [2] approximation. However, this model is invalid for electron energies in excess of the barrier height in the intrinsic region [47] which diminishes any interpretation that can be obtained from using it. The interpretation that was made was that the n-i-n diode with the MQB intrinsic region improves the barrier height by 80 meV. This result was obtained by matching the measured I-V characteristic to one simulated using the WKB approximation. This is a poor comparison since the WKB approximation is invalid over this energy range. In their analysis Takagi *et al* also point to the higher turn-on voltage for the diode with the MQB intrinsic region as evidence for an increased barrier height due to the MQB although no quantitative measure of the barrier height was provided.

Yen *et al* [48, 49] have also attempted to show the barrier height improvement due to MQBs in n-i-n diodes made from GaAs/AlGaAs. In their analysis they conclude that an increased turn-on voltage in the diode with a MQB intrinsic region is evidence of the MQB effect. They also conclude that for indirect barriers the X-minima play a significant role in blocking electron transport over the barrier. However, the signif-

[2] Wentzel-Kramers-Brillouin approximation.

icance of this work is that the authors highlight a major discrepancy in the design of MQBs used in laser structures fabricated by different research groups. They note that two different research groups report visible laser diodes which both show improved characteristics due to the inclusion of MQB structures. Each group used different effective mass values to design their MQBs and if either group's design is simulated with the other group's effective mass values, the design is rendered ineffective as an electron reflector. However, when these MQB designs are included in a laser the characteristics of the laser improve in both cases.

The analysis used in the cases described above is extremely qualitative and fails to provide a direct measure of the barrier height produced by the MQB and thus fails to verify the MQB effect.

In Chapter 6 the I-V characteristics of AlGaInP n-i-n diodes as a function of temperature from 60 K to 300 K are presented. This data allows the thermionic emission energies of electrons transported over the barrier to be experimentally established and hence the barrier height can be quantitatively measured. This is the first time this sort of analysis has been applied to AlGaInP to try to verify the MQB effect.

2.3.3 Double Active Region Light Emitting Diode

Rennie *et al* [16] use a novel technique for measuring the excess barrier height induced by a MQB in a double active region light-emitting diode (LED). The increase in barrier height due to the MQB is measured to be between 26 and 55 meV depending on the first barrier or anti-tunnelling layer thickness. The technique employed to measure the barrier height involves using a surface emitting LED with two active regions separated by a barrier. This is shown in Fig. 2.6. The first active region has a smaller bandgap than the second active region to prevent absorption of the emission from the first active region. The overflow current from the first active region is expected to reach the second active region and recombine emitting light of a different wavelength. The relative output from each active region can be measured from the LED output spectrum. The ratio of the output from the second active region to the first active region is a measure of the overflow (leakage) current. The amount of overflow current can be altered by changing the ambient temperature or the injected current. An estimate of the barrier height is thus obtained from the amount of overflow current. This analysis demonstrated that further consideration of the MQB theory was necessary due to the large discrepancy between experimental results and theoretical predictions.

2.4 Summary

Both optical and electrical confinement are necessary for the efficient operation of laser diodes. Poor confinement leads to lowered characteristic temperatures and increased

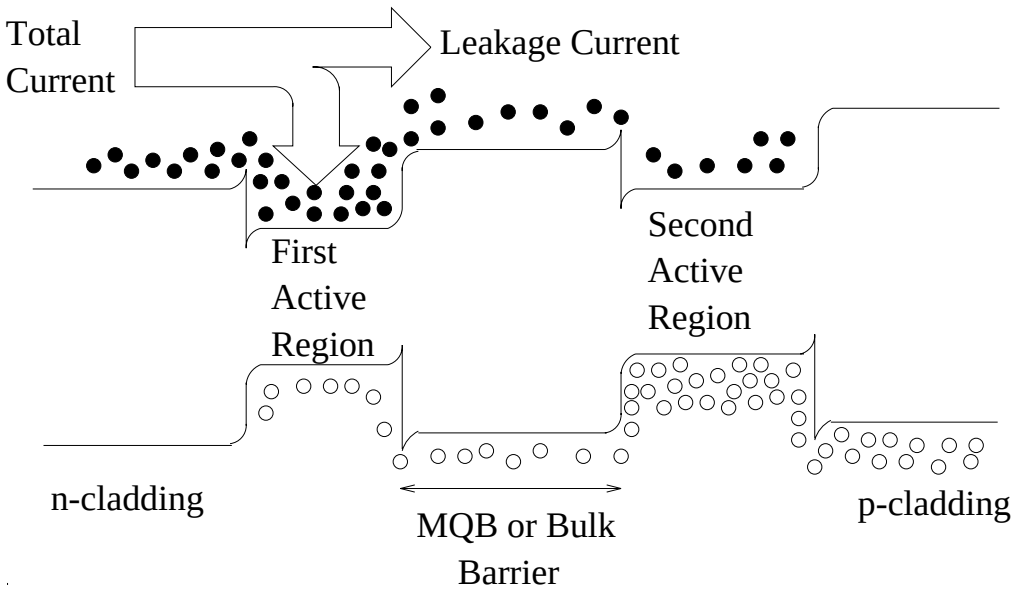

Figure 2.6: Energy band schematic of the double active region LED used by Rennie *et al.*

threshold current densities in lasers. In AlGaInP visible laser diodes electron leakage over the barrier in the conduction band has been shown to be a major loss mechanism. Other loss mechanisms include loss of electrons to the X-minima in the conduction band and loss of holes in the valence band. Techniques that have been used to suppress electron leakage in laser diodes include increased p-doping in the p-cladding of the laser; the use of misoriented substrates to suppress sublattice ordering; and the use of MQBs to provide a virtual barrier to carrier overflow. The MQB has been highlighted for successfully improving the characteristics of laser diodes, yet experimental evidence of the MQB effect has not been convincingly presented in the literature. Attempts to confirm the MQB effect of an increased virtual barrier have included comparative photoluminescence studies of samples with MQBs and bulk barriers; comparison of the I-V characteristics of n-i-n diodes with both MQB and bulk intrinsic regions; and the use of a double active region LED to measure the leakage current across either a MQB or bulk barrier separating the active regions. All of the above techniques have been described in this chapter and it was found that only the double active region LED experiment had provided any quantitative measurement of the barrier height. None of the techniques evaluated provided convincing proof of the MQB effect and Rennie *et al* have suggested that the operation of the MQB needs to be reconsidered given the large differences between theoretically predicted barrier heights and those measured experimentally with the double active region LED.

Chapter 3

Theory of Multiquantum Barriers

3.1 Introduction

In this chapter the calculation of reflection and transmission coefficients for a single barrier system is explained. This calculation is then extended to include the multi-barrier transmission formalism used by Iga, following the effective mass approximation. A simple qualitative explanation of the MQB operation is given and different aspects of MQB design are discussed.

3.2 Transmission through and Reflection from Potential Steps and Barriers

In the case of a square potential barrier, $V(x)$ is a constant function $V(x) = V$ in a certain region of space. The time independent Schrödinger equation (TISE) in one dimension may be written

$$\frac{d^2\Psi(x)}{dx^2} + \frac{2m}{\hbar^2} \cdot (E - V) \cdot \Psi(x) = 0 \tag{3.1}$$

where $\Psi(x)$ is the electron wavefunction, m is the electron mass, $\hbar$ is Planck's constant divided by 2π, E is the electron energy and V is the constant potential. [50] When this is true there are three cases to consider.

1. When the electron energy is greater than the potential ($E > V$). In this instance by making the substitution $k^2 = \frac{2m}{\hbar^2}(E - V)$ the solution to Eqn 3.1 can be written

$$\Psi(x) = Ae^{jkx} + A'e^{-jkx} \tag{3.2}$$

where A is the amplitude of the wave travelling to the right in the positive x direction and A' is the amplitude of the wave travelling in the opposite direction. The wave-vector k is given by $\frac{\sqrt{2m(E-V)}}{\hbar}$.

2. When the electron energy is less than the potential ($E < V$). By making the substitution $V - E = (\hbar^2\rho^2)/(2m)$ allows the solution to Eqn 4.2 to be written

$$\Psi(x) = Be^{\rho x} + B'e^{-\rho x}. \tag{3.3}$$

3. When the electron energy is equal to the potential height ($E = V$). This is a special case where $\Psi(x)$ is a linear function of x.

These states in a square potential can be determined by writing the applicable solution to the TISE (either Eqn 3.2 or Eqn 3.3) in all regions where $V(x)$ is constant. These solutions are then matched at the points where $V(x)$ is constant by requiring continuity of $\Psi(x)$ and $\frac{1}{m}\frac{d\Psi(x)}{dx}$. If the particle mass is assumed to be the same in the well and the barrier then the matching condition at the boundary can be relaxed to $\frac{d\Psi(x)}{dx}$. This is assumed to be the case in developing the single barrier models but the mass is introduced again for the multibarrier model since the effective mass of the electron is different in the well and barrier materials.

3.2.1 Potential Steps

The procedure outlined in the previous section is now applied to a potential step to determine the reflection and transmission coefficients. This situation is very similar to that encountered by electrons in the active region of a double heterostructure laser when they are trying to cross the potential step provided by the cladding region. A representation of this situation is shown in Fig. 3.1. There are two cases to consider. The first of these is when the electron energy, E, is greater than the height of the potential step, V_0. Classical mechanics predicts that a particle (electron) of energy $E > V_0$ should be 100% transmitted, quantum mechanics on the other hand predicts that under the condition $E > V_0$ some reflection can occur.

When $E > V_0$. In Region I

$$k_1 = \sqrt{\frac{2mE}{\hbar^2}}$$

and in Region II

$$k_2 = \sqrt{\frac{2m(E - V_0)}{\hbar^2}}.$$

In Region I TISE has the solution

$$\Psi_1(x) = A_1 e^{jk_1 x} + A_1' e^{-jk_1 x}$$

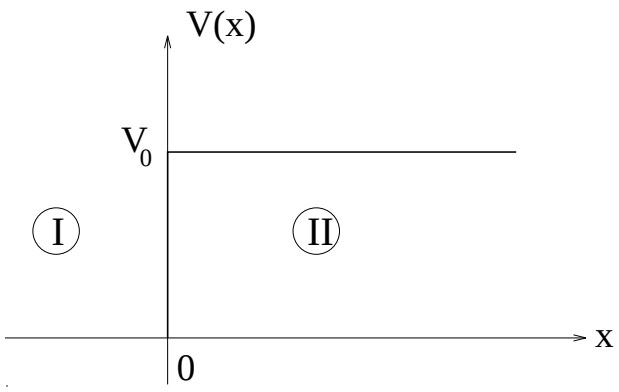

Figure 3.1: Potential step of height V_0.

and in Region II

$$\Psi_2(x) = A_2 e^{jk_2 x} + A_2' e^{-jk_2 x}.$$

By choosing $A_2' = 0$ the incident particle can only come from $x = -\infty$. Matching across the interface implies

$$\Psi_1(x) = \Psi_2(x) \ @ \ x = 0$$

$$\Rightarrow \ A_1 + A_1' = A_2$$

$$\left.\frac{d\Psi_1}{dx}\right|_{x=0} = jk_1 A_1 - jk_1 A_1'$$

$$\left.\frac{d\Psi_2}{dx}\right|_{x=0} = jk_2 A_2$$

$$\frac{d\Psi_1}{dx} = \left.\frac{d\Psi_2}{dx}\right|_{x=0} \Rightarrow \ jk_1 A_1 - jk_1 A_1' = jk_2 A_2$$

$$\therefore \ jk_1(A_1 - A_1') = jk_2(A_1 + A_1')$$

$$\Rightarrow \ k_1 - k_2 = (k_1 + k_2)\frac{A_1'}{A_1}$$

$$\frac{k_1 - k_2}{k_1 + k_2} = \frac{A_1'}{A_1}$$

Also,

$$k_1 A_1 - k_1 A_1' = k_2 A_2$$

$$\Rightarrow \ k_1 A_1 - k_1(A_2 - A_1) = k_2 A_2$$

$$2k_1 A_1 = (k_1 + k_2)A_2$$

$$\therefore \frac{2k_1}{(k_1+k_2)} = \frac{A_2}{A_1}$$

The transmission coefficient for the barrier is given by the ratio of the transmitted probability current density to the incident probability current density while the reflection coefficient is given by the ratio of the reflected probability current density to the incident probability current density. The probability current density J can be calculated from the wavefunction using [50, 51]

$$J = \frac{-jq\hbar}{2m^*}\langle(\nabla\Psi)^*\Psi - \Psi^*(\nabla\Psi)\rangle \tag{3.4}$$

If the wavefunction is given by $\Psi = Ae^{jkx}$ then

$$J = \frac{-jq\hbar}{2m^*}(-2jk|A|^2)$$

which can be reduced to

$$J = \frac{-q\hbar k}{m^*}|A|^2 \equiv \textit{Probability Current Density.} \tag{3.5}$$

For current conservation to apply the sum of the transmission coefficient and reflection coefficient must be unity. Therefore the transmission coefficient is given by

$$T = \frac{k_2}{k_1}\left|\frac{A_2}{A_1}\right|^2$$

$$\therefore T = \frac{k_2}{k_1}\left(\frac{2k_1}{(k_1+k_2)}\right)^2$$

$$\Rightarrow T = \frac{4k_1k_2}{(k_1+k_2)^2}$$

and since $R+T=1 \Rightarrow R = 1-T$ and

$$R = 1 - \frac{4k_1k_2}{(k_1+k_2)^2}$$

It is useful to note here that both T and R remain unchanged if k_1 and k_2 are interchanged i.e. if the particle is incident from the other side of the barrier.

The second case to consider is when the electron energy is less than that of the potential step i.e. $E < V_0$.

When $E < V_0$. In Region I

$$k_1 = \sqrt{\frac{2mE}{\hbar^2}}$$

and

$$\Psi_1(x) = A_1e^{jk_1x} + A_1'e^{-jk_1x}$$

In Region II

$$\rho_2 = \sqrt{\frac{2m(V_0 - E)}{\hbar^2}}$$

$$\Psi_2(x) = B_2 e^{\rho_2 x} + B_2' e^{-\rho_2 x}$$

For the solution to remain bounded as $x \to \infty \Rightarrow B_2 = 0$. Matching:

$$\Psi_1(x)|_{x=0} = \Psi_2(x)|_{x=0}$$

$$\Rightarrow A_1 + A_1' = B_2'$$

$$\left.\frac{d\Psi_1(x)}{dx}\right|_{x=0} = \left.\frac{d\Psi_2(x)}{dx}\right|_{x=0}$$

$$\Rightarrow jk_1 A_1 - jk_1 A_1' = -\rho_2 B_2'$$

$$\therefore jk_1 A_1 - jk_1 A_1' = -\rho_2 A_1 - \rho_2 A_1'$$

$$\Rightarrow \frac{A_1'}{A_1} = \frac{jk_1 + \rho_2}{jk_1 - \rho_2} = \frac{k_1 - j\rho_2}{k_1 + j\rho_2}$$

Since the reflection coefficient, R, is given by $\left|\frac{A_1'}{A_1}\right|^2$

$$R = \left|\frac{A_1'}{A_1}\right|^2 = \left|\frac{k_1 - j\rho_2}{k_1 + j\rho_2}\right|^2 = 1 \; (Total\ Reflection)$$

A plot of electron reflection as a function of energy for a potential step with V_0=0.17 eV is shown in Fig. 3.2. From this plot there is no observed transmission up to the energy of the step height. At energies above the step height there is only a small probability that the electron is reflected. The probability of reflection from the step decreases rapidly with increasing electron energy above the barrier energy.

3.2.2 Potential Barrier

After the potential step the next most complicated structure to be considered is the potential barrier. It is more complicated than the case described in the previous section because there are three regions to consider and furthermore the incoming particle has a finite probability of tunnelling through the potential barrier, depending on its thickness. This is the situation encountered in n-i-n tunnel diodes, for example. A schematic representation of a potential barrier of width l and height V_0 is given in Fig. 3.3. There are again two cases to consider, each with three regions.

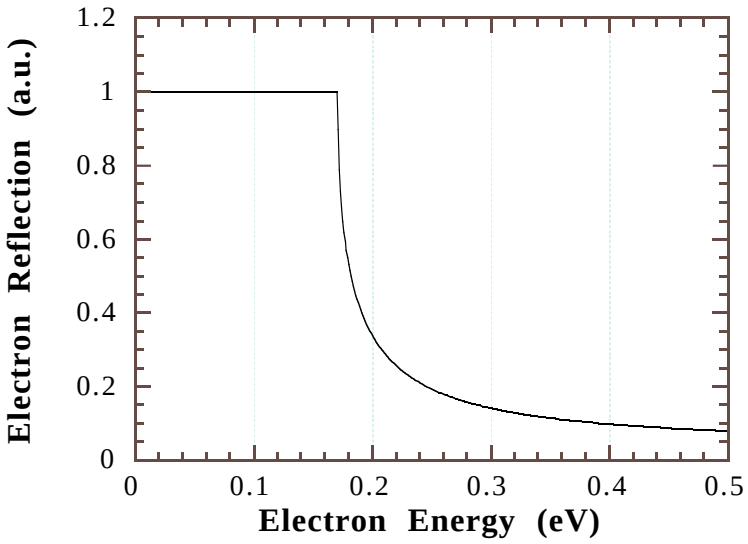

Figure 3.2: Electron reflection from a potential step of height 170 meV.

The first case is when $E > V_0$. The three regions to be examined are

$$I.\ x < 0$$
$$II.\ 0 < x < l$$
$$III.\ x > l$$

The solutions to the TISE for each of the three regions and their associated wave vectors are

$$\Psi_1(x) = A_1 e^{jk_1 x} + A_1' e^{-jk_1 x} \ \ with\ k_1 = \sqrt{\frac{2mE}{\hbar^2}}$$

$$\Psi_2(x) = A_2 e^{jk_2 x} + A_2' e^{-jk_2 x} \ \ with\ k_2 = \sqrt{\frac{2m(E-V_0)}{\hbar^2}}$$

$$\Psi_3(x) = A_3 e^{jk_3 x} + A_3' e^{-jk_3 x} \ \ with\ k_3 = \sqrt{\frac{2mE}{\hbar^2}}$$

If $A_3' = 0$, this means that the particle is coming from $x = -\infty$. Matching both the wavefunctions and their derivatives at $x = l$ gives

$$\Psi_2(x)|_{x=l} = \Psi_3(x)|_{x=l}$$

$$\Rightarrow\ A_2 e^{jk_2 l} + A_2' e^{-jk_2 l} = A_3 e^{jk_3 l} \tag{3.6}$$

$$\left.\frac{d\Psi_2(x)}{dx}\right|_{x=l} = \left.\frac{d\Psi_3(x)}{dx}\right|_{x=l}$$

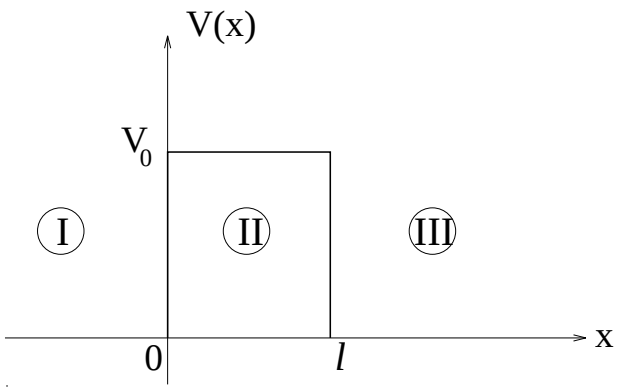

Figure 3.3: Potential barrier of width l and height V_0.

$$\Rightarrow \; jk_2A_2e^{jk_2l} - jk_2A_2'e^{-jk_2l} = jk_3A_3e^{jk_3l} \tag{3.7}$$

Match at $x = 0$

$$\Psi_1(x)|_{x=0} = \Psi_2(x)|_{x=0}$$

$$\Rightarrow \; A_1 + A_1' = A_2 + A_2' \tag{3.8}$$

$$\left.\frac{d\Psi_1(x)}{dx}\right|_{x=0} = \left.\frac{d\Psi_2(x)}{dx}\right|_{x=0}$$

$$\Rightarrow \; jk_1A_1 - jk_1A_1' = jk_2A_2 - jk_2A_2' \tag{3.9}$$

Equations 3.6 and 3.7 are solved simultaneously giving

$$A_2 = -\frac{k_3 + k_2}{k_3 - k_2}A_2'e^{-2jk_2l}$$

Substituting this back into Eqn 3.6 yields

$$-\frac{k_3 + k_2}{k_3 - k_2}A_2'e^{-jk_2l} + A_2'e^{-jk_2l} = A_3e^{jk_3l}$$

$$\Rightarrow A_2' = \frac{A_3e^{jk_3l}e^{jk_2l}}{1 - \frac{k_3+k_2}{k_3-k_2}}$$

Now from Eqn 3.8 and the solution for A_2

$$A_1 + A_1' = \left[1 - \frac{k_3 + k_2}{k_3 - k_2}e^{-2jk_2l}\right]A_2'$$

$$\Rightarrow A_1 + A_1' = \left[\frac{(k_3 - k_2) - (k_3 + k_2)e^{-2jk_2l}}{(k_3 - k_2)}\right]\left[\frac{A_3e^{jk_3l}e^{jk_2l}(k_3 - k_2)}{k_3 - k_2 - k_3 - k_2}\right]$$

This can be reduced to

$$A_1 + A_1' = (\cos k_2 l - j\frac{k_3}{k_2}\sin k_2 l)e^{jk_3 l}A_3$$

From Eqn 3.9 and the solution for A_2

$$k_1 A_1 - k_1 A_1' = -k_2\frac{k_3 + k_2}{k_3 - k_2}A_2' e^{-2jk_2 l} - k_2 A_2'$$

Substituting for A_2' gives

$$k_1 A_1 - k_1 A_1' = \left[-k_2\frac{k_3 + k_2}{k_3 - k_2}e^{-2jk_2 l} - k_2\right]\left[\frac{A_3 e^{jk_3 l}e^{jk_2 l}(k_3 - k_2)}{-2k_2}\right]$$

Further algebraic manipulation yields

$$k_1 A_1 - k_1 A_1' = \left[k_3 A_3 e^{jk_3 l}\cos k_2 l - jk_2 A_3 e^{jk_3 l}\sin k_2 l\right]$$

$$Now\ A_1' = -A_1 + (\cos k_2 l - j\frac{k_3}{k_2}\sin k_2 l)e^{jk_3 l}A_3$$

$$\Rightarrow\ k_1 A_1 - k_1\left[-A_1 + (\cos k_2 l - j\frac{k_3}{k_2}\sin k_2 l)e^{jk_3 l}A_3\right] = k_3 A_3 e^{jk_3 l}\cos k_2 l - jk_2 A_3 e^{jk_3 l}\sin k_2 l$$

And hence

$$A_1 = \left(\cos k_2 l - j\left(\frac{k_1^2 + k_2^2}{2k_1 k_2}\right)\sin k_2 l\right)e^{jk_1 l}A_3 \tag{3.10}$$

Also

$$A_1 = -A_1' + (\cos k_2 l - j\frac{k_3}{k_2}\sin k_2 l)e^{jk_3 l}A_3$$

and similar manipulation shows that

$$A_1' = j\left(\frac{k_2^2 - k_1^2}{2k_1 k_2}\right)\sin k_2 l e^{jk_1 l}A_3 \tag{3.11}$$

The reflection from the barrier will be a function of the left travelling wave in Region I and the right travelling wave in Region I. Hence,

$$\frac{A_1'}{A_1} = \frac{j\left(\frac{k_2^2 - k_1^2}{2k_1 k_2}\right)\sin k_2 l e^{jk_1 l}A_3}{\left(\cos k_2 l - j\left(\frac{k_1^2 + k_2^2}{2k_1 k_2}\right)\sin k_2 l\right)e^{jk_1 l}A_3}$$

$$\Rightarrow\ \frac{A_1'}{A_1} = \frac{j(k_2^2 - k_1^2)\sin k_2 l}{2k_1 k_2\cos k_2 l - j(k_1^2 + k_2^2)\sin k_2 l}$$

From this the reflection coefficient is defined as

$$R = \left|\frac{A_1'}{A_1}\right|^2 = \frac{-(k_2^2 - k_1^2)^2 \sin k_2 l^2}{4k_1^2 k_2^2 \cos k_2 l^2 + (k_1^2 + k_2^2)^2 \sin k_2 l^2 - 4jk_1 k_2 (k_1^2 + k_2^2) \cos k_2 l \sin k_2 l} \tag{3.12}$$

Similarly an expression for the transmission coefficient can be obtained by considering the amplitude of the right travelling wave in Region III and the amplitude of the right travelling wave in Region I. The case for when the electron energy is less than the barrier energy is approached in the same manner as described above. This calculation results in large algebraic expressions for both the reflection and transmission coefficients. A plot of the electron reflection as a function of electron energy for a single 350 Å potential barrier of height 0.17 eV is shown in Fig. 3.4. As in the case of the potential step, there is no transmission through the barrier for electrons with energies less than the barrier height. At energies above the barrier height the reflection is given by a damped oscillation. The period of the oscillation is not constant but increases with increasing electron energy.

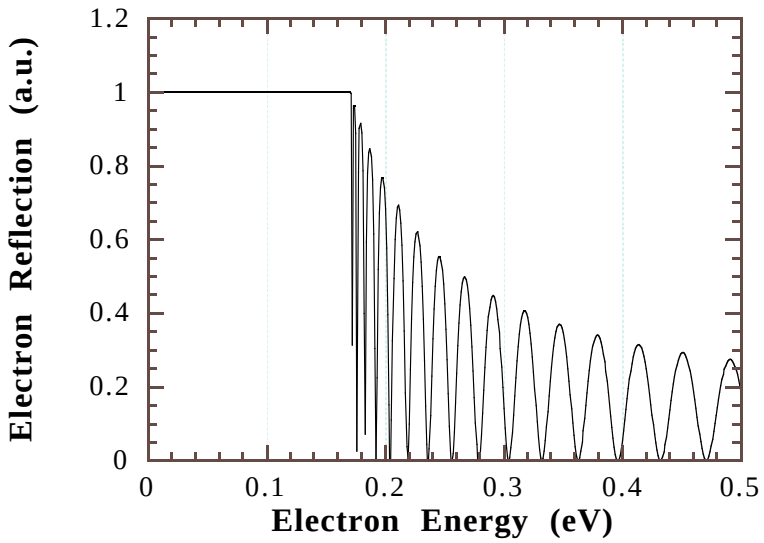

Figure 3.4: Electron reflection from a single bulk barrier 350Å thick and 170meV high.

This section has illustrated the complexity of the calculations required to determine the reflection coefficients for a single barrier. The situation becomes more complicated as more and more barriers are added so advantage is made of the iterative nature of the problem. This is discussed in more detail with the outline of the model in the next section where matrix methods are used for matching the solutions at each interface.

3.3 Multibarrier Transmission Model

To generalise the results from the single barrier case described in the previous section and to include the conservation of probability current density, the matching conditions at the interface between the $(n-1)^{th}$ and the n^{th} region at a distance $x = a$ are

$$\Psi_{n-1} \mid_{x=a} = \Psi_n \mid_{x=a}$$

and

$$\left.\frac{1}{m^*_{n-1}}\frac{d\Psi_{n-1}}{dx}\right|_{x=a} = \left.\frac{1}{m^*_n}\frac{d\Psi_n}{dx}\right|_{x=a}$$

where m^*_{n-1} is the electron effective mass in the $(n-1)^{th}$ layer. A representation of this situation is shown in Fig. 3.5.

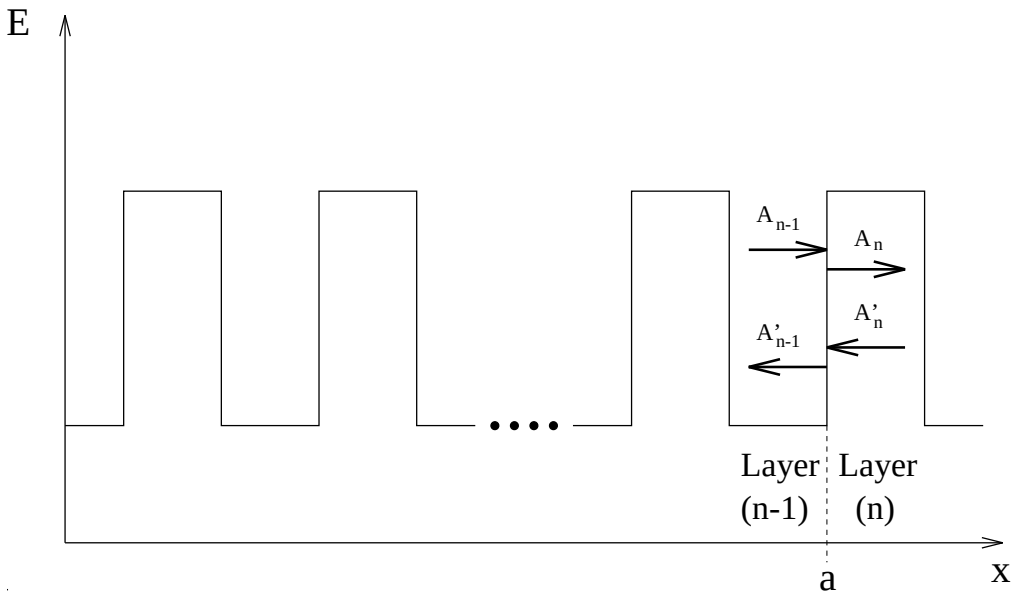

Figure 3.5: Matching of wavefunction amplitudes at the $(n-1)^{th}$ and the n^{th} interfaces at a distance $x = a$ into the semiconductor.

Explicitly these matching equations are

$$A_{n-1}e^{jk_{n-1}a} + A'_{n-1}e^{-jk_{n-1}a} = A_n e^{jk_n a} + A'_n e^{-jk_n a} \tag{3.13}$$

and

$$A_{n-1}\frac{jk_{n-1}}{m^*_{n-1}}e^{jk_{n-1}a} - A'_{n-1}\frac{jk_{n-1}}{m^*_{n-1}}e^{-jk_{n-1}a} = A_n\frac{jk_n}{m^*_n}e^{jk_n a} - A'_n\frac{jk_n}{m^*_n}e^{-jk_n a} \tag{3.14}$$

These equations can be written in matrix form

$$\begin{pmatrix} e^{jk_{n-1}a} & e^{-jk_{n-1}a} \\ \frac{jk_{n-1}}{m^*_{n-1}}e^{jk_{n-1}a} & -\frac{jk_{n-1}}{m^*_{n-1}}e^{-jk_{n-1}a} \end{pmatrix} \begin{pmatrix} A_{n-1} \\ A'_{n-1} \end{pmatrix} = \begin{pmatrix} e^{jk_n a} & e^{-jk_n a} \\ \frac{jk_n}{m^*_n}e^{jk_n a} & -\frac{jk_n}{m^*_n}e^{-jk_n a} \end{pmatrix} \begin{pmatrix} A_n \\ A'_n \end{pmatrix} \tag{3.15}$$

If the 2×2 matrix on the left hand side of the above equation is termed L_{n-1} and the 2×2 matrix on the right hand side is termed L_n then the amplitudes of the waves on the left of the n^{th} interface can be written in terms of those on the right as

$$\tilde{A}_{n-1} = L^{-1}_{n-1} L_n \tilde{A}_n \tag{3.16}$$

The matrix $L^{-1}_{n-1} L_n$ is the transfer matrix T_{n-1} across interface n at position $x = a$ in the system of layers. Therefore

$$\tilde{A}_{n-1} = T_{n-1} \tilde{A}_n \tag{3.17}$$

Successive applications of this equation for each interface of the multi-barrier region results in a relation between the amplitudes of the wavefunctions which describe the electron on one side of the multi-barrier system to those on the other side. The transfer matrix for the entire system is then the matrix product of all the individual transfer matrices for each layer, i.e.

$$\tilde{A}_1 = T_1 T_2 T_3 \ldots T_{n-1} \tilde{A}_n \tag{3.18}$$

The matrix product $T_1 T_2 T_3 \ldots T_{n-1}$ may be denoted by the system transfer matrix, T, where

$$T = \begin{pmatrix} t_{11} & t_{12} \\ t_{21} & t_{22} \end{pmatrix} \tag{3.19}$$

For the particular case of electron injection in the active region of a semiconductor laser it is assumed that no electrons enter the MQB system from the right hand side and hence $A'_n = 0$. This situation is illustrated in Fig. 3.6. The matrix relating the input wave amplitudes to the output wave amplitudes may thus be written

$$\begin{pmatrix} A_1 \\ A'_1 \end{pmatrix} = \begin{pmatrix} t_{11} & t_{12} \\ t_{21} & t_{22} \end{pmatrix} \begin{pmatrix} A_n \\ 0 \end{pmatrix} \tag{3.20}$$

Multiplying out the above equation gives

$$A_1 = t_{11} A_n$$

$$A'_1 = t_{21} A_n$$

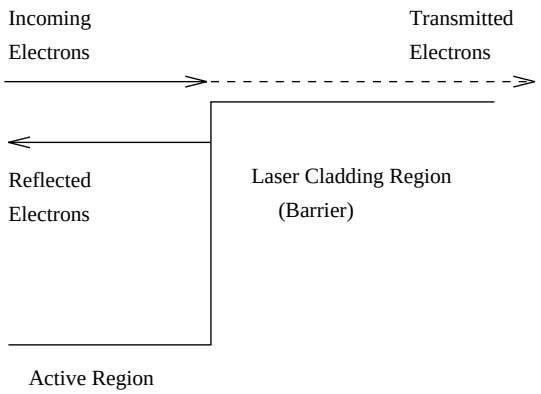

Figure 3.6: Schematic of a step barrier in a semiconductor laser where electrons can only enter from the left hand side.

and from Eqn 3.5

$$R = \frac{J_{refl}}{J_{inc}} = \left|\frac{A_1'}{A_1}\right|^2$$

$$T = \frac{J_{trans}}{J_{inc}} = \left|\frac{A_n}{A_1}\right|^2 \frac{k_n m_1^*}{k_1 m_n^*}$$

The electron reflection from a two barrier system is shown in Fig. 3.7. The barrier heights are again 0.17 eV and each barrier is 50 Å thick, separated in space by a 50 Å well. From this figure it is clear that the reflection drops to below 0.1 at an energy of approximately 165 meV. The number of oscillations is reduced in comparison with the single barrier case and the average reflectivity at electron energies greater than the barrier height is increased. This increased reflectivity is due to constructive interference between the electron wavefunctions oscillating between the barrier interfaces. An additional two 50 Å barriers have been added to the previous two barrier system to produce the electron reflection plot shown in Fig. 3.8. It can be noted from this figure that additional barriers tend to increase the average reflection at electron energies above the barrier height. The width of these high energy reflection peaks can be tailored by changing the thickness of the well/barrier pairs. The ability to design a multi-barrier system that increases the reflection of electrons with energies greater than the intrinsic barrier height is the fundamental requirement of a successful design.

From the above analysis, the reflection and transmission coefficients for any multi-barrier system can be calculated numerically. This model has some limitations and these will be discussed in the next chapter.

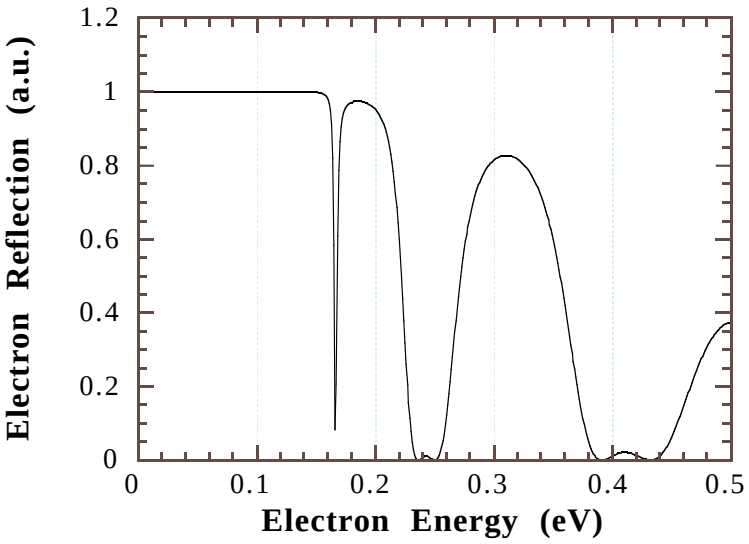

Figure 3.7: Electron reflection from two barriers each 50 Å thick and separated in space by a 50 Å well. The potential height of the barriers is 170 meV.

3.4 Qualitative Description of MQB Operation

The superlattice portion of the MQB may be described qualitatively in an analogous fashion to the Bragg reflector in optics. Varying the thickness of the wells and barriers in the superlattice changes the resonance condition for constructive interference of the electron wavefunction and hence the energy range over which a high reflection can be obtained. Having a large difference in effective mass between the well and barrier materials is advantageous because it allows the design of an efficient reflector with a smaller number of well/barrier periods. [52] In this sense the electron effective mass is analogous to the refractive index of an optical Bragg reflector.

In the superlattice, due to the formation of miniband states, there is a high probability that electrons of lower energies, resonant with the superlattice miniband, can tunnel through the structure and lose the benefit of increased reflection at higher electron energies. Iga predicted this effect and realised that for the MQB to be effective a thick barrier had to be placed in series with the superlattice to prevent the tunnelling of low energy electrons. The thickness of this layer has to be larger than the tunnelling range of the electron. A schematic picture of such a structure is given in Fig. 3.9 (a).

Another useful interpretation of the MQB principle is given by Salzman *et al* [53] and is illustrated in Fig. 3.9 (b). This picture of the MQB shows that in the superlattice, a series of minibands, or allowed states, is established. By varying the thickness of the well and barrier materials as well as the effective masses in these regions (by using

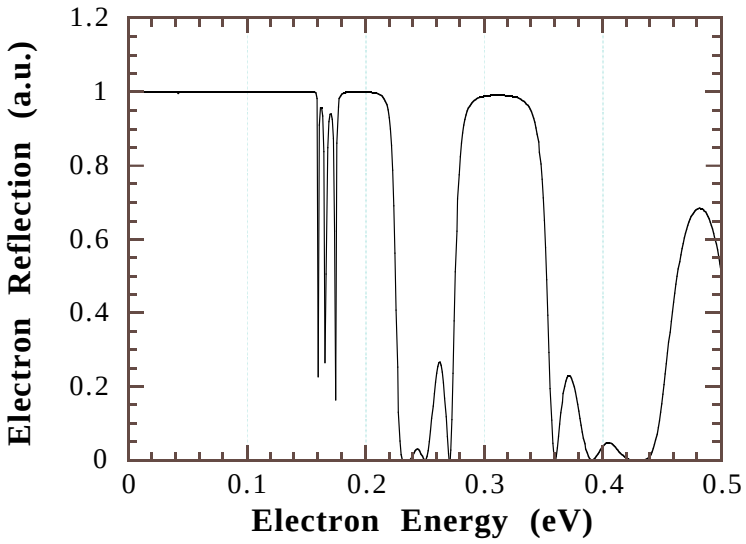

Figure 3.8: Electron reflection from a multi-barrier system consisting of four 50 Å barriers each separated by a 50 Å well. The potential height of the barriers is 170 meV.

different materials) the relative positions of these minibands can be engineered. In between the minibands forbidden states are set up in which the electron cannot exist. Hence, by producing a forbidden gap above the top of the superlattice the barrier height has been artificially elevated to the bottom of the next allowed miniband. The thick layer of the MQB serves the same purpose as before, that of filtering out low energy electrons.

In the description above it is assumed that the layers are undoped, the interfaces are perfect and that scattering effects are neglected. This is not normally the case when considering real semiconductor devices.

3.5 MQB Design

3.5.1 Design Issues

The purpose of any MQB is to produce as high a virtual barrier as possible to electron overflow. The height of the designed barrier depends strongly on the following structural parameters:

1. well and barrier thickness in the superlattice,
2. anti-tunnelling layer thickness,
3. number of well/barrier pairs in superlattice,

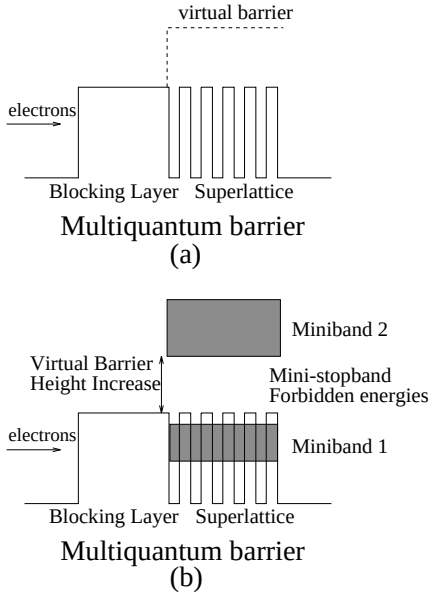

Figure 3.9: Two views of the MQB. (a) Virtual barrier produced by constructive interference of electron wavefunctions and (b) Graphical view of increased virtual barrier due to the presence of forbidden energy states.

4. effective mass difference between the well and barrier regions.

With regard to points 3 and 4 above, the number of well barrier pairs control the sharpness of the cut-off in the reflection of electrons while a large difference in effective mass reduces the number of well/barrier pairs required for a particular reflection [43], this is analogous to a large refractive index step in the case of optical Bragg reflection.

3.5.2 Designing a MQB

In order for a MQB to provide a virtual barrier it is essential that the electron wavefunction should remain coherent throughout the superlattice region of the MQB. This requirement cannot be met in structures that are thicker than the electron coherence length. It has been shown from photoconductivity measurements of a GaAs/AlGaAs superlattice that an electron in the superlattice miniband can have a room temperature coherence length of up to 495 Å. [54] Using this value as an upper limit of the electron coherence length in $(Al_xGa_{1-x})_{0.5}In_{0.5}P$ implies that for a MQB to work effectively at room temperature it needs to be significantly less than 500 Å thick, while still maintaining a high reflection coefficient. Typically a MQB is placed in the p-cladding region of the laser with the anti-tunnelling layer facing the incoming electrons. In this orientation the electron needs to remain coherent over the entire MQB structure, not just the superlattice. However, due to the reciprocity of the problem the electron re-

flectivity of the MQB is identical irrespective of whether the electrons encounter the superlattice region or the anti-tunnelling layer first. It is more advantageous however, from the point of view of preserving coherence, to have the superlattice region of the MQB adjacent to the active region. Electrons at energies resonant with the quantised states in the superlattice may tunnel out of the active region but it is expected that these will be returned by reflection from the bulk cladding region. In this sense the cladding region serves as the anti-tunnelling layer of the MQB. [13] There could be some difficulties though if the transit time of the electron is comparable with the carrier lifetime. If this is the case then the probability of spontaneous recombination in the superlattice portion of the MQB could be very high. This does not appear to be the case, however, based on the experimental evidence presented in Chapter 7.

Bearing these points in mind the design procedure is as follows:

1. Choose the material of interest to provide as large a difference in effective mass between well and barrier regions as possible.
2. Choose the well and barrier thickness to be as thin as possible but such that the first miniband in the superlattice does not extend above the top of the conduction band minimum in the barrier material.
3. The superlattice region of the MQB and not the anti-tunnelling layer should be closest to the active region of the laser which results in the cladding region of the laser acting as the anti-tunnelling layer.
4. No more than five well/barrier pairs in the superlattice are required.

3.5.3 Alternative MQB designs

Various MQB structures have been proposed in the literature. In this section these designs are described.

The simplest and probably the most useful MQB structure is one where both the wells and barriers in the superlattice are the same thickness. With this type of design a high reflection coefficient can be achieved with a very thin superlattice arrangement. Effective barriers are simply designed by making the well/barrier pairs as thin as possible while ensuring that the miniband remains below the top of the barrier. A variation on this design is the modified multiquantum barrier proposed by Takagi *et al* [55] where the well in the superlattice is narrower in bandgap than the active region of the laser in question (see Fig. 3.10 (a)). The advantage of this type of design is that the superlattice period can be made thinner while still keeping the miniband below the top of the barrier. By making the superlattice period thinner the virtual barrier height improvement is increased by pushing the second miniband higher in energy and thus widening the forbidden energy gap between the sub-bands.

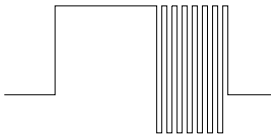

(a) Modified Multiquantum Barrier

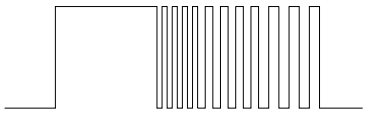

(b) Chirped Multiquantum Barrier

Figure 3.10: (a) Modified multiquantum barrier structure, (b) example of a chirped MQB structure.

A more complicated structure would involve designing the superlattice with wells and barriers of different thickness. This gives an extra degree of freedom in the design but makes the design of an optimised MQB structure much more difficult.

The final major type of MQB design is that of the chirped [32], stacked [48] or superposed [52] multiquantum barriers as shown in Fig. 3.10 (b). All of these designs rely on placing several superlattices of different periods in series with each other. Each superlattice provides a different energy window of high reflection and the effect of placing several of these in series results in a much higher reflection than can be achieved with a uniform superlattice. The main disadvantage of this technique is that the thickness of the superlattice region needs to be larger than other designs which makes it more difficult to maintain electron coherence.

3.6 Summary

The reflection from and transmission through single barriers was calculated and the methods used to calculate the reflection from multiple barriers was explained in this chapter.

The MQB is described as a reflector for electrons in a manner analogous to a Bragg reflecting mirror for photons. The main factors to consider in the design of a MQB are the well and barrier thicknesses in the superlattice; the anti-tunnelling layer thickness; the number of well/barrier pairs in the superlattice; and the effective mass difference between the well and barrier regions. The design procedure involves having as large a difference in effective mass between the wells and barriers by choosing the materials carefully; making the wells and barriers as thin as possible without allowing the first miniband to extend above the top of the barrier; reversing the MQB from its normal

orientation; and using only five well/barrier pairs.

Based on electron coherence considerations it is argued that the MQB should be reversed from its normal orientation when included in a laser diode. This argument is elaborated further in the next chapter.

Alternative MQB designs encountered in the literature include the modified MQB where the wells of the superlattice are lower in energy that the active region of the laser; MQBs with different well and barrier thicknesses; and the chirped, stacked or superposed MQBs where several superlattices of different periods are placed in series. The MQBs described in this thesis generally have the same well/barrier width, except in Chapter 5 where the well and barrier widths are different.

Chapter 4

Improved Multi-Barrier Transmission Models

4.1 Additional Considerations in MQB Design

A major limiting factor in the design of MQBs is the breakdown of electron coherence caused by elastic and inelastic scattering of electrons in the MQB. This scattering is induced by lattice vibrations, interfacial imperfections, the presence of dopant impurities and electron-electron interactions. These are all unavoidable in semiconductors but measures can be taken to minimise their effects and these are described below. The MQB structure should be undoped to reduce the number of ionised impurity scattering sites and consequently reduce ionised impurity scattering. It is known that molecular beam epitaxy (MBE) offers higher quality interfaces and lower background doping than metal organic vapour phase epitaxy (MOVPE). However, it is difficult to grow phosphorus containing compound by MBE due to the memory effect of phosphorus. For the growth of MQBs in materials other than AlGaInP MBE should offer a better alternative than MOVPE.

By reversing the orientation of the MQB as suggested in the previous chapter the effective thickness over which the electron needs to remain coherent is reduced to that of the superlattice.

Unfortunately the major drawback to the design of any MQB is the lack of information available on the bandstructure. In the case of the AlGaInP material system the values for the effective masses in the conduction band are not very well characterised and this makes the design of any MQB using this material somewhat unreliable. This has been demonstrated explicitly by Yen *et al* in a recent paper [49] where they show the differing values of effective mass being used by two different research groups working on MQBs. An additional conclusion that they come to is that the X-valley superlattice in a MQB plays an important role in the blocking of electron overflow. This hypothesis

is tested using the models described in this chapter.

4.2 AlGaInP Material Parameters used in Subsequent Simulations

The material parameters used in the simulation of AlGaInP MQBs are presented in this section.

4.2.1 Sublattice Ordering

Normally, in a ternary alloy such as GaInP, the group III atoms are expected to occupy their sublattice sites in a random arrangement. An ordered phase of GaInP occurs spontaneously under certain growth conditions where alternating layers of GaP and InP lie stacked on the {111} planes as shown in Fig. 4.1. This long range ordering has

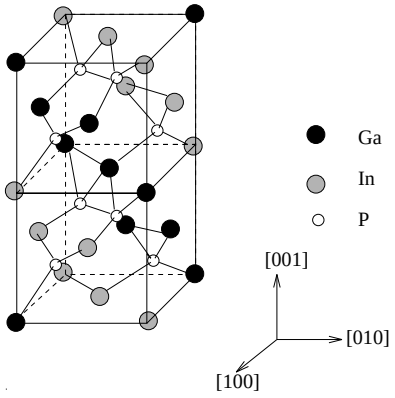

Figure 4.1: Unit cell of ordered $Ga_{0.5}In_{0.5}P$ alloy.

a periodicity twice that of the normal lattice parameter, and so it may be observed as superstructure peaks in a selected area diffraction pattern (SADP) halfway between the normal {111} Bragg reflections. Atomic ordering on the group III sublattice reduces the bandgap energy of the ternary alloy thus making device design difficult when the resulting bandgap can differ largely from the expected bandgap. Bandgap reduction is an undesirable effect since the magnitude of the reduction depends on the degree of ordering. This is not easy to quantify, so for comparison between samples it is better that the samples are grown with a completely random lattice structure as evidenced by the absence of superspots on a SADP picture of the sample material.

Growth temperature and substrate orientation influences the ordering in AlGaInP. Inclining the substrate towards the (111) direction reduces the tendency to order.[19] There are several other techniques that have been used to disorder AlGaInP. Some of

these include, heavy p-doping during growth and impurity diffusion following growth.[56] At the NMRC, substrates misoriented by 3° from the (001) direction towards the ⟨111⟩A planes and a growth temperature of 760°C are used to suppress sublattice ordering.

4.2.2 Band Gaps in AlGaInP

As the aluminium composition, x, of the $(Al_xGa_{1-x})_{0.5}In_{0.5}P$ alloy increases, the bandgap energies also increase in a linear fashion. The composition dependencies of the various bandgap energies in $(Al_xGa_{1-x})_{0.5}In_{0.5}P$ are summarised in Table 4.1. [34, 57]

Energy	*GaInP*(2K)	*AlInP*(2K)	$(Al_xGa_{1-x})_{0.5}In_{0.5}P$ (300K)
E_Γ (eV)	1.9789	2.5889	1.8849 + 0.61x
E_X (eV)	2.2581	2.3431	2.1641 + 0.085x

Table 4.1: Bandgap energies in $(Al_xGa_{1-x})_{0.5}In_{0.5}P$.

The indirect (X) bandgap energy also increases linearly with composition but at a slower rate than the direct bandgap. The direct (,) bandgap energy of $Ga_{0.5}In_{0.5}P$ can be reduced due to atomic ordering of Ga and In on the group III sublattice. This ordering occurs spontaneously under certain growth conditions and causes the bandgap to shrink. Different growth techniques as described in Ref. [56] and off-axis substrates [35, 36] are used to randomise the alloy. Ordered GaInP has a bandgap energy $E_\Gamma \sim 1.84$ eV, while the bandgap of the random alloy is ~ 1.8849 eV at room temperature. Depending on the degree of ordering it is possible to get values of the bandgap energy that lie between these values. Depending upon the degree of ordering, the AlGaInP , $-X$ crossover point can lie between $x = 0.52$ and $x = 0.7$. In this work the crossover for the random alloy is taken to be at a composition of $x = 0.52$. [58] Also throughout this work the ratio of the conduction band offset to the valence band offset $(\Delta E_c : \Delta E_v)$ is taken to be 70:30 which is consistent with values found in the literature. [8, 58, 59, 19]

4.2.3 Carrier effective masses in AlGaInP

Knowledge of the carrier effective masses is important for laser design because they determine the density of states. A greater effective mass implies a greater density of states and hence higher injected carrier densities are required to achieve a population inversion. In the literature there are several different reports for the carrier effective masses in AlGaInP, [49, 60] thus making these values unreliable. The values for the end point ternary alloys are consistent in the literature [60, 29] and so these are used to

calculate the carrier effective masses for AlGaInP by linear interpolation. The values of carrier effective mass used throughout this work are presented in Table 4.2.

Effective Mass	*GaInP*	*AlInP*	$(Al_xGa_{1-x})_{0.5}In_{0.5}P$
m_e^*/m_0	0.11	0.35	0.11 + 0.24x
m_{hh}^*/m_0	0.48	0.555	0.48 + 0.075x
m_{lh}^*/m_0	0.14	0.165	0.14 + 0.025x

Table 4.2: Carrier effective masses in $(Al_xGa_{1-x})_{0.5}In_{0.5}P$.

4.3 Numerical Modelling of the MQB

4.3.1 Introduction

The most useful models of electron transport are based on effective mass approximation models, due to their ease of implementation and the acceptable accuracy they provide for many calculations. This is also the case for multi-barrier transport in AlGaInP based semiconductors. Unfortunately, as mentioned in Chapter 2, there is a major drawback with this material system in that the , and X minima in the conduction band are in close proximity to each other in energy and they cross at an aluminium composition of between 50 and 52%. This adds an additional complication to any simple effective mass approximation model since both conduction bands are in competition for occupancy. Account must therefore be taken of the possibility of a mixing of electron wavefunctions between states. Additionally, the effect of the various scattering mechanisms on the coherence of the electron wavefunction is an important issue to address. Any loss of coherence in the wavefunction will affect the reflectivity of the MQB as electrons lost to a scattering process cannot interfere in a constructive manner to provide a high reflection coefficient. The presence of X states and the possibility of scattering were not taken account of by Iga in his calculation of the reflection from MQBs. To this end two models were developed [1] to extend the simple model used by Iga. These models are outlined in the remainder of this section. [61, 62]

4.3.2 Description of , $-X$ Mixing Model

A phenomenological approach was taken to solve the problem of , $-X$ mixing in AlGaInP semiconductors. [17] In this approach the electron wavefunction in the structure is assumed to be a linear combination of the two lowest conduction band states, namely

[1] These models were developed in collaboration with the Physics department at University College, Cork.

the $|,\rangle$ state and the $|X\rangle$ state, which are taken as base states for analysis of the system. The actual state of the system $|\Psi\rangle$ can be written as a linear combination of these states,

$$|\Psi\rangle = f_1|X\rangle + f_2|,\rangle \tag{4.1}$$

where f_1 and f_2 are functions controlling the proportion of the electron wavefunction in each of the two base states.

Assuming parabolic bands, the time independent Schrödinger equation can be written

$$\begin{pmatrix} \frac{\hbar^2 \cdot k^2}{2m_X^*} + E_X & \Delta \\ \Delta & \frac{\hbar^2 \cdot k^2}{2m_\Gamma^*} + E_\Gamma \end{pmatrix} \begin{pmatrix} f_1 \\ f_2 \end{pmatrix} = E \cdot \begin{pmatrix} f_1 \\ f_2 \end{pmatrix} \tag{4.2}$$

where m_X^* and m_Γ^* are the electron effective masses and E_X and E_Γ are the energies of the X and , conduction band minima respectively. All energies are given with reference to the bottom of the , conduction band in the system. Δ is the mixing parameter, described below.

To account for the , $-X$ mixing induced by each interface in the MQB, the interface is assumed to be of finite thickness, which is arbitrarily fixed at a value of 2.5 Å. This is illustrated in Fig. 4.2. The band-edges and effective masses for the interface region are

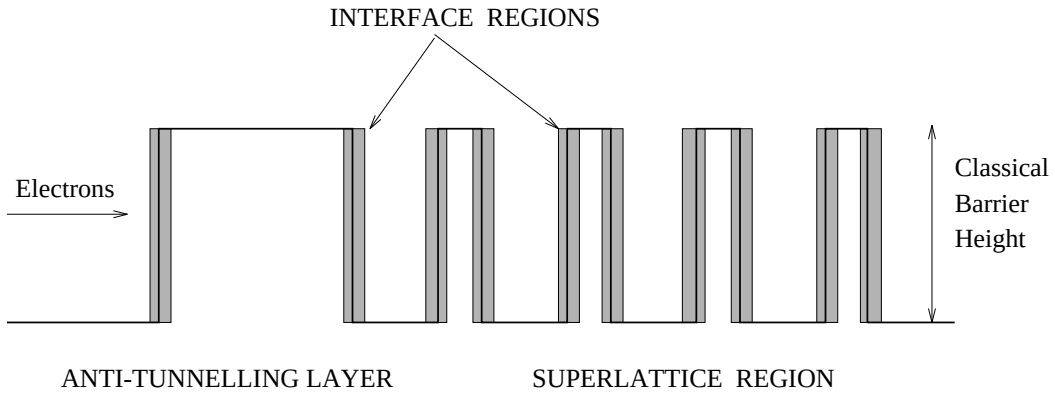

Figure 4.2: Schematic of MQB showing interface regions where , $-X$ mixing is allowed to occur.

assumed to be an average of those in the well and barrier. It is also assumed that all the mixing between states only occurs in these interface regions. This mixing of states is characterised by the mixing parameter Δ, and the interface thickness, both of which are unknown. However, by fixing the interface thickness the degree of mixing can be directly modified by only varying the magnitude of Δ. Hence, in Eqn 4.2, Δ has the value zero in all regions except the interface regions where it has a finite positive value. Δ acts as a cross-multiplication term to cause a mixing between the , and X states in

the interface regions, while in the wells and barriers the problem effectively becomes decoupled and the two states can be treated separately. The actual value of Δ must be determined either experimentally or by numerical comparison with more complex models. However, since the interface region thickness has been arbitrarily fixed, the value of Δ determined from comparison with complete band structure models remains of limited physical significance.

The general solution of the wavefunction in an interface region where mixing is allowed to take place is given in terms of the original base states by,

$$\begin{pmatrix} f_1 \\ f_2 \end{pmatrix} = \begin{matrix} (Ae^{ik^{\Gamma}x} + A'e^{-ik^{\Gamma}x} + B\beta e^{ik^{X}x} + B'\beta e^{-ik^{X}x}) \begin{pmatrix} 1 \\ 0 \end{pmatrix} + \\ (A\alpha e^{ik^{\Gamma}x} + A'\alpha e^{-ik^{\Gamma}x} + Be^{ik^{X}x} + B'e^{-ik^{X}x}) \begin{pmatrix} 0 \\ 1 \end{pmatrix} \end{matrix} \tag{4.3}$$

where A, A', B and B' are constants and α, β originate from the eigenvectors obtained from the solution of Eqn. 4.2. Once there is a solution to Eqn. 4.2, the problem is completed by matching the wavefunction and its probability current on either side of an interface describing two distinct regions.

For multi-barrier transmission the incident amplitudes, $\widetilde{C_1}$, are obtained by multiplying the output amplitudes, $\widetilde{C_n}$, by the transfer matrix for each interface, $T_1T_2T_3 \ldots T_{n-1}$. Hence,

$$\widetilde{C_1} = T_1T_2T_3 \ldots T_{n-1}\widetilde{C_n} \tag{4.4}$$

where $T_1T_2T_3 \ldots T_{n-1}$ are the transfer matrices for each interface and may be denoted by the system transfer matrix, T. [63]

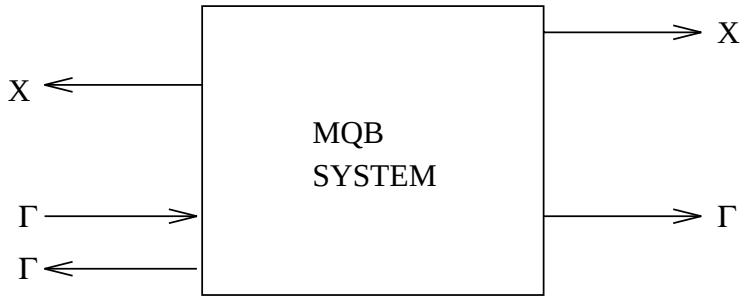

Figure 4.3: MQB system showing combinations of electron reflection and transmission for both the X and , states in the case of a visible laser diode.

For a MQB placed on the p-side of a laser active region, it is assumed that the incoming electrons will only be in the , state and that no electrons enter the system from the far side of the barrier because there is no source of electrons on that side (See

Fig. 4.3). Hence, Eqn 4.4 reduces to

$$\begin{pmatrix} 0 \\ A_1' \\ B_1 \\ B_1' \end{pmatrix} = T \begin{pmatrix} A_n \\ 0 \\ B_n \\ 0 \end{pmatrix} \tag{4.5}$$

where the subscripts refer to the layer in question and the constants A and B are for the amplitudes in the X-state and in the , -state respectively.

The reflection and transmission coefficients in the , and X band states are given by

$$\begin{aligned} R^{\Gamma} &= \frac{J^{\Gamma}_{refl}}{J^{\Gamma}_{inc}} = \left|\frac{B_1'}{B_1}\right|^2 \\ R^{X} &= \frac{J^{X}_{refl}}{J^{\Gamma}_{inc}} = \left|\frac{A_1'}{B_1}\right|^2 \frac{k_1^X m_1^{\Gamma}}{k_1^{\Gamma} m_1^X} \\ T^{\Gamma} &= \frac{J^{\Gamma}_{trans}}{J^{\Gamma}_{inc}} = \left|\frac{B_n}{B_1}\right|^2 \frac{k_n^{\Gamma} m_1^{\Gamma}}{k_1^{\Gamma} m_n^{\Gamma}} \\ T^{X} &= \frac{J^{X}_{trans}}{J^{\Gamma}_{inc}} = \left|\frac{A_n}{B_1}\right|^2 \frac{k_n^X m_1^{\Gamma}}{k_1^{\Gamma} m_n^X} \end{aligned} \tag{4.6}$$

From these relations the reflection coefficient of electrons as a function of their incident energy from the MQB can be determined. To estimate the magnitude of the mixing parameter Δ, the model was compared with the empirical pseudopotential model of Inkson and Marsh, [64, 65, 66] which essentially provides a complete description of the conduction band. Fig 4.4 shows the calculated electron transmission through single AlAs barriers of thickness 5.64 Å and 14.1 Å for both the Inkson and Marsh model and the model presented above. The effective mass for the X-minima in GaAs is taken to be $0.169m_0$, while that for the , minimum is taken as $0.069m_0$. The band edges are referenced with respect to the bottom of the GaAs , band. The X level in the GaAs is 0.365 eV above this reference level. For AlAs the effective masses are taken to be $0.224m_0$ and $0.124m_0$ for the X and , states respectively, while the X and , band-edges are 0.195 eV and 0.88 eV respectively above the , reference level in GaAs. The closest agreement between the two models was obtained by taking Δ to be between 40-50 meV, corresponding to a Δ-thickness product of between 0.1 and 0.125 eV Å. This is in excellent agreement with values between 0.08 and 0.16 eV Å quoted by Erdoğan *et al* [67] for their mixing parameter deduced from different models for GaAs/AlAs barriers. In general the , $-$ X mixing model underestimates the transmission coefficient by some $5-6\%$ and shows considerably less structure than the Inkson-Marsh model. This is due to the model accounting for only two conduction band states and assuming parabolic bands. Nevertheless, the reasonable agreement with the Inkson-Marsh model

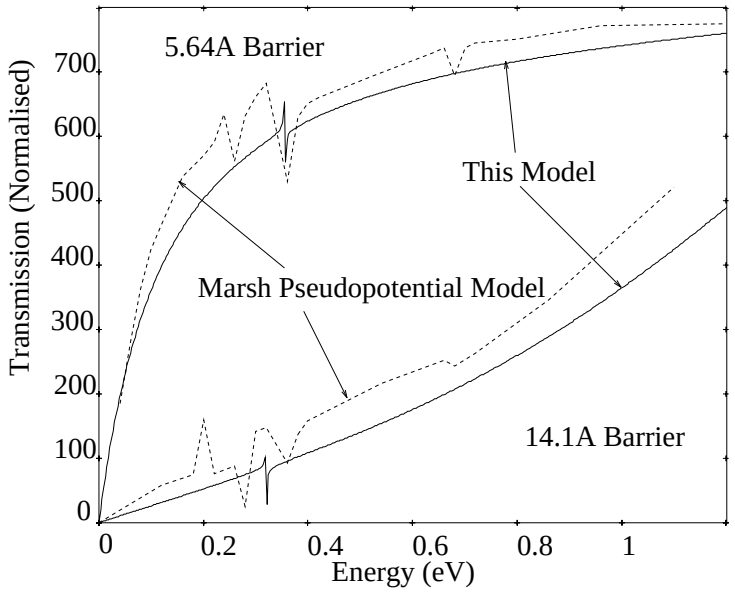

Figure 4.4: Comparison of the , $-X$ mixing model with the empirical pseudopotential model of Marsh for GaAs/AlAs single barrier of thickness 5.64 Å and 14.1 Å.

suggests that this simple effective mass model is capable of adequately modelling the effects of , $-X$ mixing in MQBs without the large overhead in calculation time and complexity.

4.3.3 Effects of , $-X$ Mixing on MQB Performance

The nomenclature used to describe the MQB is {anti-tunnelling layer thickness; number of periods $\times$ (well thickness, barrier thickness)} in normal orientation and by {number of periods $\times$ (well thickness, barrier thickness); anti-tunnelling layer thickness} in the reversed orientation. A MQB structure with dimensions $\{200\mathring{A}; 5 \times (24, 24)\mathring{A}\}$ in $(Al_{0.4}Ga_{0.6})_{0.5}In_{0.5}P$, $(Al_{0.5}Ga_{0.5})_{0.5}In_{0.5}P$ and $(Al_{0.6}Ga_{0.4})_{0.5}In_{0.5}P$ was modelled and the effect of , $-X$ mixing on the performance of the MQB was investigated. In all three cases the value of the mixing parameter, Δ, was taken to be 50 meV and the interface thickness was kept constant at 2.5 Å. AlGaInP becomes an indirect material at an aluminium composition of $\sim$52% and it is expected that at aluminium compositions above this that the X-minima in the conduction band should influence the electron transport more than the , minimum because they are then the lowest lying conduction band states. In Fig. 4.5 the electron reflection as a function of electron energy for an aluminium composition of 40% shows that there is no significant difference between the mixing and no-mixing cases. The cut-off in energy is reduced by 10-15 meV, but the structure of both plots is essentially the same. In Fig. 4.6, for an aluminium compo-

sition of 50%, there is a dip in reflection observable in the case of , $-X$ mixing, but again this is above the band edge and the reflection never drops below 80%. This dip is due to the influence of the X-minima which in this material is comparable in energy to the , minimum. This shows that the mixing between states becomes more significant

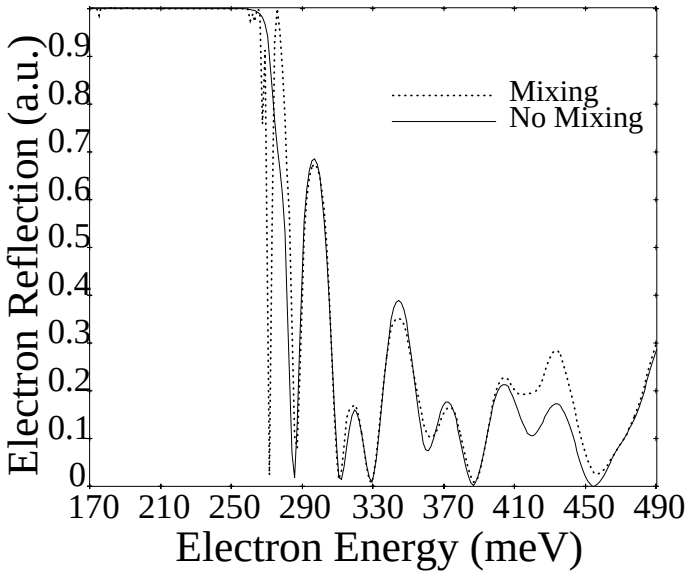

Figure 4.5: $\{200\mathring{A}; 5 \times (24,24)\mathring{A}\}$ $(Al_{0.4}Ga_{0.6})_{0.5}In_{0.5}P$ MQB with and without , $-X$ Mixing.

as the aluminium concentration is increased. However, the dip in reflection does not drop below 70% and is sufficiently narrow in energy to have no significant effect on the overall MQB performance.

The conclusion of this analysis is that interfacial , $-X$ mixing, within the limits of the approximations used in this model, does not significantly affect the MQB performance. The $X-$minima are, however, more influential on the electron reflection as the aluminium composition of the material is increased beyond the crossover composition.

4.3.4 Description of Scattering Model

To rigorously take account of electron scattering is beyond the scope of this thesis. This is a complicated problem in its own right that would require the close attention of an experienced theoretician. Nevertheless, for MQB calculations, when the electron energies are greater than the barrier height a relatively straight forward approach can be taken which allows first approximations to be made. This approach is outlined in this section.

The problem of electron scattering within a MQB structure may be thought of as a loss of coherent electrons. This assumption is valid in the sense that scattered electrons

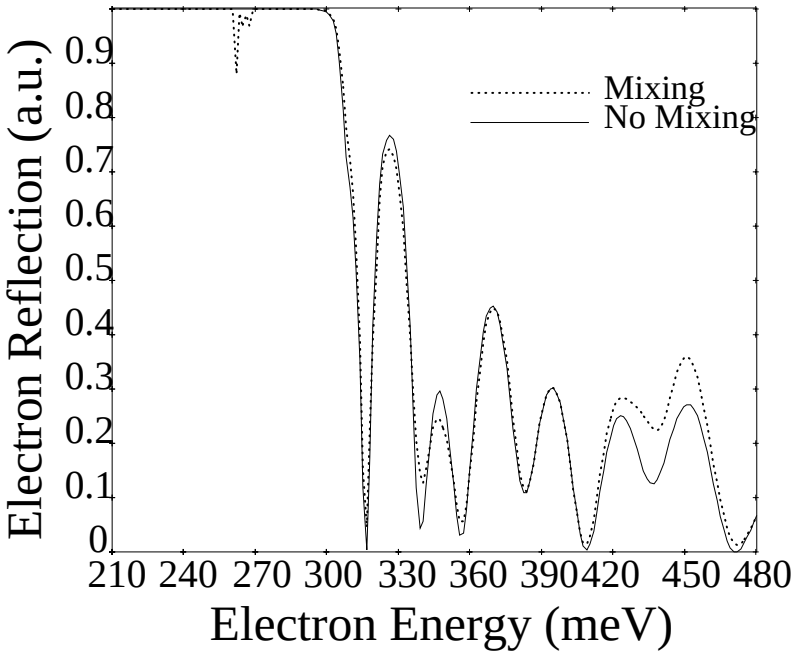

Figure 4.6: $\{200\mathring{A}; 5 \times (24, 24)\mathring{A}\}$ $(Al_{0.5}Ga_{0.5})_{0.5}In_{0.5}P$ MQB with and without , $-X$ Mixing.

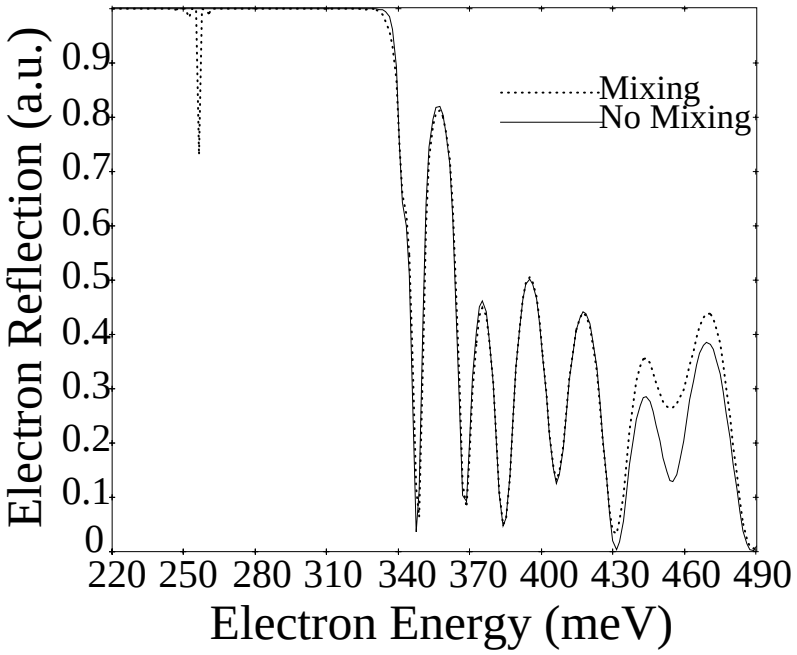

Figure 4.7: $\{200\mathring{A}; 5 \times (24, 24)\mathring{A}\}$ $(Al_{0.6}Ga_{0.4})_{0.5}In_{0.5}P$ MQB with and without , $-X$ Mixing.

are not reflected into coherent states and cannot therefore contribute to any enhanced reflection due to the MQB. As electrons are considered lost to the scattering processes there is no conservation of coherent probability current across the MQB even though the total probability current is conserved. This means that the sum of the reflectivity and the transmissivity is not equal to one. The loss of electrons, for this interpretation, may be written as a reduction in the amplitude of the electron wavefunction as the electrons travel from one interface to the next. A scattering parameter, α, is defined to be the fraction of the wavefunction amplitude that reaches the other side of a particular layer. The thicker the layer, the smaller the value of α will be. This corresponds to a probability, $|\alpha|^2$ that a single electron will reach the other side of the layer without being scattered.

Consider electrons incident on an interface from the i^{th} region of a MQB. The wavefunction for these electrons has an amplitude $A_i^{b\ 2}$ A certain fraction of this amplitude is reflected from the interface and the remainder is transmitted into the $i+1^{th}$ region. These fractions are denoted $r_{i,i+1}$ and $t_{i,i+1}$ respectively. In each case the first subscript denotes the region from which the electrons have originated and the second subscript denotes the region on the other side of the interface. This situation is illustrated in Fig. 4.8.

Electrons incident on the interface from the left and the right give rise to electrons emerging from both sides of the interface in a relationship that may be expressed as in Eqn 4.7

$$A_i^{b2} = r_{i,i+1}A_i^{b1} + t_{i+1,i}A_{i+1}^{a2}A_{i+1}^{a1} = t_{i,i+1}A_i^{b1} + r_{i+1,i}A_{i+1}^{a2} \tag{4.7}$$

and illustrated in Fig. 4.9.

These equations can be written in matrix form as:

$$\begin{pmatrix} A_{i+1}^{a1} \\ A_{i+1}^{a2} \end{pmatrix} = \begin{pmatrix} M_i^{11} & M_i^{12} \\ M_i^{21} & M_i^{22} \end{pmatrix} \begin{pmatrix} A_i^{b1} \\ A_i^{b2} \end{pmatrix} \tag{4.8}$$

The matrix $\widetilde{M}_i$ can be used to obtain the wavefunction on the right hand side of the i^{th} interface from the wavefunction on the left hand side and hence a similar matrix may be written for each interface in the MQB.

Considering the scattering of electrons within the semiconductor as a loss of electrons between the interfaces of the MQB, then this loss may be expressed as a reduction of the wavefunction amplitude as the electrons travel from one side of a region to the other. If a fraction α_i of the amplitude makes it from one side of a region to the other

[2]The subscript refers to the region of the MQB while the superscript, b, indicates that it is the amplitude of the wavefunction at the $i+1^{th}$ side of Region i rather than the $i-1^{th}$ side of Region i which would be represented by a superscript a.

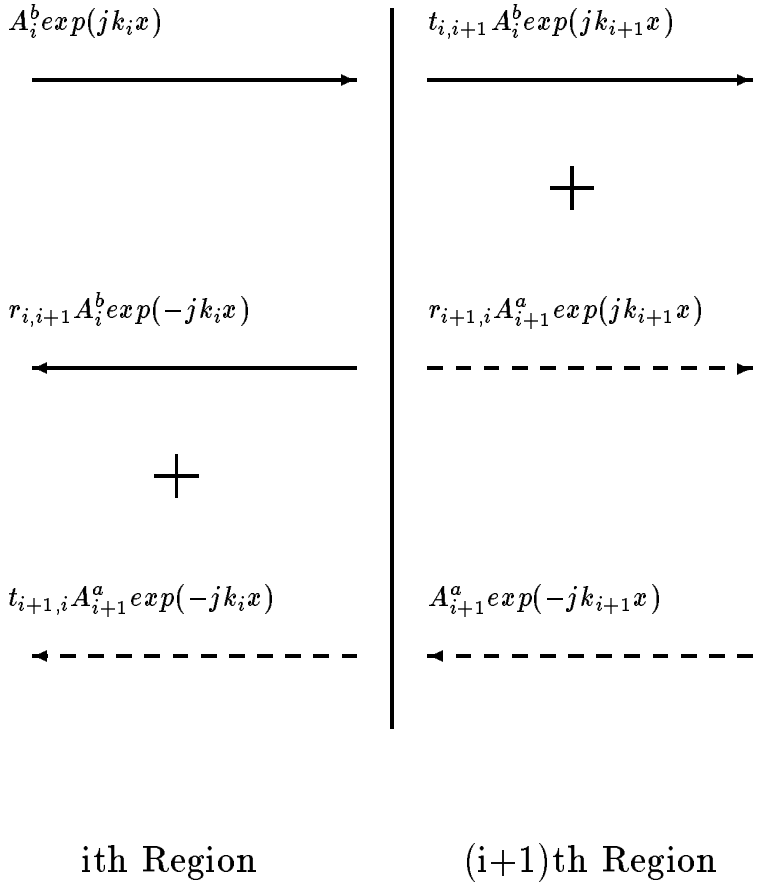

Figure 4.8: Schematic showing transmission through and reflection from an interface illustrating the nomenclature described in the text.

then

$$\begin{pmatrix} A_i^{b1} \\ A_i^{b2} \end{pmatrix} = \begin{pmatrix} \alpha_i & 0 \\ 0 & 1/\alpha_i \end{pmatrix} \begin{pmatrix} A_i^{a1} \\ A_i^{a2} \end{pmatrix} = \widetilde{\alpha_i} \widetilde{A_i^a} \tag{4.9}$$

The matrix relating the wavefunction amplitude on the right hand side of the i^{th} interface to that on the right hand side of the $i+1^{th}$ interface is therefore

$$\widetilde{N_i} = \widetilde{M_i} \widetilde{\alpha_i} \tag{4.10}$$

For the entire system then

$$\widetilde{A_n} = \tilde{D} \widetilde{A_1} \tag{4.11}$$

where

$$\tilde{D} = \widetilde{N_{n-1}} \widetilde{N_{n-2}} \ldots \widetilde{N_1} \tag{4.12}$$

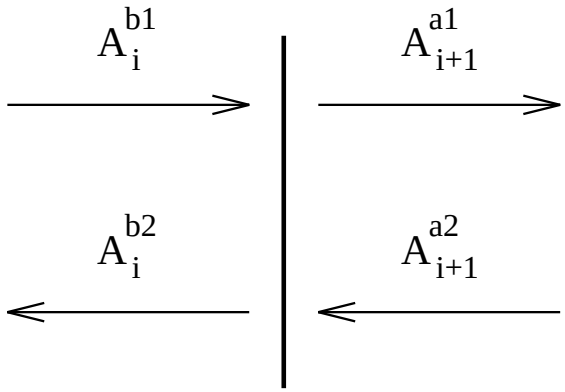

Figure 4.9: Situation at an interface with all amplitudes travelling to the left added and all amplitudes travelling to the right added.

For a system made up of n layers there are $n-1$ interfaces and so $\tilde{D}$ is the product of $n-1$ matrices. If the region to the left of the system of layers is called Region 1 then the region to the right of the system is termed Region n. Then

$$\begin{pmatrix} A_n^1 \\ A_n^2 \end{pmatrix} = \begin{pmatrix} D_{11} & D_{12} \\ D_{21} & D_{22} \end{pmatrix} \begin{pmatrix} A_1^1 \\ A_1^2 \end{pmatrix} \tag{4.13}$$

But $A_n^2 = 0$ because there are no electrons incident on the MQB from the right.

Hence,

$$\frac{A_1^2}{A_1^1} = -\frac{D_{21}}{D_{22}} = \frac{Amplitude\,of\,reflected\,wave}{Amplitude\,of\,incident\,wave} = r \tag{4.14}$$

$$\frac{A_n^1}{A_1^1} = D_{11} - \frac{D_{12}D_{21}}{D_{22}} = \frac{Amplitude\,of\,transmitted\,wave}{Amplitude\,of\,incident\,wave} = t \tag{4.15}$$

$$Reflection\,Coefficient = R = r^*r = \left|\frac{D_{21}}{D_{22}}\right|^2 \tag{4.16}$$

$$Transmission\,Coefficient = T = t^*t = \left|D_{11} - \frac{D_{12}D_{21}}{D_{22}}\right|^2 \tag{4.17}$$

The magnitude of the scattering parameter, α, can be estimated from the mean free path of an electron in the MQB. One approximation to the mean free path of an electron in a superlattice is its coherence length. This is measured to be 495 Å at room temperature in GaAs/AlGaAs superlattices. [54] For a population of n_0 electrons travelling a distance x, the population that is not scattered may be described by

$$n = n_0 e^{\frac{-x}{\lambda}}$$

where λ is the mean free path. In terms of amplitude this may be rewritten as

$$A = A_0 e^{\frac{-x}{\lambda}}$$

hence, α may be written as

$$\alpha = e^{\frac{-x}{\lambda}}.$$

Software was written in FORTRAN to implement the model described above. The effects of scattering within the MQB are investigated by looking at the reflection from a MQB with and without scattering effects. The MQBs simulated are {1260 Å ; 5×(24,24) Å } and {200 Å ; 5×(24,24) Å } where $(Al_{0.4}Ga_{0.6})_{0.5}In_{0.5}P$ is the barrier material and $Ga_{0.5}In_{0.5}P$ is the well material. The first MQB design is chosen to match the dimensions of the MQB used in the lasers of Chapter 7, while the second has a more typical anti-tunnelling layer thickness. Each of the MQBs described above was modelled for the two cases (i) $\alpha = 1$ for every layer (no scattering) and (ii) $\alpha = 0.953$ [3] for the 24 Å layers and $\alpha = 0.078$ for the 1260 Å layer.

The no scattering case is illustrated in Fig. 4.10 where the reflection is shown from the barrier band edge to 500 meV above the band edge in the well. No account is taken

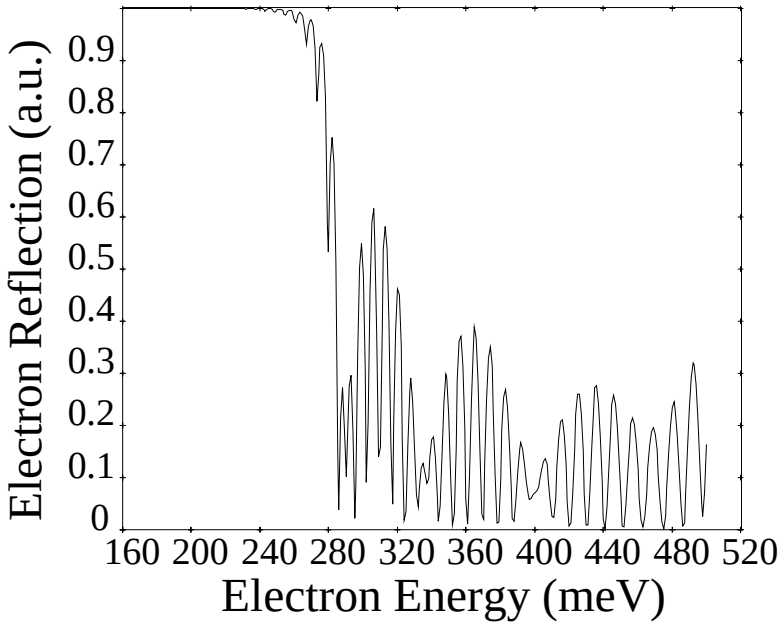

Figure 4.10: Electron reflection as a function of energy for $\{1260\ \mathring{A}; 5 \times (24, 24)\ \mathring{A}\}$ and $\{5 \times (24, 24)\ \mathring{A}; 1260\ \mathring{A}\}$ without scattering effects.

of the evanescent states (states with energies below the barrier band edge) since this

[3] $\alpha = 0.953$ is calculated by assuming an electron coherence length of 495 Å at room temperature. [54]

would involve calculations beyond the scope of this thesis; in addition, for the MQB principle, it is only electrons with energies larger than the barrier that are of interest. From this figure the increased barrier height is approximately 100 meV.

This is not the case when scattering effects are taken into consideration. In Fig. 4.11 the anti-tunnelling layer of the MQB is to the left of the superlattice and as a result the high reflection obtained in the case of no scattering is lost. This is entirely due to the breakdown in coherence of the electron wavefunction caused by the thickness of the anti-tunnelling layer. The superlattice plays no effective part in the MQB because very few electrons actually reach it. This is the case even if the anti-tunnelling layer is only 200 Å thick. These figures alone illustrate that it is unlikely for a conventional MQB to work as an electron reflector. However, if the orientation of the MQB is reversed by placing the anti-tunnelling layer to the right of the superlattice, the electrons encounter the superlattice region first. If this MQB is modelled using the same values of the scattering parameter as above then there is a dip in the reflection at the band-edge but this recovers quickly to above 90% reflection for approximately 100 meV as was the case with no scattering. This is shown in Fig. 4.12 and from a comparison of this figure and Fig. 4.11 it can be concluded that it is better for the electrons to encounter the superlattice region of the MQB before the anti-tunnelling region. This orientation ensures that a large proportion of the incident electrons remain coherent over the superlattice region and can constructively interfere to provide the high reflection required. This may seem like an obvious result but this is the first time this has been reported or commented upon. It is this result that led to the decision to incorporate the MQB in the reversed orientation in the visible laser diodes described in Chapter 7. One possible problem that could arise from having the MQB in reversed orientation is the possibility of spontaneous recombination of electrons in the superlattice of the MQB. This can occur if the transit time of the electrons crossing the superlattice is comparable to the carrier lifetime. Any recombination in the superlattice is undesirable since this is just another leakage path for electrons. Therefore any benefit that is gained from the increased reflection above the barrier energy could be balanced by loss of electrons through recombination in the superlattice. This is not the case, as will be shown in Chapter 7 with the inclusion of reversed MQBs in visible laser diodes.

Consideration was also given to values of α assuming a low temperature (5 K) coherence length of 935 Å. [54] This gives values for α of 0.975 for the 24 Å layers and 0.26 for the 1260 Å layers. Even at 5 K the MQB in normal orientation is shown not to work while the MQB in reversed orientation shows enhanced electron reflection above the barrier height. This is also the case when a more typical value of 200 Å is used for the anti-tunnelling layer thickness.

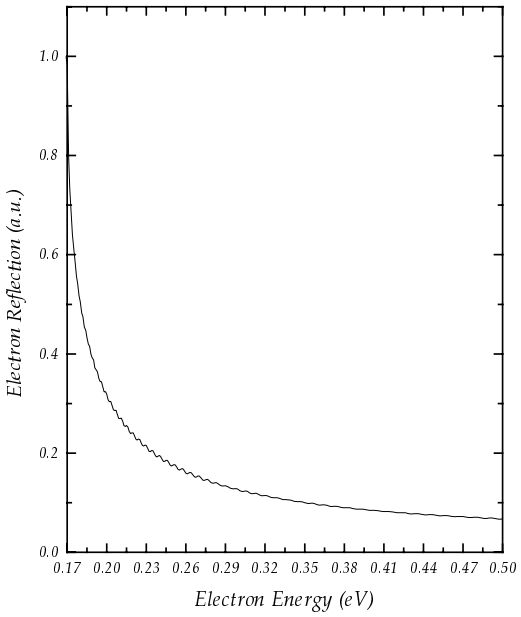

Figure 4.11: Electron reflection as a function of energy for $\{1260\ \mathring{A}; 5 \times (24, 24)\ \mathring{A}\}$ with scattering effects for energies above the bulk barrier height.

4.4 Theoretical Investigation of the MQB

4.4.1 Effect of random layer thickness fluctuation

Variations in layer thickness of a few monolayers are to be expected even in the best of growth conditions. When the grown layers are themselves of the order of a few monolayers, as in the case of the superlattice region of the MQB, these thickness fluctuations could have a significant effect on the MQB's performance. To examine the effect of this variation on the performance of the MQB a control sample was designed using $Ga_{0.5}In_{0.5}P/(Al_{0.5}Ga_{0.5})_{0.5}In_{0.5}P$ and having a layer structure of $\{150\ \mathring{A}; 5 \times (15, 35)\ \mathring{A}\}$. A series of four other samples were modelled allowing random variations in the layer thickness of up to $\pm 4 \times 2.5\ \mathring{A}$ on the control sample. These samples are outlined in Table 5.1. The parameters used in the simulation of the above structures are given in Table 4.4. The influence of the X minima is not taken into consideration in the simulation for the reasons described in Section 4.3.3. The results of the *cut-off in energy* [4] of the reflection for each of the samples described above is given in Table 4.5.

From the above results the difference in cut-off energy for each of the samples is no

[4] This is defined here to be the energy at which the electron reflection drops below 99.9%. This is an arbitrary definition to allow meaningful comparison between structures. This definition was first employed by Kishino *et al* [14] since this is typically the reflection coefficient required in a Bragg reflector for operation in a Vertical Cavity Surface Emitting Laser (VCSEL).

Layer	*Control* Å	*Sample 1* Å	*Sample 2* Å	*Sample 3* Å	*Sample 4* Å
Blocking Layer	150	150	152.5	152.5	152.5
Well 1	15	5	10	25	17.5
Barrier 1	35	42.5	30	40	30
Well 2	15	22.5	22.5	10	17.5
Barrier 2	35	32.5	37.5	35	40
Well 3	15	22.5	25	12.5	12.5
Barrier 3	35	25	42.5	45	35
Well 4	15	12.5	17.5	22.5	15
Barrier 4	35	35	32.5	25	45
Well 5	15	17.5	20	20	22.5
Barrier 5	35	42.5	27.5	30	37.5

Table 4.3: Description of samples to investigate the influence of random layer fluctuations.

Layer	m^*_Γ	E_Γ (eV)
Well	0.11	0.0
Barrier	0.23	0.2135

Table 4.4: Layer parameters used in the calculation.

Sample	*Cut-off energy* (meV)
Control	290.8
1	274.3
2	269.4
3	270.4
4	271.2

Table 4.5: Comparison of cut-off energy for samples with random layer thickness fluctuations.

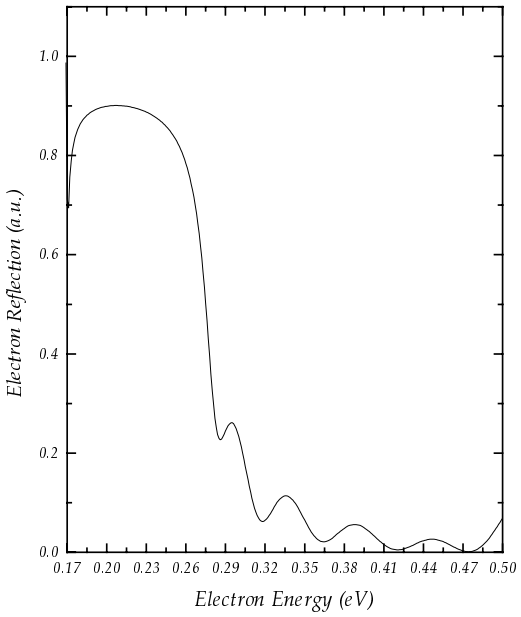

Figure 4.12: Electron reflection as a function of energy for $\{5 \times (24, 24)\ \mathring{A}; 1260\ \mathring{A}\}$ with scattering effects for energies above the bulk barrier height.

more than 21.4 meV from that of the control sample. The control sample is seen to have the highest cut-off energy but the other samples are all within 5 meV of each other in terms of their cut-off point. This implies that a random variation in the thickness of the various layers does not greatly affect the overall result, even though random variations tend to reduce the virtual barrier. The barriers with random variations still provide a better barrier than would be expected for the bulk case, 213.5 meV.

4.4.2 Effect of systematic layer thickness fluctuation

To examine the effect of systematic layer thickness fluctuation on the MQB's reflectivity the anti-tunnelling layer is kept at a constant thickness while the well and barrier thicknesses in the superlattice are varied by 2 Å each time. The starting design structure is $\{180\ \mathring{A}; 5 \times (14, 14)\ \mathring{A}\}$ increasing to $\{180\ \mathring{A}; 5 \times (40, 40)\ \mathring{A}\}$ in 2 Å increments. The barrier material is $(Al_{0.4}Ga_{0.6})_{0.5}In_{0.5}P$ and the well material is $Ga_{0.5}In_{0.5}P$. These structures were specifically designed for incorporation into the n-i-n tunnel diodes described in Chapter 6 to allow a meaningful comparison between the experimentally measured barrier height and that calculated here. A plot of the barrier height improvement as a function of well/barrier thickness is shown in Fig. 4.13. This figure shows that for very narrow well/barrier thicknesses (< 20 Å) there is no improvement in the barrier height. However, at 20 Å the barrier height reaches a maximum of 285.9 meV which is an improvement of 115.1 meV over the bulk barrier height of 170.8 meV. At

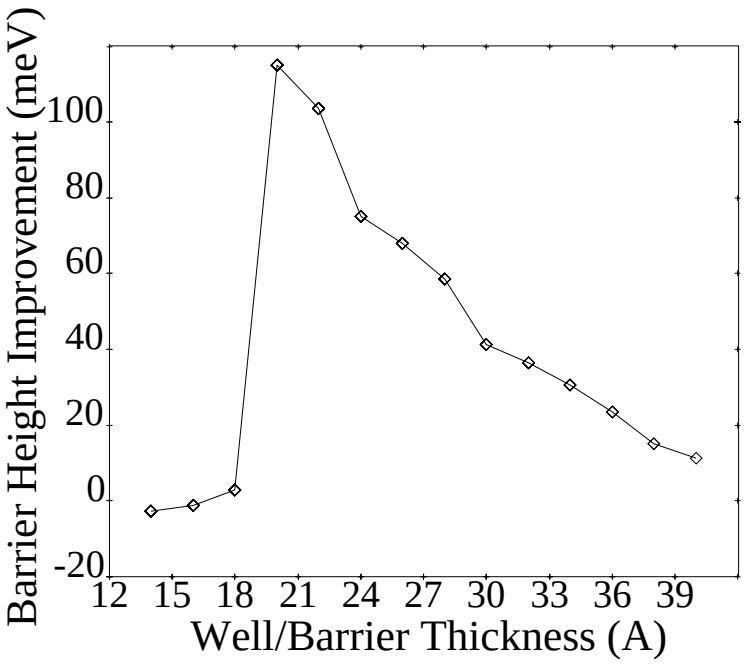

Figure 4.13: Variation in apparent barrier height improvement as a function of well/barrier thickness.

well/barrier thicknesses wider than this the barrier height improvement drops off at approximately -5 meV/Å.

This is an important result because it implies that in a design it is better to have well/barrier pairs that are slightly thicker than the thickness required for the highest barrier to allow for growth fluctuations. For the particular case considered above, where the thickness for the highest virtual barrier is at 20 Å for the well and barrier, it is better to choose 24 Å to be the design thickness to allow for a 4 Å error in the growth.

4.4.3 Effect of varying anti-tunnelling layer thickness

From Fig. 4.14 the effect of varying the thickness of a single $(Al_{0.4}Ga_{0.6})_{0.5}In_{0.5}P$ barrier on its apparent barrier height is shown. In this figure, at 340 Å the cut-off in energy due to transmission is equal to the expected bulk barrier height. This height is preserved down to a thickness of approximately 150 Å and as the barrier gets thinner the apparent barrier height begins to drop, gradually at first, but falling off sharply between 100 and 50 Å. At 20 Å the barrier is effectively non-existent as far as an electron is concerned. This sets a lower bound on the anti-tunnelling layer thickness. The barrier needs to be greater than 150 Å for its bulk character to be preserved. This will of course vary from material to material and will largely depend on the electron effective mass.

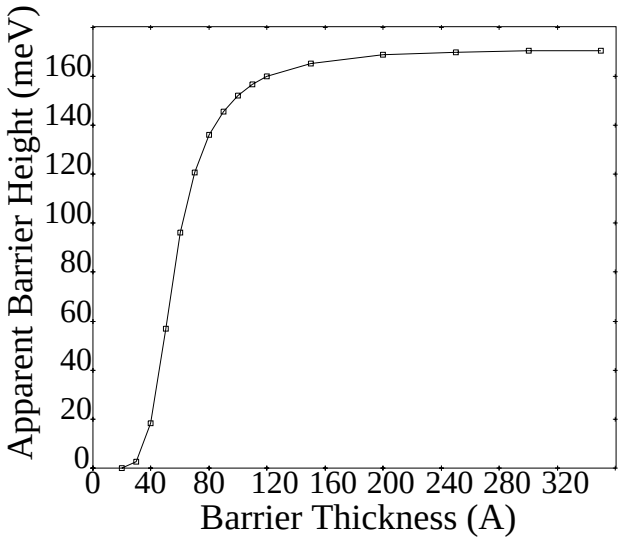

Figure 4.14: Variation in apparent barrier height with thickness for a single AlGaInP barrier.

4.4.4 Effective mass variation in a design

Repeating the simulation of Section 4.3.2 where the well/barrier thicknesses were varied but this time allowing the effective mass in the barrier to be varied by $\sim \pm$ 10%. This value was chosen to see if even small fluctuations in effective mass can be significant on MQB performance. The effective mass in the barrier is one of the most uncertain parameters in a design because of the variety of values reported for it. If a 10% fluctuation is shown to be significant then the large variation in the effective mass values reported in the literature are sure to be even more significant. It appears from Fig. 4.15 that if the electron effective mass in the barrier is reduced then the well/barrier pair thickness needs to be increased to compensate. This is logical considering that a lower effective mass implies that the miniband will lie higher up in a superlattice of the same dimensions. By increasing the period of the superlattice this effect is reduced and the miniband is brought back close to its previous level. This is another illustration of the analogy between the optical Bragg reflector and the MQB. In the optical Bragg reflector a high refractive index step between layers implies that thinner reflecting mirrors may be used, but thicker mirrors need to be used if the refractive index step is not large. For the MQB the same applies, except instead of refractive index differences it is the difference in effective mass that is important.

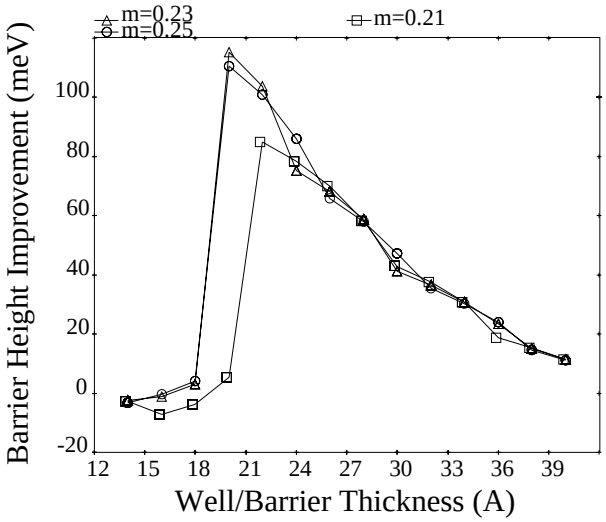

Figure 4.15: Effect of effective mass variation on the MQBs barrier height.

4.5 Influence of MQB on hole reflection

Generally, the MQB is placed in the p-cladding region of a laser to prevent the overflow of electrons out of the active region. If the MQB can reflect electrons effectively then it is possible that this same principle could prevent the injection of holes into the active region of the laser. This effect is examined in this section.

There are two bands present in the valence band, the heavy hole and light hole bands. Although these are degenerate at $k = 0$ in bulk semiconductors the degeneracy is removed in low dimensional structures where quantisation causes a splitting of the bands. The heavy hole band then becomes the lowest lying of the valence bands. For the purpose of this analysis it is necessary to consider the reflection of both heavy and light hole electrons from the MQB structure. The MQB used in this simulation has a layer structure of $\{180\ \mathring{A}; 5 \times (22, 22)\ \mathring{A}\}$ in $(Al_{0.4}Ga_{0.6})_{0.5}In_{0.5}P$. In this structure the effective mass in the barrier is taken to be $0.51m_0$ for the heavy hole and $0.15m_0$ for the light hole, while in the well the heavy hole is $0.48m_0$ and the light hole is $0.14m_0$ [60]. The barrier height is taken to be 73.2 meV. For the case of the heavy holes in the MQB the cut-off in energy is 88.7 meV, slightly larger than the bulk case, however the light holes only see a barrier of 60 meV. For the heavy hole barrier the miniband lies below the top of the barrier and the next miniband starts about 15 meV above the barrier and increases the barrier height by that much. In the case of the light holes this does not happen because the first miniband extends above the top of the barrier. Another reason for the MQB being more successful with the heavy holes in this case is that the step in mass is greater for the heavy hole case in this example. A larger step in mass between the well and the barrier could induce an equally large effect for light

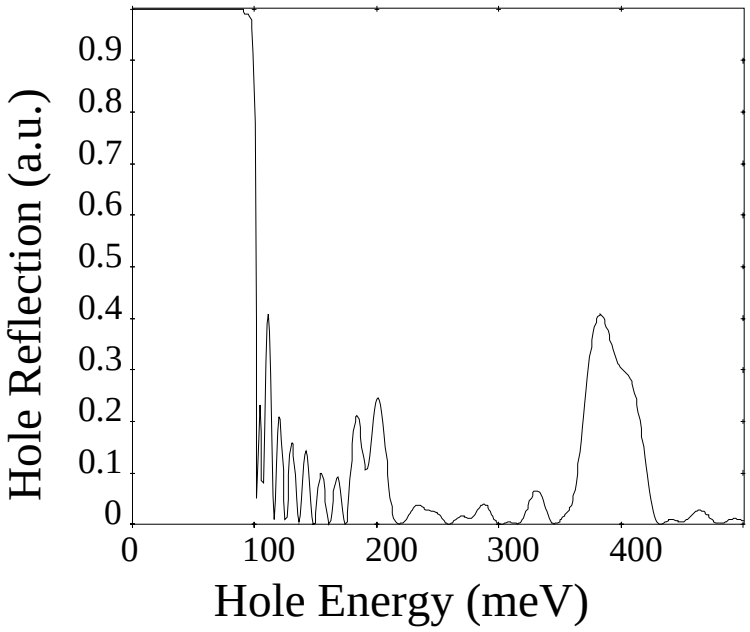

Figure 4.16: Hole reflection as a function of energy for heavy holes .

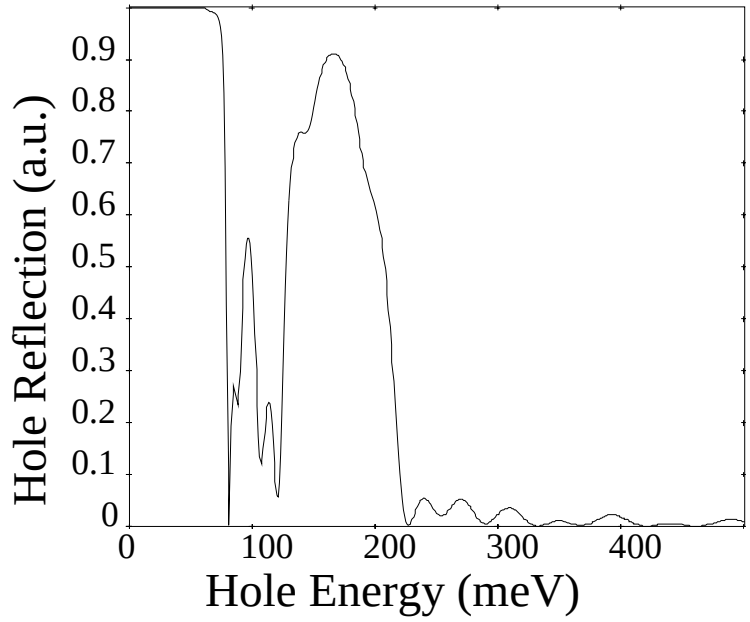

Figure 4.17: Hole reflection as a function of energy for light holes .

holes. Plots of electron reflection as a function of electron energy are shown in Figure 4.16 and Figure 4.17. Of course these results are for a MQB designed to reflect electrons i.e. a MQB placed in the p-cladding. An additional option could be to design a MQB optimised for hole reflection and place this in the n-cladding region of the visible laser. This could then assist in preventing loss of holes over the valence band offset which is 2.3 times smaller than the conduction band offset.

4.6 Summary and Conclusions

A simple effective mass model which allows mixing between electrons in , and X states was developed with the introduction of a mixing parameter, Δ. The model is simple to implement and requires less computation time than more complicated pseudopotential models. The value of the mixing parameter was found by reproducing the calculations of other researchers using more complicated models. It is found that the reflection of electrons from MQBs is not adversely affected by including , $-$ X mixing effects.

The notion of scattering was introduced into a simple effective mass model by considering scattered electrons as a loss of coherent electrons. This was implemented in the model as a reduction in the amplitude of the electron wavefunction by a factor α, which is known as the scattering parameter. α was determined from the mean free path of the electron as $\alpha = e^{x/\lambda}$ where x is the distance travelled and λ is the mean free path of the electron. As $\lambda \rightarrow \infty$ then $\alpha \rightarrow 1$ and there is no scattering. When scattering effects are accounted for it has been shown that the MQB cannot work in its conventional orientation. For the MQB to provide any increased reflection above the bulk barrier height it needs to be reversed so that electrons encounter the superlattice first.

Random fluctuations in the layer thicknesses of the MQB have little effect on the calculated reflection from the MQB, however if the layer thicknesses are systematically changed then the barrier height improvement has a strong dependence on the layer thickness. For a particular barrier material there is a minimum anti-tunnelling layer thickness required to prevent the loss of low energy electrons. For $(Al_{0.4}Ga_{0.6})_{0.5}In_{0.5}P$ this is found to be approximately 150 Å. It was found that thinner well and barrier layers could be used in a MQB if the effective mass difference between the wells and barriers is larger.

The MQB, although used to confine electrons can also inhibit the injection of holes. Since the valence band offset in AlGaInP is 2.3 times smaller than the conduction band offset a MQB designed to reflect holes could be used in the n-cladding region of a laser to prevent leakage of holes out of the active region.

Chapter 5

Photoluminescence Investigation of MQBs

5.1 Introduction

This chapter presents an attempt to measure an increase in the effective total barrier height of a MQB. The experimental measurements present a comparative luminescence study of $Ga_{0.52}In_{0.48}P/(Al_{0.5}Ga_{0.5})_{0.52}In_{0.48}P$ single quantum wells with both bulk barriers and MQBs. Comparative luminescence studies have been used previously for investigating the effectiveness of MQBs. For example, Islam *et al* [68] reported the luminescence efficiency from undoped single InGaP quantum wells (SQW) with (a) bulk AlInP barriers, (b) InGaP/AlInP MQBs and (c) a generic MQB referred to as a strain-modulated aperiodic superlattice heterobarrier (SMASH). SMASH barriers are basically MQBs in which the bandgaps of the superlattice well layers increase in successive layers away from the quantum well. The structure is designed to enhance the carrier capture in the SQW because of the *funnelling* potential of the superlattice. They found in their analysis that the room temperature luminescence from the SMASH and the MQB samples was 20 and 4 times brighter than the SQW with bulk AlInP barriers, respectively. The conclusion of their analysis is that the MQB samples increase the luminescence efficiency by providing the expected virtual barrier, although they do not provide any quantitative measure of the barrier height. Similarly, Takagi *et al* [43] have investigated the temperature dependence of the photoluminescence (PL) intensity from a GaAs/AlGaAs SQW with and without a MQB. Again, due to the increased luminescence efficiency from the MQB sample these authors concluded that an enhanced virtual potential barrier is responsible. In this chapter it is also shown that there is an increase in luminescence efficiency at room temperature in a SQW sample with MQBs when compared with the SQW sample with bulk barriers. This study differs from that of Islam *et al* and Takagi *et al* in that Arrhenius plots are used

to determine the activation energy from the SQW for both bulk barriers and MQBs, thus giving a quantitative measure of the effective barrier height. It is shown that there is no evidence for the presence of a virtual barrier. The observed increase in the SQW luminescence efficiency is instead attributed to the thermalisation of excess carriers trapped in the MQB's superlattice back into the quantum well.

5.2 Experimental Details

5.2.1 Barrier Height Measurement by Photoluminescence (PL)

The barrier height present in a SQW is defined as the total energy required to remove an electron from the ground state in the well to the conduction band edge of the barrier plus the energy required to remove a corresponding hole from its ground state to the barrier's valence band edge. This barrier height is experimentally measured as the difference between the barrier and quantum well PL peak energies. It has been previously established that the dominant loss mechanism in $Ga_{0.52}In_{0.48}P/(Al_{0.2}Ga_{0.8})_{0.52}In_{0.48}P$ quantum wells is thermal activation over this barrier. [69] As with $In_xGa_{1-x}As/GaAs$ quantum wells [70], the integrated luminescence intensities from $Ga_{0.52}In_{0.48}P/(Al_{0.2}Ga_{0.8})InP$ quantum wells of various widths as a function of inverse temperature show an Arrhenius behaviour, which when fitted, give thermal activation energies that are in agreement with those expected for thermal activation over the barrier. In principle, therefore, by measuring the luminescence as a function of temperature of a GaInP/AlGaInP SQW with both conventional bulk barriers and MQBs the effect of the MQB on the barrier height can be directly measured and compared with the bulk.

5.2.2 Description of Samples

Two $Ga_{0.52}In_{0.48}P/(Al_{0.5}Ga_{0.5})_{0.52}In_{0.48}P$ SQW samples were measured, one with bulk barriers of $(Al_{0.5}Ga_{0.5})_{0.52}In_{0.48}P$ (SQW$_{Bulk}$) and the other with MQBs (SQW$_{MQB}$). The SQW$_{Bulk}$ sample consisted of a 50 Å $Ga_{0.52}In_{0.48}P$ well with 0.2 μm $(Al_{0.5}Ga_{0.5})InP$ barriers. The SQW$_{MQB}$ sample also consisted of a 50 Å $Ga_{0.52}In_{0.48}P$ well with a 150 Å $(Al_{0.5}Ga_{0.5})InP$ anti-tunnelling layer followed by five pairs of $(Al_{0.5}Ga_{0.5})InP$ / $Ga_{0.52}In_{0.48}P$, 35 Å and 15 Å thick, respectively, and a further 0.16 μm of $(Al_{0.5}Ga_{0.5})InP$ on either side. A schematic representation of the samples is shown in Fig. 5.1. The overall thickness of both SQW samples is identical. Both samples are nominally undoped and were grown by conventional atmospheric metal organic vapour phase epitaxy at a growth temperature of 760°C on a Si-doped GaAs substrate misoriented by 3^o towards the (111)A direction. This substrate misorientation, coupled with the high growth temperature, ensures that a high degree of group III sublattice disorder is achieved. [71] Cleaved edge transmission electron microscopy (TEM) confirmed that the measured

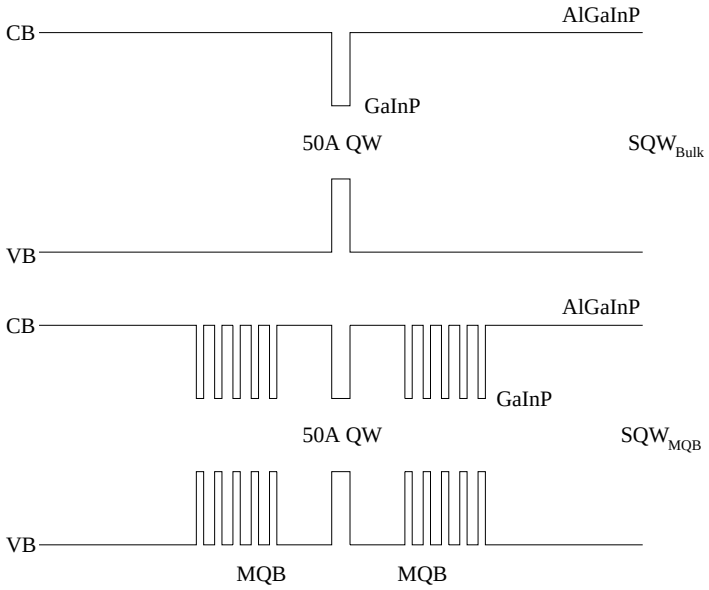

Figure 5.1: Schematic representation of the two samples described in the text.

layer thicknesses for the MQBs were within $\pm$ 2 Å of the nominal design values.

By using a simple effective mass model [17] as described in the previous chapter and assuming $Ga_{0.52}In_{0.48}P$ and $(Al_{0.5}Ga_{0.5})InP$ electron effective masses of $0.11m_0$ and $0.23m_0$ respectively, with a conduction band offset of 213.5 meV, the MQB structure was designed to have a total thickness of less than 400 Å. Fig. 5.2 shows a plot of the electron reflection as a function of electron energy for this MQB. If a stringent cut-off criterion for the electron reflection of 99.9% is used, then the estimated virtual barrier height is 77.3 meV greater than the intrinsic conduction band offset.

5.2.3 Experimental Set-Up

The continuous wave PL spectra were collected from the SQW samples in two configurations. For the first, both samples were excited above the $(Al_{0.5}Ga_{0.5})_{0.52}In_{0.48}P$ barrier energy using the 488 nm line of an Ar^+ ion laser, while in the second the SQW's were excited resonantly with a tunable dye laser. This latter mode of excitation creates a population of electrons and holes only in the SQW itself. Initial PL spectra were also taken at 4.2 K in a helium bath cryostat using 488 nm excitation. The temperature dependent measurements from 10 K to room temperature were taken using a closed cycle cryostat. In all cases the luminescence signal was dispersed through a *SPEX 500M* spectrometer and detected using a silicon charge coupled device (CCD). Fig. 5.3 shows a schematic representation of the experimental set-up.

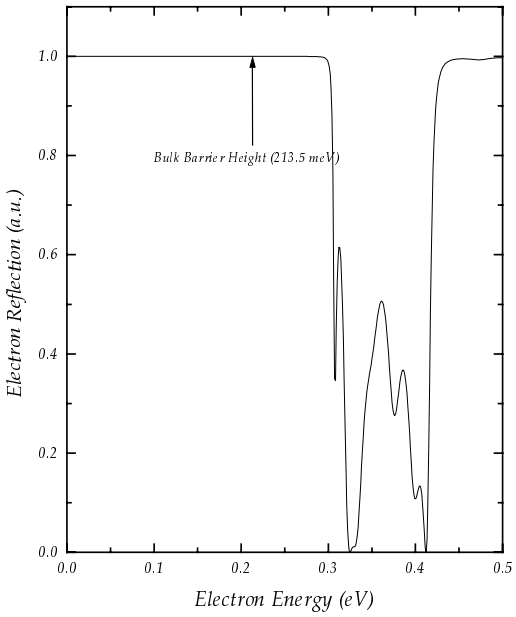

Figure 5.2: Plot showing the expected electron reflection from the SQW$_{MQB}$ structure.

5.3 Results

A comparison of the 4.2 K PL spectra for the SQW$_{Bulk}$ and SQW$_{MQB}$ samples shows that the well and barrier emissions for both samples are almost identical (see Fig. 5.4), indicating practically identical quantum well structures for both samples. The quantum well emission occurs at 2.067 eV for the SQW$_{Bulk}$ and 2.065 eV for the SQW$_{MQB}$ with full widths at half maximum (FWHM) of 15 meV and 12 meV respectively. The barrier emissions occur at 2.328 eV and 2.329 eV respectively for the SQW$_{Bulk}$ and SQW$_{MQB}$ samples. From the quantum well and barrier emission energies, the barrier height for this quantum well is determined to be 262 meV. Additional peaks located 32 meV and 51 meV below the bulk barrier peak in both samples are longitudinal optical (LO) phonon replicas of the bulk emission. The origin of the background emission at lower energy, particularly for the SQW$_{MQB}$ sample, is unknown although it could be acceptor related or related to ordering induced emissions that can occur in these materials. Peaks located 47 meV below the emission peak of the quantum well in both structures are also attributed to a phonon replica as phonon energies for the InP-like and GaP-like LO-phonons in GaInP have been measured at 44.5 and 47 meV respectively. [72] For the SQW$_{MQB}$ sample the MQB emission is located at 2.203 eV with a shoulder at 2.187 eV. From the comparison of the 4.2 K PL of these two samples it is concluded that the quantum wells are almost identical and that a fair comparison can be made to measure the influence of the MQB on carrier confinement.

Arrhenius plots of the integrated PL intensity as a function of temperature for both

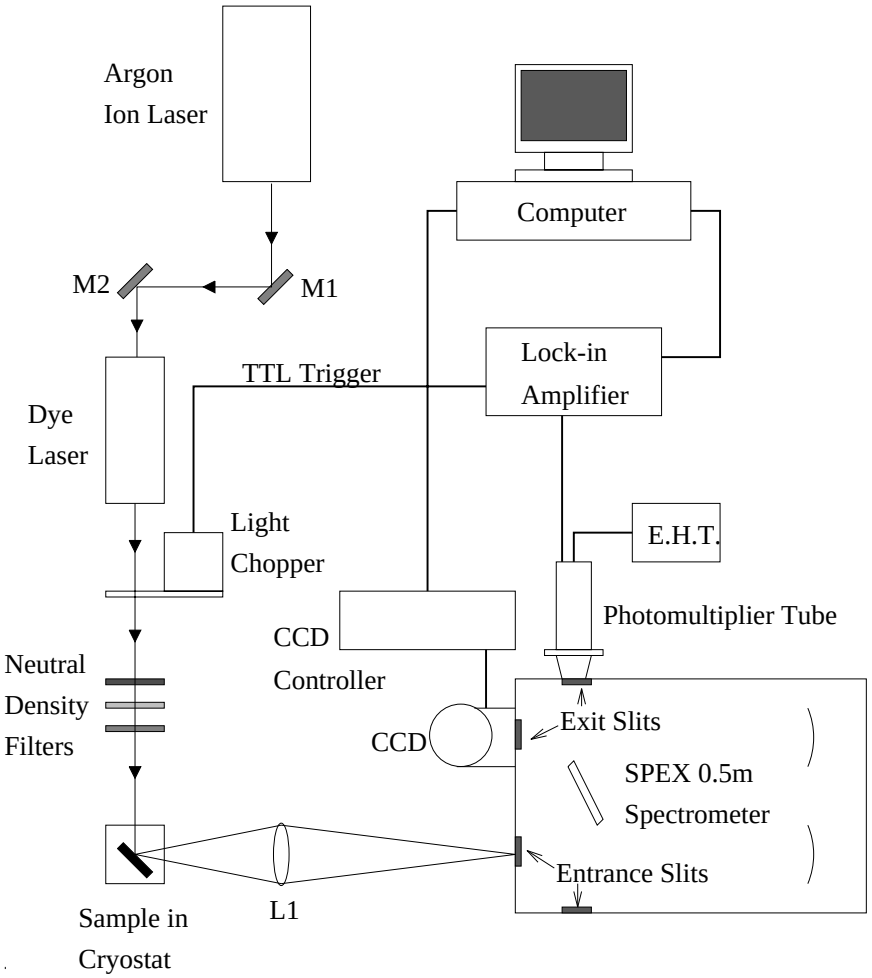

Figure 5.3: Experimental set-up used to take the photoluminescence spectra.

of the samples when excited above the barrier energy with the 488 nm line of the Ar^+ ion laser are shown in Fig. 5.5. There is a striking difference in behaviour between the two samples since the intensity is 443 times smaller at 300 K than at 10 K for the SQW_{Bulk} sample compared to a reduction in intensity of only 61 times for the SQW_{MQB} sample, as outlined in Table 5.1. This observation alone seems to support the Bragg confinement of carriers by the MQB. This is however, shown not to be the case when the data is examined in more detail. The SQW_{Bulk} sample shows a slight increase in PL intensity at higher temperatures before dropping off sharply as room temperature is reached. Comparing this with the same plot for sample SQW_{MQB}, the PL intensity begins to fall off gradually before peaking at 140 K and then falling off sharply as room temperature is reached. This resonant increase in PL intensity is indicative of the thermal emission of carriers from the MQB superlattice and their

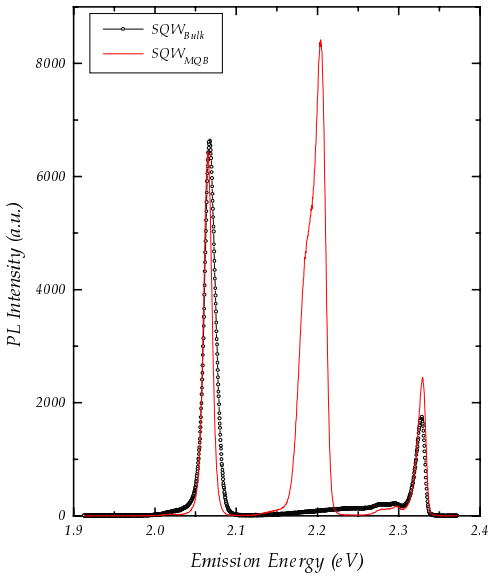

Figure 5.4: 4.2 K PL Spectra for the MQB and Bulk Barrier samples respectively.

Excitation Mode	SQW_{Bulk} ΔI (T=10 to 300 K)	SQW_{MQB} ΔI (T=10 to 300 K)
488 nm	$I_0 \times 443^{-1}$	$I_0 \times 61^{-1}$
Dye Laser	$I_0 \times 40^{-1}$	$I_0 \times 37^{-1}$

Table 5.1: Factors by which the 10 K PL intensities are reduced in going to room temperature under the two modes of excitation as described in the text.

subsequent recapture by the lower energy state of the quantum well. This process of thermalisation and recapture has been previously seen in InGaAs/GaAs quantum well structures. [73] Further evidence of this carrier transport between the MQB superlattice and the quantum well is given by the 50 K photoluminescence excitation (PLE) spectrum of sample SQW_{MQB}. This spectrum, shown in Fig. 5.6, shows that when the excitation laser energy is resonant with the quantum well emission energy, a measurable recombination is detected at the peak emission wavelength of the MQB. This is an unusual arrangement for a PLE measurement where the detection energy is customarily at lower energy than the excitation source. This measurement confirms that the reverse transport process is possible in that carriers in the quantum well can be thermalised into the barrier and captured by the superlattice of the MQB. These carrier transport effects increase the difficulty of estimating the activation energy out of the well. Such effects, however, can be easily avoided by only creating a population of carriers in the quantum well itself by resonantly exciting these carriers using a tunable dye laser.

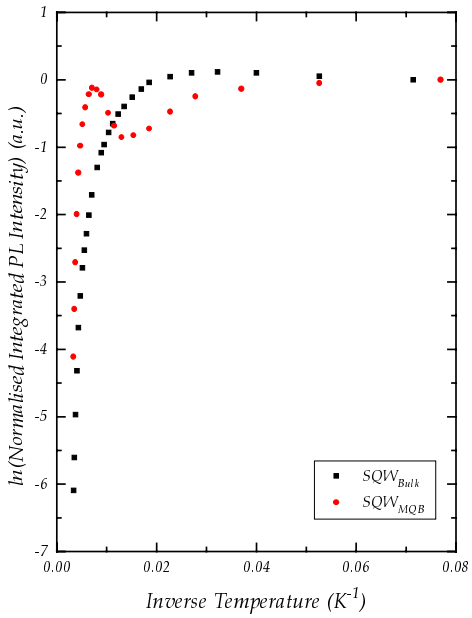

Figure 5.5: PL Spectra for the MQB and Bulk Barrier samples using 488 nm excitation.

Figure 5.7 shows a plot of the integrated PL intensity for both samples when the quantum well is resonantly excited using a dye laser. Unlike the previous excitation mode the behaviour of both samples is now very similar. In both cases the PL intensity gradually reduces with increasing temperature until a temperature is reached when the fall-off in PL intensity is very sharp. Changes in intensity prior to quenching are no longer evident. The maximum difference in intensity between the two samples is only a factor of 2.8 and occurs at a temperature of 170 K. The total reduction in intensity in going from 10 K to room temperature for both samples is virtually identical ($\sim$40 times less) as shown in Table 5.1.

5.4 Analysis of Arrhenius Plots

The Arrhenius behaviour shown in Fig. 5.7 can be fitted across the entire temperature range using a simple model that assumes two thermally activated loss mechanisms. [69] A low temperature mechanism characterised by an activation energy, E_A and a higher temperature mechanism characterised by an activation energy, E_B. The luminescence intensity (I_{PL}) as a function of temperature, T, is given by

$$I_{PL}(T) = \frac{I_0}{1 + C_A e^{\frac{-E_A}{kT}} + C_B e^{\frac{-E_B}{kT}}} \tag{5.1}$$

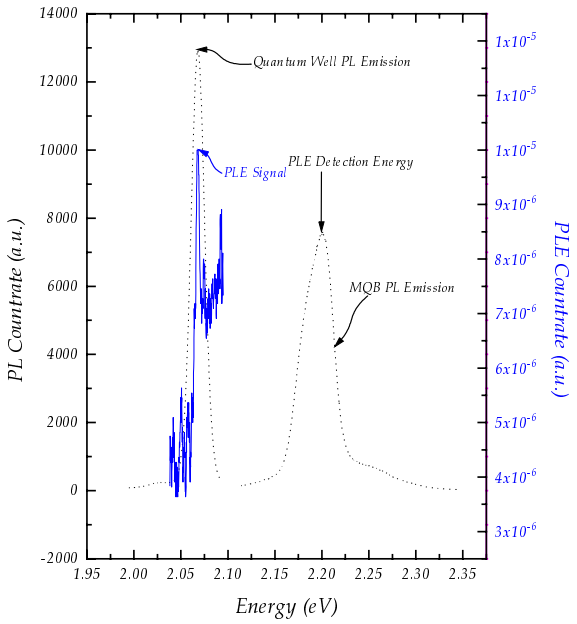

Figure 5.6: PL Emission Spectrum showing emission from the MQB when the quantum well is resonantly excited.

	I_0	C_A	E_A (meV)	C_B	E_B (meV)	E_{PL} (eV) at 4.2 K	$E_{PL} + E_B$ (eV)
SQW_{Bulk}	0.66	$10^{0.77}$	8.3 ± 2	$10^{2.66}$	63.2 ± 8	2.067	2.130 ± 0.01
SQW_{MQB}	0.97	$10^{0.99}$	17.0 ± 1	$10^{3.38}$	109.5 ± 8	2.065	2.175 ± 0.01

Table 5.2: Fitting parameters used to fit the Arrhenius plots described in the text.

where I_0 is the PL intensity at 4.2 K, k is Boltzmann's constant, C_A and C_B are the ratios of the 4.2 K radiative lifetime to the high temperature non-radiative lifetime for mechanisms A and B respectively. The prefactors C_A and C_B are assumed to remain constant as a function of temperature. The results of a least squares fit of Eqn. 5.1 to the experimental data are shown in Fig. 5.7 as solid lines, while the fitted parameters are given in Table 5.2. The fits to the experimental data are good enough to allow a quantitative comparison to be made between the two structures. The nature of the low temperature mechanism is not clear although it may be associated with the thermalisation of carriers from band-edge fluctuations due to either alloy variations or well-width fluctuations followed by non-radiative recombination, possibly at the quantum well interfaces. The higher temperature activation process is expected to be dominated by the thermal loss of carriers out of the quantum well.

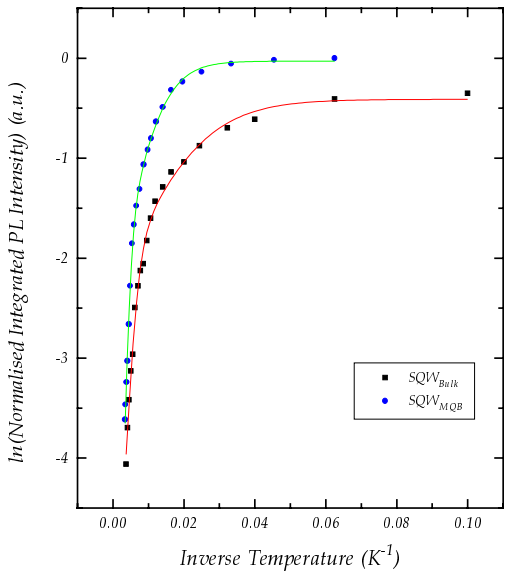

Figure 5.7: PL Spectra from the MQB and Bulk Barrier samples when the quantum well is resonantly excited using a dye laser. The solid line represent fits to the data using Eqn 5.1.

5.5 Discussion

From the fitted parameters shown in Table 5.2, the activation energy, E_B, for the SQW$_{MQB}$ sample is almost a factor of two larger than the SQW$_{Bulk}$ sample. This would seem to suggest that the MQB has produced an enhanced barrier height, but it is important to note that both activation energies are less than half the 262 meV barrier height expected from the PL emission energies for the SQW$_{Bulk}$ sample. Therefore, the major loss mechanism for carriers in both these SQW samples is not simply activation out of the quantum well as anticipated, but is instead complicated by the presence of a competing and less energetic loss mechanism. Similar behaviour is also observed in InGaAs quantum wells with AlGaAs barriers. [70] In the InGaAs/AlGaAs system the major loss mechanism is by non-radiative recombination via traps in the barrier or interface which are assumed to be associated with Al-O complexes. It is feasible that the high aluminium composition in the AlGaInP SQWs discussed here introduces a similar loss mechanism. It is also possible that an additional loss mechanism might involve the non-radiative loss of electrons via X-states in the barrier due to the proximity of the X-minima to the , minimum at this aluminium composition, a loss mechanism that has been highlighted recently by Smowton and Blood. [4] Such a mechanism can give rise to a significant proportion of the large excess leakage currents measured in tensile strained quantum well visible lasers. [34] As pointed out in Chapter 2, and stressed

again here, the assumption that the poor thermal characteristics of visible lasers is merely due to the small , -minima band offsets is an over-simplification and greater attention should be paid to other possible loss mechanisms.

Even though the measured activation energy for the SQW_{MQB} sample is greater than that of SQW_{Bulk} it is not correct to attribute any significance to this difference since both activation energies are much lower than the experimentally measured barrier height of 262 meV. The important figure of merit for a quantum well for use in a laser device is its room temperature luminescence efficiency. The combination of the activation energies, E_B, and prefactors, C_B, for both samples ensures that their room temperature luminescence efficiencies are virtually identical when the quantum well is resonantly excited. In this sense both samples are indistinguishable and the MQB shows no additional effect over the bulk barrier at room temperature. This report contrasts with those of Islam *et al* and Takagi *et al* who report significant enhancements of luminescence efficiency in MQB quantum well samples at room temperature. However, in their measurements an excitation wavelength of 488 nm was used and so the observed increase in PL intensity in their MQB samples is almost certainly due to the capture of carriers that have thermally escaped from the MQB's superlattice.

It should be noted here that in hindsight the samples used in the experiments described in this chapter are flawed for two reasons. Firstly, by having MQBs on both sides of the quantum well a confining potential can be created on either side of the quantum well which can introduce new confined states above the quantum well at energies lower than any anticipated barrier height improvement due to the MQBs. Electrons could then escape over the barrier via these confined states, rendering the MQBs useless as electron reflectors. For this reason it would have been more instructive to have the MQB on one side of the quantum well only. Secondly the aluminium composition used in the barrier material seems to have more complicated leakage and recombination paths than would have been observed if the aluminium composition in the barrier was limited to 20%. If 20% aluminium was used in the barriers then electron leakage over the heterobarrier would be the only thermally activated process. [69]

5.6 Summary and Conclusions

The luminescence efficiency, as a function of temperature, of two comparable single quantum well (SQW) samples, one with bulk barriers and one with MQBs, was presented in this chapter. Two different excitation sources were used, the first was with the 488 nm line of an Ar^+ ion laser to excite carriers above the barrier energy and the second was using a dye laser to resonantly excite carriers in the ground state of the quantum well. It was shown that when the 488 nm excitation source was used the MQB sample showed a much larger room temperature luminescence efficiency than its bulk

barrier counterpart. This is in agreement with studies done by other researchers using the same excitation source. [68, 43] Their explanation for the increased luminescence efficiency is an increased barrier to carrier overflow due to the presence of the MQB. Analysis of Arrhenius plots for the samples described in this chapter indicate that the mechanism responsible for the increased luminescence efficiency is the thermalisation of excess carriers trapped in the MQB superlattice back into the quantum well and not the expected MQB effect of an increased barrier height. Further investigation of the samples by resonantly exciting the ground state in the quantum well with a tunable dye laser shows that the leakage mechanism is different to the expected thermalisation of carriers over the barrier. Instead a competing lower energy mechanism, of unknown origin but exhibiting similar characteristics to a similar mechanism observed in the InGaAs/AlGaAs system, is shown to be responsible for the carrier leakage. There is no significant difference in the luminescence efficiency between the two samples and the MQB shows no improvement over its bulk counterpart.

There are two novel aspects in the approach to this problem that have not been explored in the literature previously. The first is the systematic measurement of the PL intensity as a function of temperature to allow a quantitative measurement of the activation energy out of the quantum well, and hence the surrounding barrier height. The second is the use of a tunable dye laser to resonantly excite carriers in the ground state of the quantum well. This technique showed that the activation of carriers out of the well was not over the barrier but involved a lower energy mechanism. This result is contrary to expectations and could be a result of the proximity of the X-minima to the , minimum at the aluminium composition used in the barriers.

In conclusion, there is no observed barrier height improvement with the inclusion of MQB structures. It would be beneficial to repeat the experiments described in this chapter with a smaller aluminium composition in the barrier to ensure that carrier leakage over the barrier is in fact the dominant leakage mechanism. In the next chapter a different approach is taken to try to measure a barrier height improvement due to the MQB by measuring the activation over intrinsic barriers in n-i-n tunnel diodes from the current-voltage (I-V) characteristics as a function of temperature.

Chapter 6

Carrier Transport in n-i-n Diodes

6.1 Introduction

Various techniques have been applied to investigate the improvement in barrier height due to a MQB. One such technique is the direct comparison between the I-V characteristics of a bulk and a MQB n-i-n diode. Iga *et al.* [45] were the first to perform such a comparison and based on their observation of a higher turn on voltage for an n-i-n diode with a MQB intrinsic region they concluded that this was a result of an increased barrier height due to the MQB effect. As a qualitative comparison between devices this approach is quite reasonable but from a single measurement at 77 K it is impossible to ascertain any quantitative information about the barrier heights in the intrinsic region.

Recent papers by Chaabane *et al.* [74, 75, 76] outline techniques for investigating the transport properties of electrons over bulk barriers in GaAs/AlGaAs as well as a means of estimating the barrier height encountered by the electrons in n-i-n diodes. These techniques are adopted here for comparing the barrier heights obtainable from bulk and multiquantum barriers in AlGaInP. In this chapter these techniques are presented and the various electron transport regimes are discussed. The sample set designed and fabricated is detailed along with the experimental set-up for measuring the I-V characteristics of n-i-n diodes as a function of temperature. Results are presented for bulk barrier diodes of various alloy composition and MQB barrier diodes where the superlattice period is varied from $5 \times (14,14)\mathring{A}$ to $5 \times (32,32)\mathring{A}$.

6.2 Transport Mechanisms

6.2.1 Fowler-Nordheim Tunnelling

When the electric field is sufficiently high across an insulating barrier then electrons can gain enough energy to tunnel straight through the barrier. This form of tunnelling is known as Fowler-Nordheim (F-N) tunnelling and is illustrated in Fig. 6.1. In the n-i-n diodes described in this chapter the intrinsic region is considered to be like an insulator and as a result it is assumed that all of the electric field is dropped across the barrier. Because the barriers are so thin it is easy to induce F-N tunnelling at low temperatures.

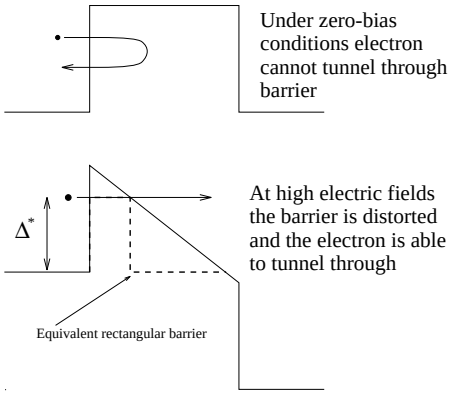

Figure 6.1: The Fowler-Nordheim Tunnelling process.

The barriers are considered rectangular and the current density, J, is given by

$$J = \frac{q^3 F^2}{8\pi h \Delta^*} exp\left(-\frac{8\pi\sqrt{2m^*}(\Delta^*)^{3/2}}{3hqF}\right) \tag{6.1}$$

where h is Planck's constant, q is the electronic charge, F is the electric field, m^* is the electron effective mass and Δ^* is the barrier height.[75, 77] The F-N regime can therefore be recognised from the region of linear behaviour of $ln(J/F^2)$ versus F^{-1} as

$$ln\left(\frac{J}{F^2}\right) = a - \frac{b}{F}$$

The measurement of the slope

$$b = \left(\frac{8\pi\sqrt{2m^*}}{3hq}\right)(\Delta^*)^{3/2}$$

yields the barrier height Δ^* which should be consistent with the value of Δ^* obtained

by extrapolation to $F^{-1} = 0$

$$a = ln\left(\frac{q^3}{8\pi h\Delta^*}\right)$$

Although this technique provides a measure of the barrier height, the values obtained for Δ^* from the slope, b, and the intercept, a, frequently differ from each other. The main source of this discrepancy is estimating the electric field across the barrier. This barrier height measurement technique is also unsuitable for n-i-n diodes having MQB intrinsic regions since the high field distortion of the MQB eliminates any possibility of observing a barrier height increase due to the MQB effect. To compare the MQB with bulk barriers a technique is required for measuring the effective barrier height at sufficiently low fields that any MQB effect is not lost by distortion of the barrier.

6.2.2 Phonon Assisted Tunnelling

As the temperature increases the F-N tunnelling becomes temperature dependent and the Fermi distribution ($f(E,T)$) of the electrons becomes important. The transport becomes dominated by phonon assisted tunnelling where an electron of energy E is transmitted with a tunnelling probability

$$T(E) = exp\left(-\frac{4\pi}{h}\sqrt{2m^*}\int_x \sqrt{qV(x) - E}dx\right)$$

where $qV(x)$ represents the variation of the potential barrier with depth x. The tunnelling current is

$$J = qv_n \int_E N_D f(E,T)T(E)dE$$

where N_D is the electron density in the conduction band of the material that surrounds the barrier and v_n is the electron thermal velocity.[47, 75, 78] This regime is not a good measure of the true barrier height of a MQB because the carrier transport is through the barrier by means of tunnelling and not over the barrier.

6.2.3 Thermionic Emission

In semiconductor-insulator-semiconductor (SIS) structures at low voltages and high temperatures the principal conduction mechanism is thermionic emission of electrons over the barrier. The current density at temperature T due to thermionic emission is given by the Richardson equation

$$J = A^*T^2 exp\left(-\frac{q\Delta^*}{kT}\right) \tag{6.2}$$

where A^* is the effective Richardson constant given by

$$A^* = qm^*k^2/2\pi^2\hbar^3$$

and Δ^* is the apparent barrier height.[79, 80, 81] The linearity of the plot $ln(J/T^2)$ versus T^{-1} is indicative of an emission process having an activation energy or apparent barrier height, Δ^*. Δ^* is found from the slope of the linear portion of the $ln(J/T^2)$ versus T^{-1} graph. If the slope remains constant as a function of bias then the emission process is thermionic and Δ^* corresponds to the barrier height from the quasi-Fermi level for electrons to the bottom of the conduction band in the intrinsic barrier. If the slope reduces with increasing bias then other emission processes, such as Poole-Frenkel emission, dominate the transport and Δ^* measured in this regime does not give the barrier height of interest for quantitatively comparing the barrier heights of MQB and bulk barriers. A schematic representation of the thermionic emission process is given in Fig. 6.2. This is the transport regime of interest for critically comparing the barrier

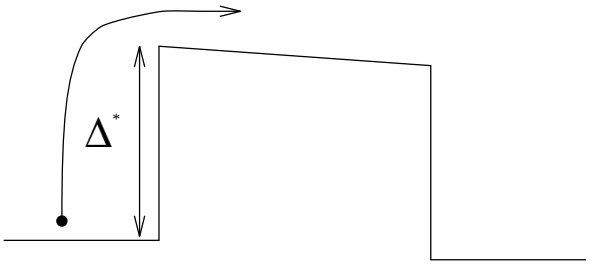

Figure 6.2: Thermionic Emission over an insulating barrier.

heights of MQBs and bulk barriers in n-i-n diodes. Here the barrier height is given from the quasi-Fermi level to the barrier band edge since the transport of carriers is over the barrier. In addition this transport regime is characterised by low applied bias which is essential for having a flat band condition across the MQB intrinsic region.

6.2.4 Poole-Frenkel Emission

Poole-Frenkel (P-F) emission is governed by field or thermal ionisation of trap states in the barrier. Here the current density, J, is expressed as

$$J = qe_nN_Tw \tag{6.3}$$

where N_T is the density of defects involved in a given thickness w of the barrier and e_n is the electron emission rate from the defect into the barrier conduction band

$$e_n = \sigma v_n N_C exp\left(\frac{-E_i}{kT}\right)$$

where E_i is the associated ionisation energy, σ is the electron capture cross section and N_C is the density of states in the barrier conduction band.[75] Thus, all defects located in the thickness w are always filled by tunnelling with the rate of filling being much larger than the rate of ionisation. In the presence of the electric field, F, the ionisation barrier, E_i, can be decreased. For a Coulombic binding potential, E_i varies with F as

$$E_i = E_{i0} - \alpha\sqrt{F} \tag{6.4}$$

with

$$\alpha = \sqrt{\frac{q}{\pi\epsilon}}$$

where ϵ is the dielectric constant and E_{i0} is the defect ionisation energy under zero field. When the P-F mechanism is dominant one expects J to vary with temperature as e_n

$$J = J_0 exp\left(\frac{-E_i}{kT}\right)$$

with

$$J_0 = qN_T w\sigma v_n N_C.$$

The ionisation energy, E_i, can be calculated from a graph of $ln(J)$ versus T^{-1} and the P-F transport mechanism can be recognised as a dependence of E_i on $F^{1/2}$. If the binding potential is not Coulombic then one should get a slope of the plot $E_i(F^{1/2})$ different from $\alpha = 2.19\times10^{-4}\ V^{1/2}cm^{1/2}$.[75] A schematic of the Poole-Frenkel emission process is given in Fig. 6.3. Again this transport regime is not useful for comparing the barrier heights of MQBs and bulk barriers. The transport of carriers is dependent on traps within the barrier which is a material dependent parameter and the measured barrier height is typically less than the actual barrier height in the device.

6.3 Experimental Set-up

The I-V data from the designed n-i-n samples was collected in a closed cycle Stirling cryostat as shown in Fig. 6.4. This apparatus allowed the I-V measurements to be taken between 60 K and 310 K. Temperature feedback is via a thermistor mounted on the cold finger of the cryostat. With this arrangement the temperature can be accurately controlled to within ±0.5 K. During the measurement the cryostat system is pumped down to 10^{-6} Torr and current is supplied by a Philips PLPS2000 Power supply which

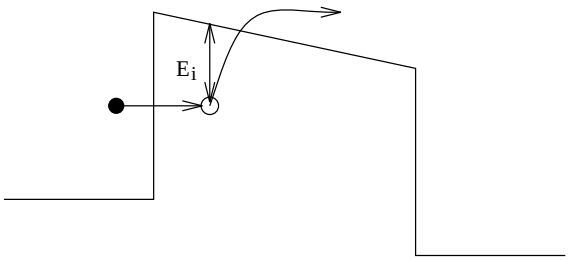

Figure 6.3: Poole-Frenkel Emission from traps located within an insulating barrier.

is current limited to 500 mA. All the data is collected in real time using Labview [1] virtual instruments and the temperature is manually adjusted using a variac attached to the cryostat compressor.

The entire top and bottom surfaces of the n-i-n diodes are used as the contact areas and these measure 300 μm $\times$ 500 μm. The devices are mounted epi-side up on copper cubes and bonded to TO-5 headers which are easily inserted into the sample mount of the cryostat. The samples are all grown on n-type GaAs substrates and consist of a 0.2 μm GaAs buffer layer (n=2$\times$ 10^{18} cm^{-3}), a 0.05 μm $Ga_{0.5}In_{0.5}P$ layer (n=2$\times$ 10^{18} cm^{-3}), 0.05 μm $Ga_{0.5}In_{0.5}P$ spacer layer (nominally undoped, n.u.d.), an intrinsic barrier (undoped) layer (this is the only layer that is changed in all of the samples and is the only layer that is described when talking about the n-i-n diodes in the following sections), a 0.05μm $Ga_{0.5}In_{0.5}P$ spacer layer (n.u.d), a 0.05 μm $Ga_{0.5}In_{0.5}P$ layer (n=2$\times$ 10^{18} cm^{-3}) and a 0.2 μm GaAs capping layer (n=2$\times$ 10^{18} cm^{-3}). The spacer layers are used to prevent shorting of the diodes by ensuring that the entire barrier region remains undoped.

It is important to know how the dopants in the devices will behave as a function of temperature so that the effects of carrier freeze-out can be accounted for in the analysis. To determine this behaviour a test structure consisting of a GaAs buffer layer, a 200 Å GaInP barrier and a GaAs capping layer (all doped n=2$\times$ 10^{18} cm^{-3}) was measured between 60 K and 280 K. From this sample the resistance was observed to be 0.42 Ω at 60 K and 0.48 Ω at 280 K. The change in resistance of 0.06 Ω over a 200 K temperature range is considered small enough to be neglected from the analysis of the samples. The nature of the contact to all of these devices is such that surface leakage currents could be a problem and distort the data analysis. To check that the actual current in the

[1] Labview is a trademark of National Instruments.

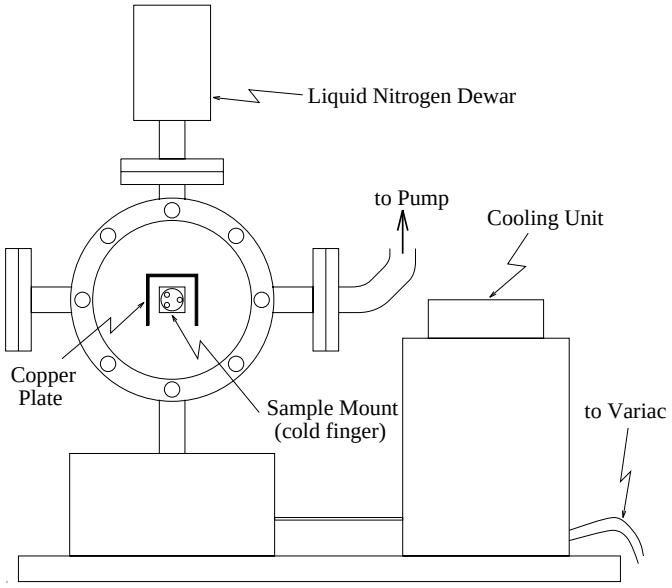

Figure 6.4: Closed cycle Stirling cryostat used for cooling device samples.

n-i-n diodes is not dominated by surface leakage currents a series of measurements was made on devices of varying area to see if the current scaled with the area or with the circumference of the devices. If the current scales with the area then surface leakage currents can be deemed negligible. The devices under test were all 300 μm wide and the lengths varied as 200 μm, 500 μm, 1000 μm and 1500 μm. The data for these samples was taken with a Tektronix 577 Curve tracer in DC mode with the sample under test immersed in liquid nitrogen. The chip dimensions were checked with a microscope and 3 chips per length were inspected. It was found that the current scaled linearly with the area for currents above the minimum deliverable current (10^{-6} A) of the power supply used with the cryostat measurement set-up. Hence, surface leakage currents can be neglected from the analysis for data taken with the cryostat set-up described above.

6.4 Bulk AlGaInP n-i-n Diodes

6.4.1 Description of Sample Set

Five n-i-n diodes were designed with $(Al_xGa_{1-x})_{0.5}In_{0.5}P$ intrinsic barrier regions. These samples have aluminium compositions of x =0.4, 0.5, 0.6, 0.7 and 1.0 respectively and were grown by MOVPE to have a disordered lattice structure. The purpose of the sample set was to investigate the different transport regimes in AlGaInP using the three models described in Section 6.2 and to determine the barrier heights as a function of composition using the thermionic emission model. This model is shown to provide

acceptable accuracy in determining the GaInP/AlGaInP band-offsets for both direct and indirect bandgap AlGaInP. A schematic representation of the conduction band of an n-i-n diode under zero bias is shown in Fig. 6.5, while Fig. 6.6 shows the diode with an applied bias of 0.1 V. The intrinsic barrier in these figures has 40% aluminium in the AlGaInP and the measured barrier height is the difference in energy between the Fermi level and the band-edge in the barrier. This barrier height, from the diagram, is between 150 and 170 meV and closely approximates the conduction band offset between the GaInP and the AlGaInP.

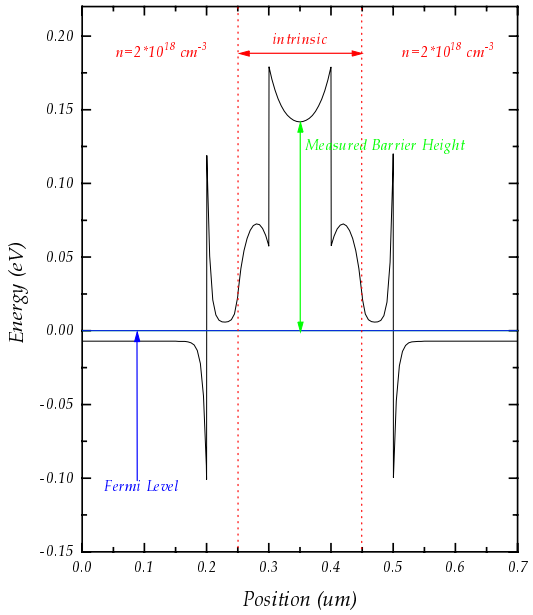

Figure 6.5: Device Structure for a Bulk $(Al_{0.4}Ga_{0.6})_{0.5}In_{0.5}P$ n-i-n Diode under zero bias conditions.

6.4.2 Fowler-Nordheim Tunnelling as a function of Temperature

The I-V characteristics for each of the five bulk barrier n-i-n diodes was measured under forward (positive bias on epi-layer) and reverse bias conditions from 60 K to 300 K. As described in Section 6.2.1, the Fowler-Nordheim Tunnelling regime can be recognised from the linearity of the $ln(J/F^2)$ versus $1/F$ plot of the data, where J is the current density and F is the electric field. The data may also be represented in the form of $ln(I/V^2)$ versus $1/V$ as shown in Fig. 6.7. The slopes of the regression lines shown in red in Fig. 6.7 allow the apparent barrier height as a function of temperature to be determined. It is assumed that the entire field is dropped across the barrier and this allows the field to be determined from the applied voltage. The slopes of the regression

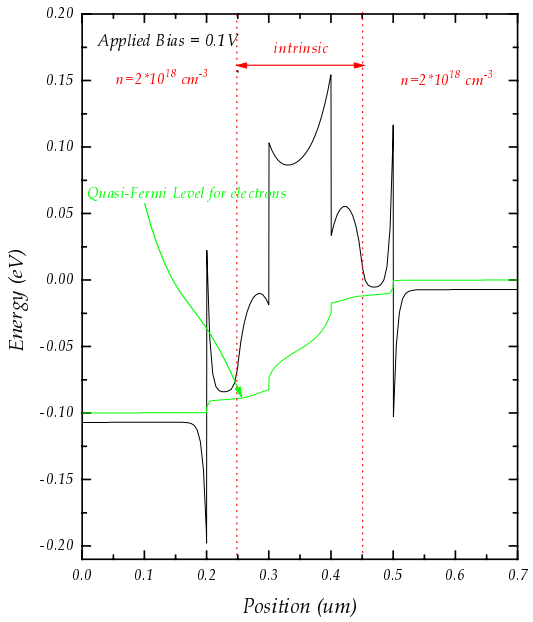

Figure 6.6: Device Structure for a Bulk $(Al_{0.4}Ga_{0.6})_{0.5}In_{0.5}P$ n-i-n Diode with an applied bias of 0.1 V.

lines are divided by the barrier thickness and the resulting number is equivalent to

$$\left(\frac{8\pi\sqrt{2m^*}}{3hq}\right)(\Delta^*)^{3/2}$$

where Δ^* is the apparent barrier height, m^* is the effective mass in the barrier, h is Planck's constant and q is the electronic charge. This analysis was repeated for each of the five bulk barrier samples and the results are displayed in Fig. 6.8. From this figure, the apparent barrier height as a function of temperature decreases almost linearly for the barriers with 40% and 50% aluminium. The other three barriers show no obvious trends in the apparent barrier height variation with temperature. This is presumably due to the fact that the barrier is an indirect bandgap material at these compositions.

The analysis shows that typically fields in excess of 5 MV/m^2 are required to induce Fowler-Nordheim Tunnelling in AlGaInP. From Fig. 6.8 it is observed that F-N tunnelling can occur at temperatures up to 215 K for the 40% aluminium composition, and up to 260 K for the 50% aluminium composition. The other three compositions, 60%, 70% and 100% aluminium did not show any linear dependence on the $ln(I/V^2)$ versus $1/V$ plot at temperatures above 110 K, 150 K and 120 K respectively. It is unexpected that the barrier height, as determined from the Fowler-Nordheim Tunnelling Model, exhibits such a strong linear dependence on temperature since no temperature dependence is expected from the governing equation. This experimental observation

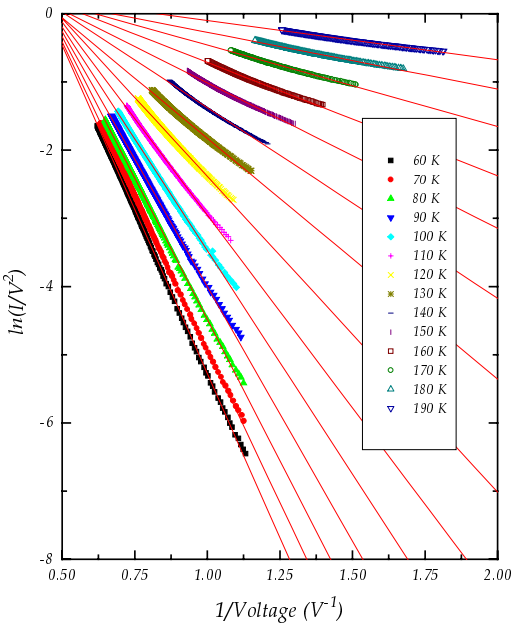

Figure 6.7: Fowler-Nordheim Data for n-i-n tunnel diode with $(Al_{0.4}Ga_{0.6})_{0.5}In_{0.5}P$ barrier. Red lines are linear regression fits to the experimental data.

supports the proposition of Lenzlinger and Snow [82] that the barrier height is temperature dependent to explain the temperature dependence of the Fowler-Nordheim tunnelling currents. This is the first time that the temperature dependence of the barrier height in AlGaInP has been demonstrated for the Fowler-Nordheim regime.

This technique is useful for determining the F-N transport regime but the apparent barrier height determined from the analysis significantly underestimates the true barrier height. It is therefore not a useful technique for comparing the barrier heights of MQBs and bulk barriers.

6.4.3 Barrier Height Estimation as a function of Bias using the Thermionic Emission Model

To measure the barrier height of the devices the data was organised into plots of $ln(I/T^2)$ versus $1000/T$ (thermionic emission or TE plots) as a function of applied bias. An example of such a plot is given in Fig. 6.9 for an n-i-n diode with a 1000 Å $(Al_{0.4}Ga_{0.6})_{0.5}In_{0.5}P$ intrinsic barrier region. The activation energy over the heterointerface between the GaInP and AlGaInP is determined from the slope of the linear portion of the TE plot multiplied by the Boltzmann constant, k, in eV. When thermionic emission is the dominant transport mechanism then the slopes of the TE plots are constant with increasing bias as can be seen from Figs. 6.9 and 6.10. The measured activation energy corresponds to the difference in energy between the quasi-Fermi level

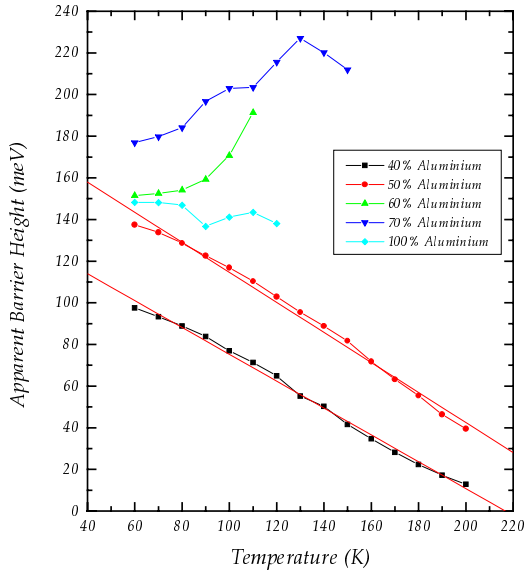

Figure 6.8: Apparent Barrier Height as a function of Temperature from the Fowler-Nordheim Analysis of the 5 bulk barrier n-i-n samples.

for electrons and the conduction band in the barrier. For the samples considered in this study the activation energy for the thermionic emission regime should correspond closely to the conduction band offset between the GaInP and the AlGaInP because the quasi-Fermi level lies within 20 meV of the conduction band edge in the GaInP. As the bias is increased beyond the thermionic emission regime then other transport mechanisms, such as Poole-Frenkel emission and Fowler-Nordheim tunnelling, become significant. This is seen as a reduction in the magnitude of the slope of the TE plot as a function of bias, as seen in Figs. 6.11 and 6.12. The activation energies obtained from the TE plots are plotted as a function of voltage to show how the apparent barrier height varies with applied bias. At low bias the saturation of the activation energy, or apparent barrier height, indicates that thermionic emission is the dominant transport mechanism and the saturated energy value should correspond closely to the actual conduction band offset in the diode. The portions of this plot that are monotonically decreasing are indicative of other transport mechanisms.

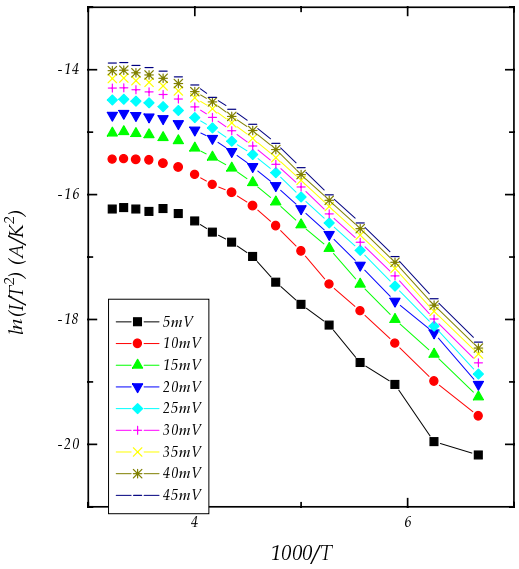

Figure 6.9: Thermionic emission plot for bias points up to 45 mV.

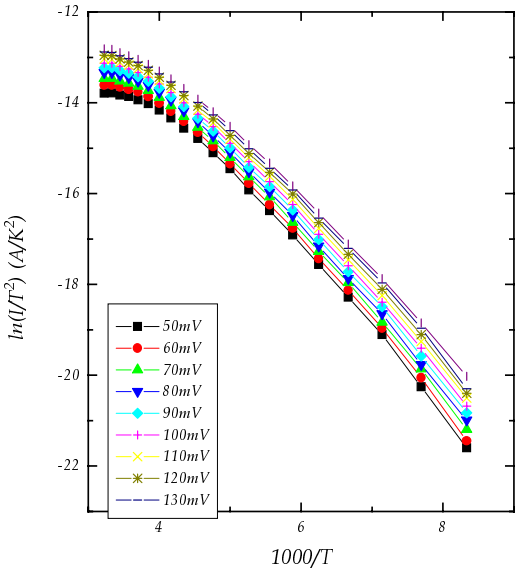

Figure 6.10: Thermionic emission plot for bias points between 50 mV and 140 mV.

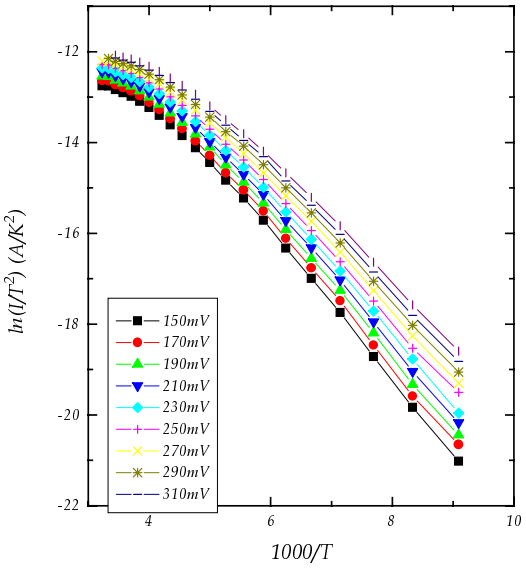

Figure 6.11: Thermionic emission plot for bias points between 150 mV and 330 mV.

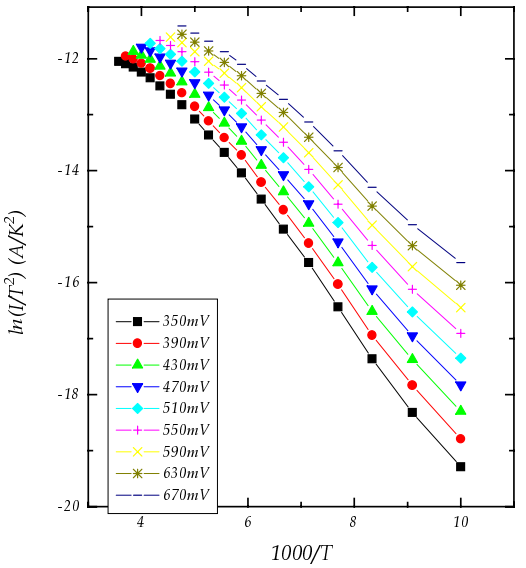

Figure 6.12: Thermionic emission plot for bias points between 350 mV and 710 mV.

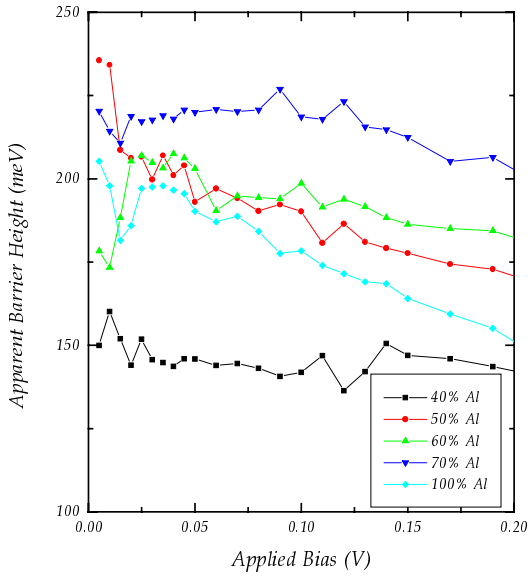

Figure 6.13: Apparent barrier height versus applied bias for bulk n-i-n diodes of various aluminium composition for the forward bias case.

The apparent barrier height versus voltage plot under forward bias conditions for each of the bulk samples examined in this study is shown in Fig. 6.13 and in reverse bias in Fig. 6.14. In the forward bias case, for the 40% sample, the plot saturates towards a zero bias value of between 155 and 165 meV. This is a significant result since the expected conduction band offset in this material is 170 meV. The 50% aluminium barrier is seen to saturate between 210 and 220 meV whereas the theoretically expected barrier height for this composition is 213.5 meV. The 60% aluminium sample is expected to have an indirect barrier and so its X-like character should dominate the barrier properties. It reaches a maximum barrier height of about 210 meV, which is significantly less than its expected , barrier height of 256.2 meV. However, it is much closer in energy to the expected X barrier height of 220.4 meV indicating that the measured activation energy is from the quasi-Fermi level in the GaInP to the X-minima in the AlGaInP barrier. The 70% aluminium barrier has an expected , barrier of 298.9 meV but the barrier is seen to saturate at 220 meV on the graph. This is close to the expected X barrier energy of 210.6 meV again indicating the X like character of the barrier and demonstrating that within the thermionic emission regime the X barrier is the dominant one for indirect bandgap material. In the case of 100% aluminium in the barrier it is observed that at low bias the barrier height reaches a minimum of $\sim$180 meV before rising again to $\sim$205 meV again indicating the X like nature of the barrier which has an expected barrier height of 181.2 meV whereas the , barrier is expected to be 427 meV. These results are summarised in Table 6.1 and compared graphically to the theoretically

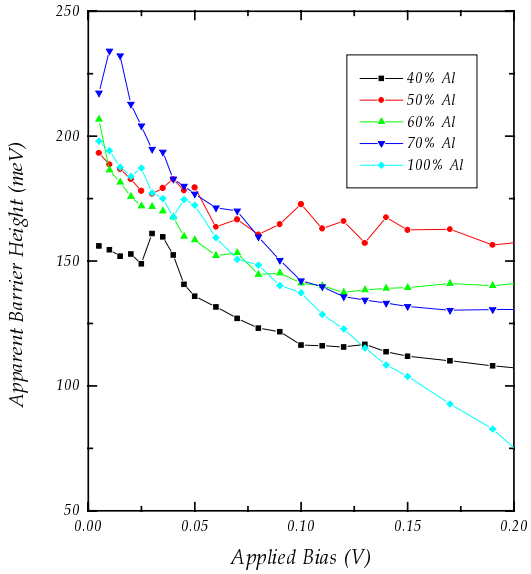

Figure 6.14: Apparent barrier height versus applied bias for bulk n-i-n diodes of various aluminium composition for the reverse bias case.

expected values in Fig. 6.15. The measured barrier heights are obtained by averaging the barrier heights obtained at biases less than 25 mV, except in the cases where the barrier height is monotonically increasing as the bias is reduced, then the measured barrier height is taken to be the maximum value.

% Al	, *– Barrier* (meV)	*X – Barrier* (meV)	*Measured Barrier* (meV)	*Barrier Type*
40	170.8	240	160±10	,
50	213.5	230.2	215±12	,
60	256.2	220.4	210±10	*X*
70	298.9	210.6	220±5	*X*
100	427	181.2	193±13	*X*

Table 6.1: Comparison between expected barrier heights and measured barrier heights for various aluminium compositions in the forward bias case. The measured barrier heights are averages of the barrier heights obtained at biases less than 25 mV.

These are significant results because they demonstrate that for aluminium compositions greater than the crossover composition of AlGaInP the thermionic emission is dominated by the transfer of electrons to the *X* barriers. This is an important consideration for

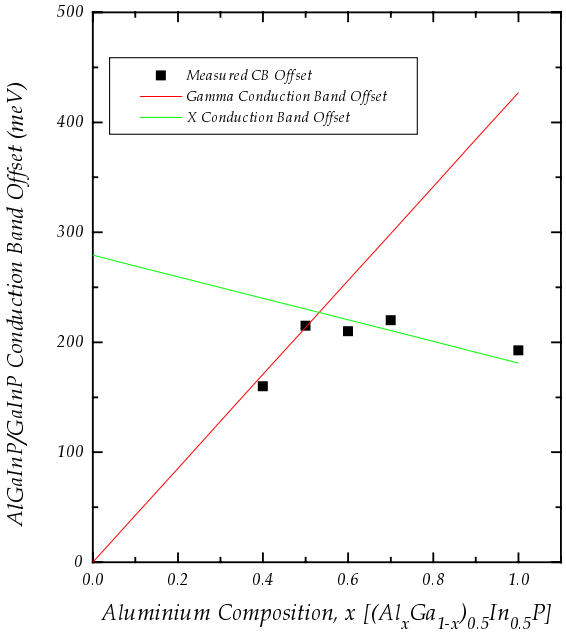

Figure 6.15: Conduction Band Offsets determined experimentally compared with the empirically expected values.

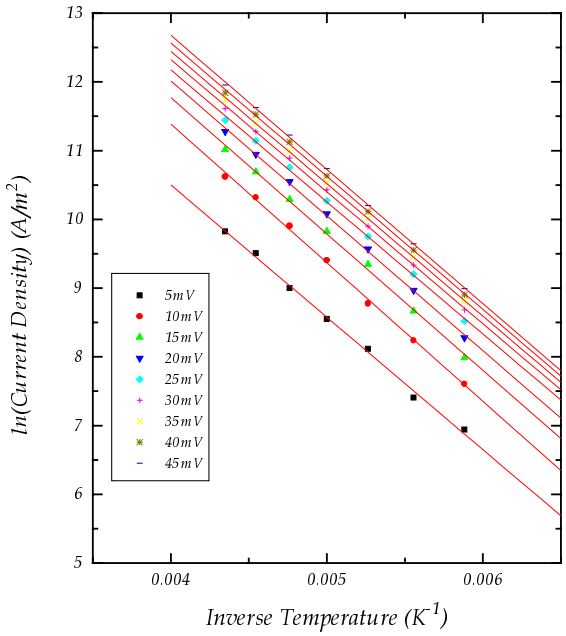

Figure 6.16: Natural log of the current density as a function of inverse temperature for biases up to 45 mV. Red lines are linear fits to the experimental data.

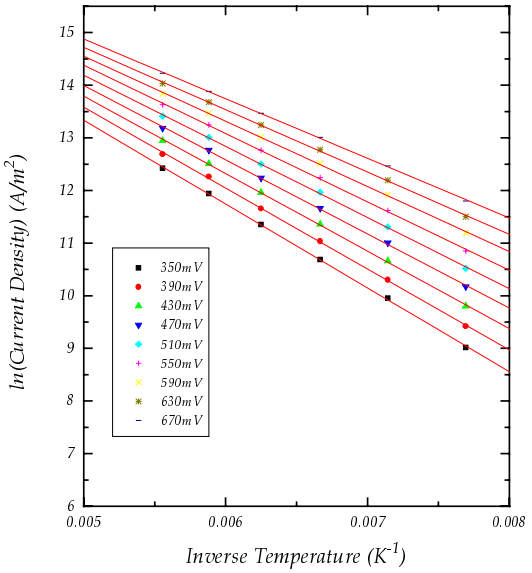

Figure 6.17: Natural log of the current density as a function of inverse temperature for biases between 350 mV and 670 mV. Red lines are linear fits to the experimental data.

designing laser diodes in this material since it implies that as much benefit can be obtained with 50% aluminium in the barriers as with barriers having more than 70% aluminium. These results are also important because they illustrate that this technique allows a very accurate measurement of the barrier heights in the material and they confirm that in disordered AlGaInP the crossover occurs between 50 and 60% aluminium.

From Fig. 6.14, at lower bias the barrier heights tend to saturate to values similar to those observed in the forward bias case. The barrier height is dominated by the direct barrier for the 40% and 50% aluminium cases and by the indirect barrier for the cases of 60%, 70% and 100% aluminium compositions. The measured barrier heights are compared with the theoretically expected values in Table 6.2.

6.4.4 Poole-Frenkel Analysis

According to the model for Poole-Frenkel emission presented in Section 6.2.3 the apparent barrier height for the n-i-n diodes can also be extrapolated from the slopes of the linear portions of a plot of $ln(J)$ versus $1/T$, where J is the current density and T is the absolute temperature. Examples of data from the n-i-n diode with 40% aluminium presented in this manner are shown in Figs. 6.16 and 6.17 respectively. These plots also show the regression lines used to fit the data. The apparent barrier heights are extrapolated from the linear fits to the data for each of the five samples considered and these

% Al	, − Barrier (meV)	X − Barrier (meV)	Measured Barrier (meV)	Barrier Type
40	170.8	240	160±5	,
50	213.5	230.2	195	,
60	256.2	220.4	210	X
70	298.9	210.6	228±7	X
100	427	181.2	200	X

Table 6.2: Comparison between expected barrier heights and measured barrier heights for various aluminium compositions in the reverse bias case

are then plotted as a function of $\sqrt{F}$ where F is the applied field. This data is shown in Fig. 6.18. At low values of applied field ($< 1000\ V^{1/2}m^{-1/2}$ the apparent barrier height saturates to similar values obtained using the Thermionic-Emission model and thus provides a useful means of determining the actual barrier height or conduction band offset between GaInP and AlGaInP. The linear variation in apparent barrier height with $\sqrt{F}$ is indicative of the Poole-Frenkel emission process. Poole-Frenkel emission is seen to be dominant at applied fields in excess of approximately 3 MV/m for all compositions. The linear portions of the graph in Fig. 6.18 run parallel for all compositions at values of $\sqrt{F}$ in excess of 1800 $V^{1/2}m^{-1/2}$. However, the slope of these linear portions of the graph differs from the $2.19 \times 10^{-4}V^{1/2}cm^{1/2}$ required for a purely Coulombic binding potential. The measured slope is approximately $4.8 \times 10^{-3}V^{1/2}cm^{1/2}$ for these samples. It is impossible to attribute these results to any one trap for all the cases considered, however the defect ionisation energy under zero bias, E_{i0}, is found to be 241.21±12.4 meV irrespective of the aluminium composition.

6.5 n-i-n Diodes with MQB Intrinsic Regions

6.5.1 Description of Sample Set

Ten n-i-n diodes were grown and fabricated with MQB barrier layers. The MQB intrinsic barriers were made from $(Al_{0.4}Ga_{0.6})_{0.5}In_{0.5}P$ and the samples were labelled according to the width of the wells and barriers in the MQB, for example sample 14A has a MQB structure {180 Å;5×(14,14) Å} and sample 32A has a structure {180 Å;5×(32,32) Å}. These MQBs are a subset of the samples simulated in Section 4.4.2 where the effect of systematic layer thickness fluctuation in the superlattice of the MQB is examined. That analysis showed that MQBs having the structure of 14A, 16A or 18A should be ineffective as electron reflectors while 20A and subsequent barriers in the series should provide a measured barrier height that is in excess of the

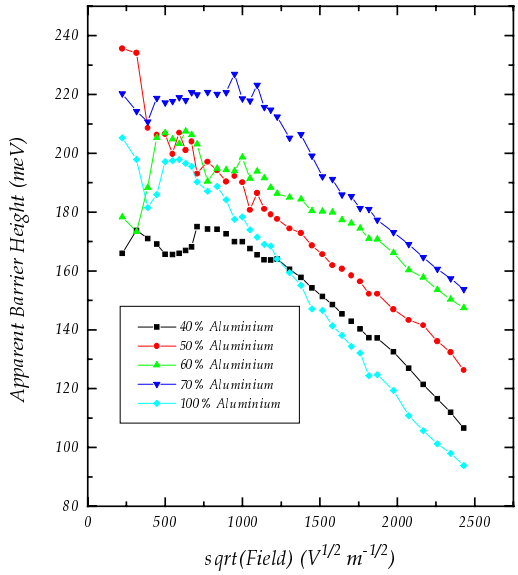

Figure 6.18: Poole-Frenkel plot for the n-i-n samples of various aluminium composition in the barrier.

bulk barrier height. 20A should be the best reflector with a barrier height increase of over 100 meV, while 32A should give a barrier height improvement of over 30 meV. The purpose of this experiment is to see if the barrier height measured experimentally matches the theoretically predicted barrier heights for the MQBs and to compare the MQB with a bulk barrier of the same aluminium content and dimensions. There are no results available from 18A and this sample has been eliminated from the remaining analysis.

6.5.2 MQB Barrier Height Evaluation

In the previous section it was shown that good approximations to the barrier height of bulk AlGaInP barriers could be measured from a plot of $ln(I/T^2)$ versus $1000/T$ at low bias. The measured barrier height corresponded to the difference in energy between the quasi-Fermi level for electrons and the lowest lying conduction band in the barrier. AlGaInP with 40% aluminium was chosen as the ideal barrier material from which to make MQB diodes since the influence of the X band on the direct barrier height was seen to be negligible at this composition. The technique for measuring barrier heights as described in the previous section was applied to n-i-n diodes with multiquantum barriers this time to see if any barrier height increase could be measured.

As described in the previous section for the bulk devices the thermionic emission model was applied to each of the MQB samples in turn to establish the actual barrier

height at low bias. The bias point chosen was 10 mV. Fig. 6.19 shows the measured barrier height for each of the MQB samples and compares them with the simulated values from Section 4.3.2. It is obvious that none of the MQB structures displays an increased virtual barrier due to the MQB effect. In fact the measured barrier heights for these samples fall short of even the expected bulk barrier height. In addition the barrier height measured in reverse bias for these structures is slightly greater, but not significantly so in all cases except the 14A case. The conclusion of this analysis can only be that either it is impossible to measure any barrier height increase with this analysis technique, because of the applied bias on the MQB, or the MQB is simply ineffective as an electron reflector. This is the first time that the MQB has been studied in such a systematic way and the fact that it fails to show any improvement over the bulk barrier height is discouraging for the MQB theory. In the next chapter two of the MQB structures are included in the p-cladding layer of a bulk double heterostructure AlGaInP laser to see if they have any effect on the performance of these lasers.

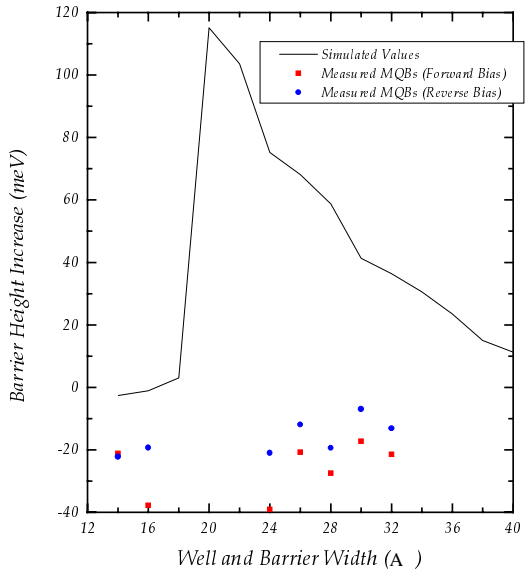

Figure 6.19: Comparison between measured barrier heights for the various MQB samples and the expected values from the simulations of Section 4.3.2.

6.6 Summary and Conclusions

In this chapter various models of carrier transport over and through an insulating barrier were introduced. Thermionic emission was chosen as the most appropriate model for measuring the apparent barrier height in both bulk and MQB barriers in n-i-n diodes. This model was chosen because thermionic emission was seen to be the

dominant transport mechanism at very low electric fields. The ability to measure the apparent barrier height at low electric fields is important for comparing the bulk and MQB barriers in the n-i-n diodes since distortion of the MQB by high electric fields render it useless as an electron reflector making it impossible to measure any virtual barrier produced by the MQB.

Bulk barriers of different barrier heights were obtained by varying the aluminium composition of the AlGaInP barrier. The apparent barrier height as measured from a plot of $ln(I/T^2)$ versus $1/T$ was found to correspond to the lowest lying conduction band in the barrier. This was found to be the , conduction band minimum in the case of aluminium compositions of 40 and 50%. For the other aluminium compositions investigated the barrier height measured was found to correspond quite closely to that expected for the X conduction band minima in the barrier. From these measurements it was concluded that this technique could be used to measure the barrier height of a n-i-n diode with bulk barriers. The analysis clearly showed that increasing the aluminium content above 50% in the AlGaInP barriers does not significantly increase the barrier height.

The apparent barrier height was then measured in n-i-n diodes with MQB intrinsic regions. No increase in barrier height due to the MQB effect was observed. The difference in barrier height between nine different MQB samples was only 20-30 meV. When these MQB barriers were compared with a bulk barrier of similar thickness it was found that the difference between the bulk barrier and the MQB was less than 20 meV.

Chapter 7

MQB Performance in Bulk DH Laser Diodes

7.1 Introduction

The MQB effect of an increased barrier height was not observed when isolated MQB structures were investigated as described in Chapters 5 and 6. For laser diodes with MQBs included in the p-cladding region there have been several reports in the literature of vastly improved laser diode performance [1, 6, 2, 11, 12, 14, 15] and this improved performance is normally attributed to the MQB producing a virtual barrier that is in excess of the bulk barrier height. In all of these cases the measured barrier height improvement is found to be much lower than the theoretically predicted value. However, since relatively minor structural changes in lasers can lead to significant changes in performance, it is difficult to unambiguously establish whether MQBs improve laser characteristics because of an increase in barrier height or whether some other subtle explanation is appropriate. It is possible, for example, that changes in the optical confinement of the active region due to the MQB may be responsible for the enhanced performance rather than an increase in the barrier height. To critically assess the effects of MQBs three laser structures were grown and fabricated. A bulk double heterostructure (DH) reference laser; a laser with a MQB optimised to achieve an increased virtual barrier height and another with a MQB deliberately designed to have a transmission window 100 meV wide above the bulk barrier height. These laser structures are not optimised for high temperature operation, but are specially designed to critically compare MQB and conventional laser performance. The MQBs are included in the cladding region on the p-side of the laser with the superlattice regions facing the incoming electrons. The MQB structures are kept undoped and the active regions of the lasers are adjusted to ensure the same optical confinement in all three lasers. From a relative comparison of threshold current and characteristic temperature

values (T_0) in the reference laser and the MQB lasers it has been shown that the MQB does indeed improve the performance of visible laser diodes, but that the improvement cannot be uniquely attributed to a virtual increase of the barrier in the conduction band.

7.2 Experimental Details

To reduce the complexity of assessing the effect of MQBs on visible laser performance a simple InGaP/AlGaInP DH laser was used as the reference laser. The $(Al_{0.4}Ga_{0.6})_{0.5}In_{0.5}P$ cladding material used in these lasers ensures that the conduction band offset with the $Ga_{0.5}In_{0.5}P$ active region is sufficiently small that carrier loss over the barrier is a significant leakage mechanism and that any improvement due to the MQB should be seen as a dramatic effect. In addition, by using this direct bandgap composition of AlGaInP barrier material, the influence of the X conduction band minima on the electron transport over the InGaP/AlGaInP heterojunction barrier is reduced.

The thickness of the reference laser's active region is 500 Å with cladding regions of 1.1 μm on either side. Waveguide calculations [83] predict an optical confinement factor of 20% for this design. The optical confinement factor for the subsequent MQB lasers is kept the same as that of the reference sample by modifying the thickness of the active region. Schematic pictures of all three laser designs are shown in Fig. 7.1.

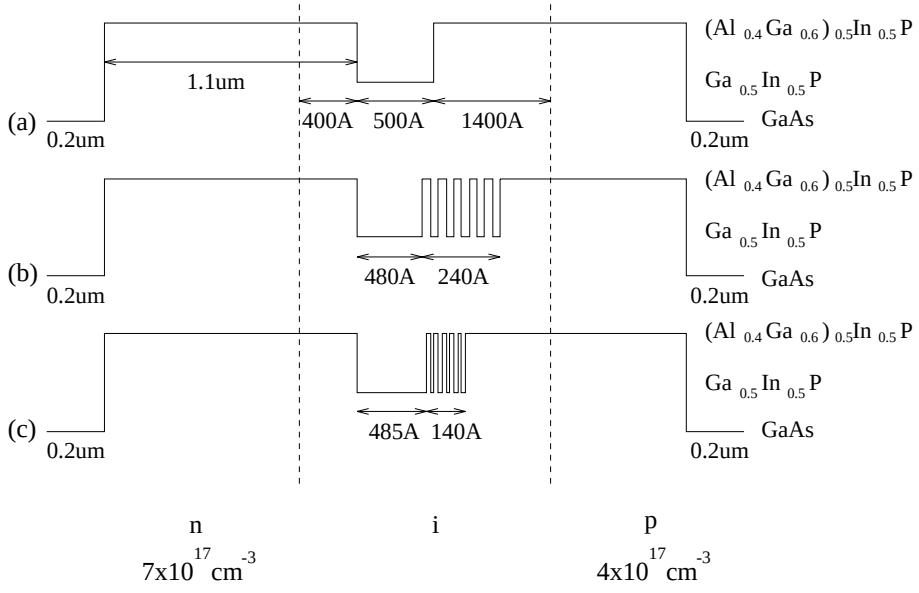

Figure 7.1: Schematic representation of the three laser structures, (a) Bulk reference, (b) Optimised MQB and (c) Leaky MQB.

For a MQB to provide a virtual barrier it is essential that the electron wavefunction should remain coherent throughout the superlattice region of the MQB. This requirement becomes increasingly more difficult to meet in thicker structures. It has been shown from photoconductivity measurements of a GaAs/AlGaAs superlattice that an electron in the superlattice miniband can have a room temperature coherence length of up to 495 Å. [54] Using this value as an upper limit of the electron coherence length in $(Al_xGa_{1-x})_{0.5}In_{0.5}P$ implies that for a MQB to have any likelihood of working effectively at room temperature it needs to be significantly less than 500 Å thick, while still maintaining a high reflection coefficient. Typically a MQB is placed in the cladding region of the laser with the anti-tunnelling layer facing the incoming electrons.[16] In this orientation the electron needs to remain coherent over the entire MQB structure, not just the superlattice. In Chapter 4, calculations showed that the electron reflectivity of the MQB is identical irrespective of whether the electrons encounter the superlattice region or the anti-tunnelling layer first, provided scattering effects are neglected. It is more advantageous however, from the point of view of preserving coherence, to have the superlattice region of the MQB adjacent to the active region. Electrons at energies resonant with the quantised states in the superlattice may tunnel out of the active region but these will be returned by reflection from the bulk cladding region. In this sense the cladding region serves as the anti-tunnelling layer of the MQB. The superlattice is kept undoped to preserve the interface quality and the undoped region is extended into the cladding to reduce back diffusion of dopants into the MQB superlattice.

The optimised design consists of five periods of $(Al_{0.4}Ga_{0.6})_{0.5}In_{0.5}P/Ga_{0.5}In_{0.5}P$ with each well and barrier 24 Å thick. The leaky design of the MQB also consists of 5 periods, but with well/barrier thicknesses of 14 Å. Calculations of electron reflectivity as a function of electron energy for the leaky design show a drop in reflectivity to below 50% at the bulk barrier height of 170.8 meV and has a similar average reflectivity as the bulk up to 270 meV after which the reflectivity increases again to above 90%. The optimised design displays a theoretical cut-off of 245 meV at 99.9% reflectivity. These are calculated using the effective mass model previously presented in Chapter 4. [17] In the calculation, the electron effective mass is taken to be $0.11m_0$ in the well, while the effective mass in the barrier is estimated by linear interpolation between the electron effective mass in $Ga_{0.5}In_{0.5}P$ and that in $Al_{0.5}In_{0.5}P$ to be $0.21m_0$. [68] Plots of the electron reflection from the leaky and optimised MQB structures are shown in Figures 7.2 and 7.3 respectively.

All the laser structures were grown by metalorganic vapour phase epitaxy and fabricated into 7 μm stripe lasers with 500 μm cavity lengths. The diodes were bonded to copper heat sinks and mounted on T05 headers. Diode testing was conducted in a closed cycle Stirling cryostat which allowed the diode temperature to be controlled from 80 K to 300 K with an accuracy of $\pm 0.5K$. This experimental set-up is the same as

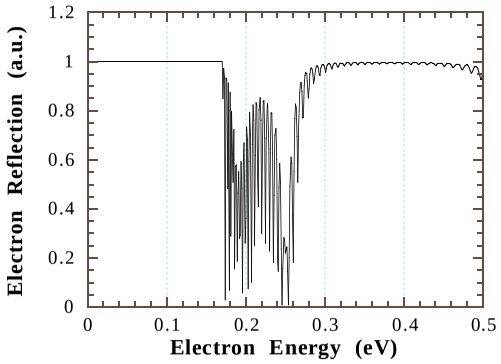

Figure 7.2: Electron reflection as a function of electron energy for the leaky MQB structure.

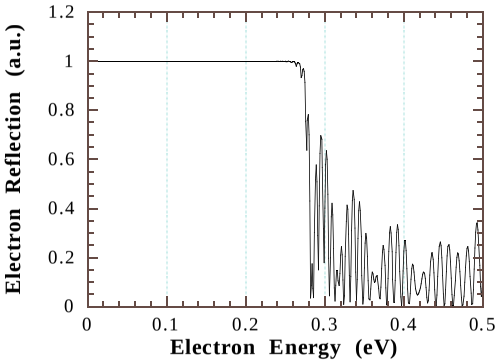

Figure 7.3: Electron reflection as a function of electron energy for the optimised MQB structure.

that used for the n-i-n diodes and is described in Chapter 6. The threshold current as a function of temperature was measured under pulsed and continuous wave conditions for each of the three laser diodes. The pulse width was 200 ns and the repetition rate was 1 kHz. Wavelength measurements at room temperature indicate that all three lasers emit at 662 nm.

7.3 Results

7.3.1 Threshold Current as a function of Temperature

The variation in threshold current as a function of temperature for each of the three laser types is shown in Fig. 7.4. From this figure, at temperatures below 170 K all three lasers

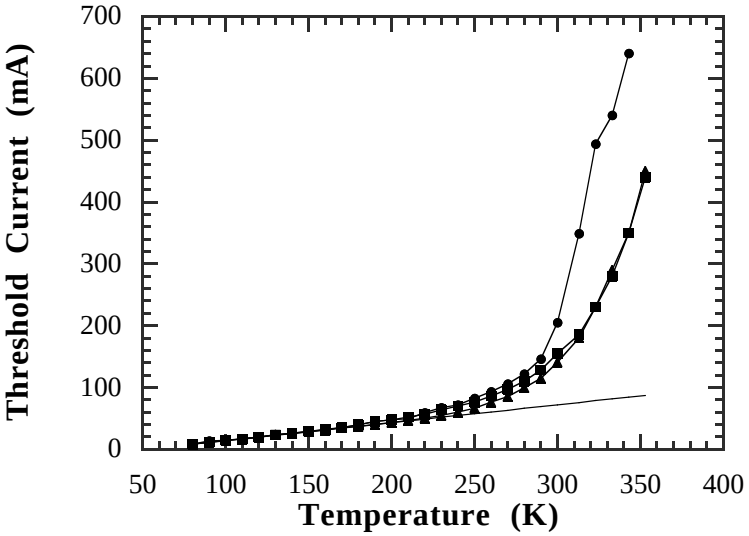

Figure 7.4: Temperature variation of the threshold current for the reference laser (circle), the optimised MQB laser (triangle) and the leaky MQB laser (square). Straight line is a linear extrapolation of low temperature data.

behave identically, since the carrier leakage over the barrier at these temperatures is not significant. This also demonstrates that the optical confinement in the three structures is the same, as designed. However, as the temperature is raised the threshold current in the bulk reference and the leaky MQB begins to rise faster than that of the laser with the optimised MQB design. The bulk reference laser and the leaky MQB laser approximately follow each other up to a temperature of 240 K after which the threshold current of the bulk reference begins to rise at a higher rate than the leaky MQB laser. At room temperature the bulk reference laser has the highest threshold current of 205 mA while the leaky MQB laser requires 156 mA. The optimised MQB laser shows the best performance with a threshold current of 141 mA which represents a 31% reduction in threshold current over the reference laser at room temperature. Above room temperature the leaky MQB laser approaches the performance of the optimised MQB laser and at 313 K they appear identical. At this temperature the bulk laser has a threshold current that is more than twice that of the MQB lasers. As the temperature is increased further the percentage difference in threshold current between the bulk and MQB lasers reduces and at a temperature of 343 K the bulk reference has a threshold current that is approximately 45% larger than either of the two MQB lasers.

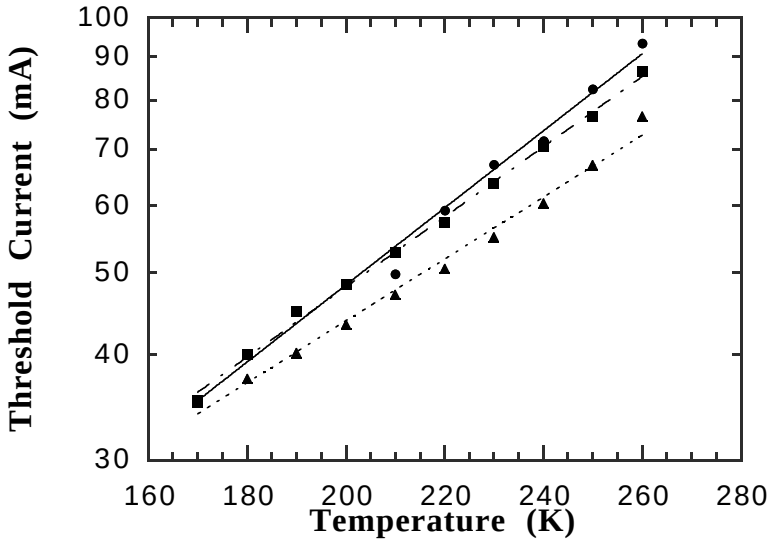

Figure 7.5: Low temperature threshold current data to calculate T_0 for the reference laser (circle), the optimised MQB laser (triangle) and the leaky MQB laser (square). Straight lines represent least squares fits to the data.

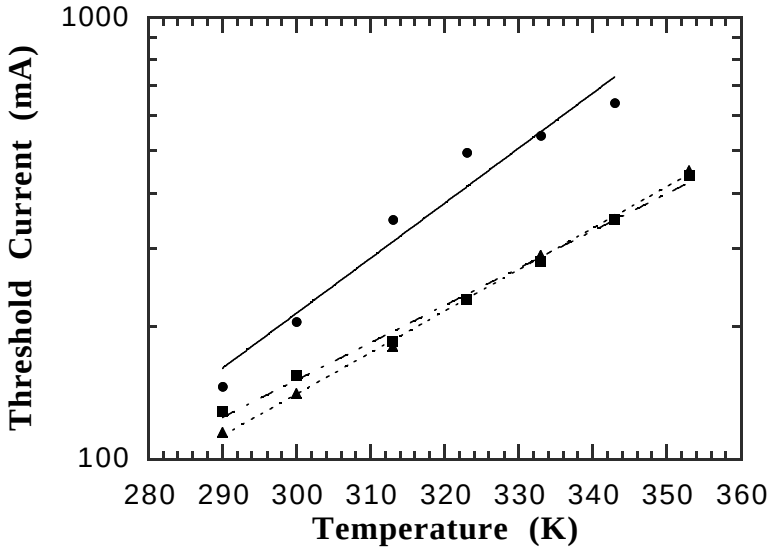

Figure 7.6: High temperature threshold current data to calculate T_0 for the reference laser (circle), the optimised MQB laser (triangle) and the leaky MQB laser (square). Straight lines represent least squares fits to the data.

7.3.2 T_0 Characteristics

As mentioned in Chapter 2, double heterostructure lasers typically display two characteristic temperatures, identified by two distinct slopes on a plot of $ln(J_{th})$ versus $Temperature$. The T_0 of the reference laser, leaky MQB laser and optimised MQB laser, determined from a plot of $ln(J_{th})$ versus $Temperature$ between 170 and 260 K, are 95, 105 and 119 K respectively. This is shown in Fig. 7.5. There is a 20 K improvement in the T_0 parameter for the optimum MQB laser over that of the reference laser. From Fig. 7.6, the T_0 of the reference laser, leaky MQB laser and optimised MQB laser between 290 and 343 K, are 35, 53.5 and 47 K respectively. At these elevated temperatures the T_0 drops significantly due to increased thermal loss of carriers over the heterobarrier. The T_0 for the leaky MQB is greater than that of the optimised MQB at these temperatures and both of these lasers have a T_0 that is at least 12 K larger than the bulk reference laser. These results indicate that the MQB lasers are less sensitive to temperature than the bulk reference laser.

7.3.3 Determination of Activation Energies from Excess Current

Defining excess current as the difference between the threshold current of each laser structure and the straight line shown in Fig. 7.4 the approach of Hagen *et al* [84] is adopted and this excess current as a function of inverse temperature is plotted in Fig. 7.7. From this plot, two activation energies are apparent for the bulk and leaky MQB lasers, whereas the optimised MQB laser displays only one activation energy over the entire temperature range between 220 and 350 K. The low temperature excess current between 220 K and 270 K is shown in Fig. 7.8 and indicates that over this range the bulk and leaky MQB lasers have almost identical activation energies of 143.9 meV and 140.7 meV respectively. The optimised MQB laser has an activation energy of 273.9 meV over the same temperature range, this is approximately 130 meV larger than either of the other two lasers and explains why the optimised MQB laser has a lower threshold current then either of the other two lasers over this temperature range.

The excess current as a function of temperature between 280 and 350 K is shown in Fig. 7.9. Over this temperature range the optimised MQB has an activation energy of 282 meV, slightly larger than before. The leaky MQB laser has an activation energy that is increased to 240.4 meV. The bulk reference laser has a non-linear excess current over this temperature range. It is possible to fit several different activation energies to this data depending on the temperature range considered. For the temperature range 280-350 K a least squares fit to the bulk laser excess current gives the largest activation energy of the three with 326 meV. With an activation energy this large the bulk reference laser would be expected to outperform the MQB lasers. It is difficult to attribute these measured activation energies to any one leakage mechanism in the

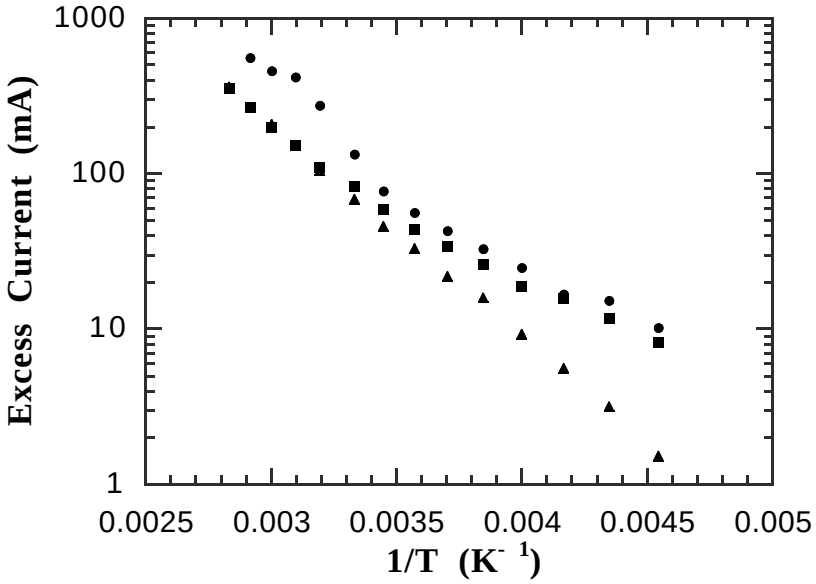

Figure 7.7: Excess current as a function of inverse temperature for the reference laser (circle), the optimised MQB laser (triangle) and the leaky MQB laser (square).

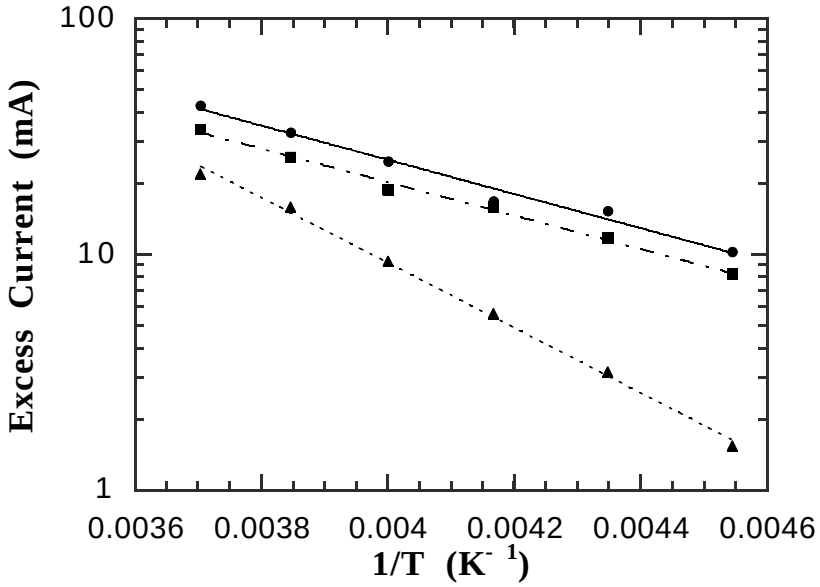

Figure 7.8: Low temperature excess current as a function of inverse temperature for the reference laser (circle), the optimised MQB laser (triangle) and the leaky MQB laser (square). Straight lines represent least squares fits to the data.

lasers. It is best to consider the activation energies as containing contributions from several leakage mechanisms. In this way the large activation energy in the bulk laser between 280 and 350 K can be attributed to the presence of additional leakage paths that have been eliminated in the MQB lasers, such as a transfer of electrons into the X-minima of the conduction band in the barrier.

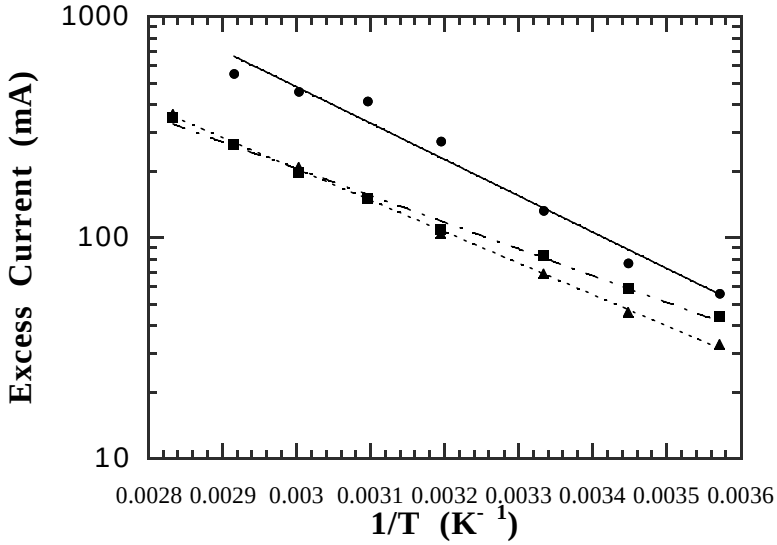

Figure 7.9: High temperature excess current as a function of inverse temperature for the reference laser (circle), the optimised MQB laser (triangle) and the leaky MQB laser (square). Straight lines represent least squares fits to the data.

7.4 Discussion and Conclusions

Calculation of electron reflectivity from MQB structures can be quite sensitive to the layer thickness and effective mass parameters. For the leaky MQB laser a layer thickness fluctuation of -4 Å will widen the transmission window to over 200 meV while a fluctuation of +4 Å can produce a barrier as good as the optimised MQB structure. Similar fluctuations in the layer thicknesses of the optimised MQB always yield a virtual barrier of at least 50 meV in excess of the bulk barrier height. The effective mass in the barrier material is the least certain parameter in the design and any reduction or increase in this effective mass will reduce or increase the barrier height respectively. The experimental uncertainty in both thickness and effective mass parameters therefore allows for the possibility that the reflectivity of the leaky MQB can be greater than intended. However, since the measured activation energy for the leaky MQB is far less than that of the optimised MQB, it is expected that both MQBs are performing as

designed.

The threshold current for both MQB lasers is significantly less than that of the bulk laser. This is surprising since one of the MQB lasers was designed to be ineffective according to the conventional theory of MQB operation. The fact that similar improvements in laser diode characteristics are obtained irrespective of the MQB design is evidence that the improvement in performance cannot be uniquely attributed to the MQB effect alone and suggests that another mechanism in addition to the conventional MQB effect is responsible. It is plausible, for example, that the MQB structures serve to inhibit non-radiative recombination routes via $X-$states in the barrier, a loss mechanism that has recently been highlighted by Smowton and Blood.[4] Alternatively, Yen *et al* [49] suggest the proximity of the $X-$minima to the , minimum in many MQB laser designs could also yield an improvement in laser performance by virtue of the increased effective mass. The measured activation energies cannot be attributed to any single leakage path in the lasers. It is quite likely that the measured activation energies contain contributions from several leakage paths within the laser. This is something that needs to be investigated further, possibly by measuring the spontaneous emission from the laser structures as a function of temperature. This should give a greater insight into the recombination routes for each of the three lasers studied here.

In conclusion, the results presented here confirm that the use of a MQB in the cladding region of a bulk double heterostructure laser improves the threshold characteristics at room temperature. The complete mechanism responsible for the improvement is not, as yet, fully understood, but it was shown that the improvement is not due to the MQB providing a virtual increase in the cladding barrier height by reflection of high energy electrons. Finally, an improvement in laser operation was still achieved irrespective of the MQB orientation in the cladding.

Chapter 8

Conclusions and Future Work

8.1 Introduction

This chapter summarises the work performed in this thesis. The main conclusions of the thesis are outlined and areas of future work are presented.

8.2 Thesis Summary

Visible laser diodes were introduced in this thesis as important optical sources for many applications. High density optical storage was highlighted as a major commercial application of AlGaInP based laser diodes. Double heterostructure (DH) laser diodes were described and several of the leakage mechanisms evident in AlGaInP DH laser diodes were presented. Attention was focused on electron leakage over the heterobarrier with a description of the techniques used by several researchers to suppress electron overflow in AlGaInP lasers. The multiquantum barrier (MQB) concept for reducing electron overflow from the active region to the p-cladding region of a laser diode was introduced as an effective means of improving the characteristics of visible laser diodes. The operating principle of the MQB, i.e. the production of an increased virtual barrier by enhanced reflection of high energy electrons, was shown to be questionable when attempts to verify the MQB effect by several researchers proved inconclusive. In this thesis the problem of verifying the MQB theory has been addressed by initially developing a qualitative understanding of how the MQB works. The effective mass model used by Iga *et al* to calculate the reflection from a MQB was extended to include the effects of , $-X$ mixing and electron scattering within the AlGaInP semiconductor alloy. Using these models the idealised performance of the MQB was investigated and MQB structures were designed for use in visible laser diodes and n-i-n diodes to experimentally verify the operating principle of the MQB.

The photoluminescence (PL) intensity as a function of temperature from quantum

well samples surrounded by MQBs and bulk barriers was experimentally measured. These were normalised and plotted on an Arrhenius plot to measure the thermal activation energies for electrons escaping out of the quantum well in both cases. There was no measured barrier height increase due to the MQB effect, although the samples with MQBs displayed a higher radiative efficiency near room temperature. Additional measurements of the barrier height for n-i-n diodes with MQB and bulk barrier regions showed no evidence of an enhanced electron reflection due to the MQB effect. This is the first time such measurements have been performed for AlGaInP n-i-n diodes. The high fields across the MQB intrinsic region of the n-i-n diodes make the operation of the MQB as an electron reflector impossible. The introduction of MQB structures into visible laser diodes is shown to reduce the threshold current by a factor of two at 313 K, as well as increase its characteristic temperature by 20 K. These structures provide the most convincing evidence to date that the improvement due to the presence of MQBs in visible laser diodes cannot simply be attributed to an increased virtual barrier height due to quantum mechanical reflection of high energy electrons.

8.3 Conclusions

8.3.1 Principal Results and Conclusions

The fact that MQB structures improve the performance of visible laser diodes is indisputable. This has often been demonstrated in the literature and has been confirmed again by the laser results presented in this work. What is questionable though is the reason for the improved performance. The MQB concept, as originally proposed by Iga, explains the operation of the MQB by drawing an analogy with an optical Bragg reflector. The MQB is supposed to produce a virtual increase in the barrier height of the intrinsic barrier by enhanced reflection of high energy electrons. In this thesis Iga's idealised theory of MQB operation is shown to be insufficient to describe the MQB in a real device. Iga's explanation of MQB operation only holds for a theoretically ideal device. For a MQB structure to work there are several conditions that must be met, many of which are currently impossible to achieve in a real device. These include the assumption of an infinite coherence length for the electron; a flat band condition across the structure and completely undoped MQBs. The presence of scattering mechanisms, the nature of epitaxial growth and the large biases applied to the laser diodes ensure that the necessary conditions for the MQB to work as an electron reflector cannot be met. To increase the possibility of the MQB working as an electron reflector suggestions have been made to enable the optimisation of the MQB for real device operation. These suggestions included reversing the MQB orientation to minimise the length over which the electron wavefunction needs to remain coherent; keeping the entire MQB

structure undoped, and extending the undoped region into the p-cladding of the laser to prevent back diffusion of the Zn dopant which would result in a distortion of the interface quality in the MQB superlattice. It was also suggested that the AlGaInP barrier material should contain only a 40:60 Al to Ga ratio because this minimises any effects due to the proximity of the X-minima which occurs in higher aluminium compositions. In addition the low aluminium content in the barriers ensures that electron leakage over the heterobarrier between the GaInP and AlGaInP is a significant leakage mechanism.

Although every consideration was given to allow the MQB to perform as an electron reflector the experimental evidence shows that there is no measurable barrier height increase due to the MQB effect. Iga's explanation of the MQB effect is shown not to hold for MQBs in real devices. The most convincing piece of evidence from this work that confirm this fact is the similar improvements in laser diode characteristics irrespective of whether the MQB included in the laser is designed to be an effective electron reflector or not. The ultimate conclusion from this work must be that the operation of the MQB in the p-cladding of a laser diode is a generic effect irrespective of the MQB design. Two possible explanations for the improvement due to the MQB are the ability that interfaces have for preventing the diffusion of dopant atoms which in turn could prevent the Zn-dopants in the p-cladding from diffusing into the active region of the laser; another explanation which is related to the first is the possibility that diffused Zn is captured between the interfaces of the MQB thereby increasing the level of p-type doping locally. This increase in p-type doping has the effect of moving the Fermi level in the p-cladding closer to the valence band edge which in turn increases the barrier to electrons in the conduction band of the p-cladding region. [85]

8.3.2 Additional Results and Conclusions

There are several other significant results arising from this thesis that are general to AlGaInP and visible laser diodes without being specific to MQBs. All of these results, however, come from the analysis techniques applied to this investigation of the MQB. These supplementary results and conclusions are presented here. For the first time the I-V characteristics of AlGaInP n-i-n diodes as a function of temperature for MQB and bulk intrinsic barriers are measured and analysed. The thermionic emission model was shown to be useful for estimating the barrier height in these devices. Measurements of the barrier height for devices with barriers using different aluminium compositions show that the intrinsic barrier in the conduction band is the , minimum for aluminium compositions $\leq 50\%$ and the X-minima for aluminium compositions $\geq 60\%$. This result confirms the direct-indirect crossover for AlGaInP to be between 50% and 60% as predicted by empirical measurements by other researchers. It was concluded from

Previous Work	*This Thesis*
MQBs work according to simple effective mass model.	Improved simple effective mass model by including , $-X$ mixing and scattering effects. MQB may only work in reversed orientation.
PL intensity measurements show increased luminescence with MQBs. Conclude that MQB effect is real.	PL intensity measurements with resonant excitation show that MQB effect not necessary to explain increased luminescence with MQBs.
I-V characteristics of n-i-n diodes at 77 K. Higher turn-on voltage for MQB intrinsic regions. Conclude that MQB effect is real.	I-V characteristics of n-i-n diodes between 60 K and 300 K. Thorough analysis of transport mechanisms in AlGaInP. Quantitative barrier height measurements indicate MQBs don't increase the barrier height. No flat band condition across MQB precludes it from working as a reflector.
Include MQBs in lasers. Improved characteristics leads to the conclusion that MQB effect is real.	Compare MQB designed to produce a virtual barrier with one designed to be ineffective as a reflector. Both show improved characteristics when included in lasers. Can conclude that the MQB effect cannot be uniquely attributed with the improvement.

Table 8.1: Summary of the advances in the understanding of operation of MQBs from this thesis.

these measurements that there is no advantage to be gained in having a cladding region in a visible laser diode with an aluminium composition greater than 50%. In fact the reduced aluminium content in the cladding of the laser means an increase in hole mobility and makes the p-cladding easier to dope to a high level, thus introducing greater benefits than higher aluminium compositions in the cladding. The difficulty in attributing the measured activation energies, from PL measurements from quantum wells and excess current measurements in bulk DH laser diodes, to any one leakage mechanism leads to the conclusion that there are several possible leakage routes that are equally, if not more, significant than electron leakage over the GaInP/AlGaInP heterobarrier in AlGaInP laser diodes. The main results of this thesis are summarised in Table 8.1.

8.4 Suggested Areas of Future Work

The work presented in this thesis has demonstrated the complexity of AlGaInP and device structures fabricated from it. It has been conclusively demonstrated that the

improvements in laser diode characteristics with MQBs cannot be uniquely attributed to the MQB effect. The role of the MQB in improving laser diodes remains uncertain, although two possible explanations have been put forward in the text. Further investigation is required to verify these explanations or indeed to discover other explanations.

It was pointed out in Chapter 5 that there were two flaws in the PL experiment to measure an increased barrier height due to the MQB. The samples used in the investigation should be changed to include the MQB on only one side of the quantum well and the barrier material should be reduced in aluminium composition to 20%. This would ensure that carrier leakage out of the quantum well is by thermal activation over the barrier. In addition the sample could be grown with two additional quantum wells of different widths each a set distance to the left and right of the main quantum well. The luminescence from these wells would be a measure of the amount of carriers leaking over the bulk barrier and MQB when the main quantum well is resonantly excited.

The analysis of the n-i-n diodes in Chapter 6 provided useful information about the transport regimes in bulk AlGaInP. The analysis could be extended to include multi-quantum barriers. It would be very beneficial if a single model could be developed to describe the device performance over the entire range of temperatures and bias considered. It would also be useful to compare the transport regimes in samples grown by MBE and MOVPE. A comparison between the AlGaAs material system and AlGaInP would be instructive because more information is available about the bandstructure of AlGaAs which increases the confidence in the interpretation of the results.

In hindsight an additional laser sample should have been grown for the comparison in Chapter 7. This laser should have a MQB structure in the normal orientation to act as an additional control sample. One particularly interesting and useful experiment that should be performed is the measurement of the spontaneous emission as a function of temperature from the top surface of the laser diodes described in this thesis. This follows similar work performed by Smowton and Blood [4] to investigate the recombination routes in AlGaInP laser diodes. If this technique is applied to the devices described in this thesis then a more quantifiable measure of the recombination routes affected by the presence of the MQB structures can be made.

Bibliography

[1] J. Rennie, M. Okajima, M. Watanabe, and G. Hatakoshi, "Room temperature CW operation of orange light (625nm) emitting InGaAlP laser," *Elect. Lett.*, vol. 28, pp. 1950–1952, Oct. 1992.

[2] M. Watanabe, J. Rennie, M. Okajima, and G. Hatakoshi, "Improvement in the temperature characteristics of 630nm band InGaAlP multiquantum-well laser diodes using a 15° misoriented substrate," *Elect. Lett.*, vol. 29, pp. 250–252, Feb. 1993.

[3] G. Hatakoshi, K. Itaya, M. Ishikawa, M. Okajima, and Y. Uematsu, "Short-wavelength InGaAlP visible laser diodes," *IEEE J. Quant. Elect.*, vol. 27, pp. 1476–1482, June 1991.

[4] P. M. Smowton and P. Blood, "$GaInP - (Al_yGa_{1-y})InP$ 670nm quantum well lasers for high-temperature operation," *IEEE J. Quant. Elect.*, vol. 31, pp. 2159–2164, Dec. 1995.

[5] H. Tanaka, Y. Kawamura, S. Nojima, K. Wakita, and H. Asahi, "InGaP/InGaAlP double-heterostructure and multiquantum-well laser diodes grown by molecular-beam epitaxy," *J. Appl. Phys.*, vol. 61, pp. 1713–1719, Mar. 1987.

[6] M. Shono, S. Honda, T. Ikegami, Y. Bessyo, R. Hiroyama, H. Kase, K. Yodoshi, T. Yamaguchi, and T. Niina, "High-power operation of 630nm-band tensile strained multiquantum well AlGaInP laser diodes with a multiquantum barrier," *Elect. Lett.*, vol. 29, pp. 1010–1011, May 1993.

[7] P. J. A. Thijs, "Progress in quantum well lasers: Application of strain," *Digest of the 13^{th} IEEE International Semiconductor Laser Conference*, p. 2, 1992.

[8] M. D. Dawson and G. Duggan, "Band-offset determination for GaInP-AlGaInP structures with compressively strained quantum well active layers," *Appl. Phys. Lett.*, vol. 64, pp. 892–894, Feb. 1994.

[9] K. Iga, H. Uenohara, and F. Koyama, "Electron reflectance of multiquantum barrier (MQB)," *Elect. Lett.*, vol. 22, pp. 1008–1010, Sept. 1986.

[10] J. de Poorter, "Private communication.".

[11] T. Fukushima, H. Shimizu, K. Nishikata, Y. Hirayama, and M. Irikawa, "Carrier confinement by multiple quantum barriers in 1.55 μm strained GaInAs/AlGaInAs quantum well lasers," *Appl. Phys. Lett.*, vol. 66, pp. 2025–2027, Apr. 1995.

[12] T. Takagi and K. Iga, "Temperature dependence of GaAs/AlGaAs multiquantum barrier lasers," *IEEE Photonics Technology Lett.*, vol. 4, pp. 1322–1324, Dec. 1992.

[13] A. P. Morrison, J. D. Lambkin, C. J. van der Poel, and A. Valster, "Evaluation of multiquantum barriers in bulk double heterostructure visible laser diodes," *IEEE Photonics Technology Letters*, vol. 8, pp. 849–851, July 1996.

[14] K. Kishino, A. Kikuchi, Y. Kaneko, and I. Nomura, "Enhanced carrier confinement effect by the multiquantum barrier in 660nm GaInP/AlInP visible lasers," *Appl. Phys. Lett.*, vol. 58, pp. 1822–1824, Apr. 1991.

[15] J. Rennie, M. Watanabe, M. Okajima, and G. Hatakoshi, "High temperature ($90°C$) CW operation of 646nm InGaAlP laser containing multiquantum barrier," *Elect. Lett.*, vol. 28, pp. 150–151, Jan. 1992.

[16] J. Rennie, M. Okajima, K. Itaya, and G. Hatakoshi, "Measurement of the barrier height of a multiple quantum barrier (MQB)," *IEEE J. Quant. Elect.*, vol. 30, Dec. 1994.

[17] A. P. Morrison, J. D. Lambkin, E. O'Sullivan, and S. Fahy, "Simple effective mass model to include the effects of , $-X$ mixing in multiquantum barriers," *Opt. Eng.*, vol. 33, pp. 3926–3930, Dec. 1994.

[18] A. P. Morrison, J. D. Lambkin, E. O'Sullivan, and S. Fahy, "Design of a Multi-Quantum Barrier using an Extended Effective Mass Model to include the effects of , $-X$ Mixing," in *Proceedings of the 18^{th} European Workshop on Compound Semiconductor Devices and Integrated Circuits (WOCSDICE), Kinsale, Ireland.*, p. 91, May 1994.

[19] J. D. Lambkin, A. P. Morrison, L. Considine, G. M. O'Connor, C. J. McDonagh, E. Daly, and T. J. Glynn, "Energy-band structure of type I and type II InGaP/InAlP short period superlattices," *22^{nd} International Conference on The Physics of Semiconductors*, vol. 1, pp. 707–710, Aug. 1994.

[20] A. P. Morrison, L. Considine, S. Walsh, N. Cordero, J. D. Lambkin, G. M. O'Connor, E. M. Daly, T. J. Glynn, and C. J. van der Poel, "Photoluminescence Investigation of the Carrier Confining Properties of MultiQuantum Barriers." In preparation for IEEE J. Quant. Electronics, 1996.

[21] A. P. Morrison, J. D. Lambkin, C. J. van der Poel, and A. Valster, "Measuring the , $-X$ Transition in AlGaInP using n-i-n Diodes." In Preparation, 1996.

[22] A. P. Morrison, J. D. Lambkin, C. J. van der Poel, and A. Valster, "Electron Transport in n-i-n Diodes with AlGaInP Intrinsic Barriers." In Preparation, 1996.

[23] A. P. Morrison, J. D. Lambkin, C. J. van der Poel, and A. Valster, "Systematic Measurement of the Barrier Height of the MultiQuantum Barrier Intrinsic Region in AlGaInP n-i-n Diodes." In Preparation, 1996.

[24] J. D. Lambkin, A. P. Morrison, C. J. van der Poel, and A. Valster, "MultiQuantum Barriers in Bulk Double Heterostructure Visible Laser Diodes," in *20^{th} Workshop on Compound Semiconductor Devices and Integrated Circuits (WOCSDICE), Vilnius, Lithuania.*, May 1996.

[25] A. P. Morrison, J. D. Lambkin, C. J. van der Poel, and A. Valster, "Performance of MultiQuantum Barriers in Bulk Double Heterostructure Visible Laser Diodes as a Function of Temperature," in *Conference on Lasers and Electro-Optics Europe, Hamburg, Germany.*, p. 50, IEEE, Sept. 1996.

[26] P. Bhattacharya, *Semiconductor Optoelectronic Devices.* Prentice Hall International Editions, 1994.

[27] H. C. Casey and M. B. Panish, *Heterostructure Lasers Part A: Fundamental Principles.* Academic Press, Inc., 1978.

[28] A. Kikuchi, K. Kishino, and Y. Kaneko, "High optical quality GaInP and GaInP/AlInP double heterostructure lasers grown on GaAs substrates by gas-source molecular-beam epitaxy," *J. Appl. Phys.*, vol. 66, pp. 4557–4559, Nov. 1989.

[29] D. P. Bour, *Quantum Well Lasers*, ch. 9, pp. 415–460. Academic Press, Inc., 1994. edited by Peter S. Zory, Jr.

[30] T. Takagi, F. Koyama, and K. Iga, "Potential barrier height analysis of AlGaInP multi-quantum barrier (MQB)," *Jpn. J. Appl. Phys.*, vol. 29, pp. L1977–L1980, Nov. 1990.

[31] D. P. Bour, D. W. Treat, R. L. Thornton, R. S. Geels, and D. F. Welch, "Drift leakage current in AlGaInP quantum-well lasers," *IEEE J. Quant. Elect.*, vol. 29, pp. 1337–1342, May 1993.

[32] H. Fujii, K. Endo, and H. Hotta, "Improvement of multiquantum-barrier effect by layer-thickness modulation," *Appl. Phys. Lett.*, vol. 64, pp. 3479–3481, June 1994.

[33] K. Itaya, H. Sugawara, and G. Hatakoshi, "InGaAlP visible light laser diodes and light emitting diodes," *J. Cryst. Growth*, vol. 138, pp. 768–775, 1994.

[34] A. T. Meney, A. D. Prins, A. F. Phillips, J. L. Sly, E. P. O'Reilly, D. J. Dunstan, A. R. Adams, and A. Valster, "Determination of the band structure of disordered AlGaInP and its influence on visible-laser characteristics," *IEEE J. of Selected Topics in Quant. Elect.*, vol. 1, pp. 697–706, June 1995.

[35] H. Hamada, M. Shono, S. Honda, R. Hiroyama, K. Yodoshi, and T. Yamaguchi, "AlGaInP visible laser diodes grown on misoriented substrates," *IEEE J. Quant. Elect.*, vol. 27, pp. 1483–1490, June 1991.

[36] T. Tanaka, H. Yanagisawa, S. Yano, and S. Minagawa, "High-temperature operation of 637nm AlGaInP MQW laser diodes with quaternary QWs grown on misoriented substrates," *Elect. Lett.*, vol. 29, pp. 24–26, Jan. 1993.

[37] K. Nakano, A. Toda, T. Yamamoto, and A. Ishibashi, "Effects of ordering on the operation of AlGaInP lasers grown by metalorganic chemical vapor deposition," *Appl. Phys. Lett.*, vol. 61, pp. 1959–1961, Oct. 1992.

[38] A. Kikuchi and K. Kishino, "Remarkable reduction of threshold current density by substrate misorientation effects in 660nm visible light lasers with GaInP bulk active layers," *Appl. Phys. Lett.*, vol. 60, pp. 1046–1048, Mar. 1992.

[39] L. Esaki and R. Tsu, "Superlattice and negative differential conductivity in semiconductors," *IBM J. Res. Develop.*, pp. 61–65, Jan. 1970.

[40] R. Tsu and L. Esaki, "Tunneling in a finite superlattice," *Appl. Phys. Lett.*, vol. 22, pp. 562–564, June 1973.

[41] G. Lenz and J. Salzman, "Bragg confinement of carriers in a quantum barrier," *Appl. Phys. Lett.*, vol. 56, pp. 871–873, Feb. 1990.

[42] A. Kikuchi, Y. Kaneko, I. Nomura, and K. Kishino, "Room temperature continuous wave operation of GaInP/AlInP visible-light laser with GaInP/AlInP superlattice confinement layer grown by gas source molecular beam epitaxy," *Elect. Lett.*, vol. 26, pp. 1668–1670, Sept. 1990.

[43] T. Takagi, F. Koyama, and K. Iga, "Design and photoluminescence study on a multiquantum barrier," *IEEE J. Quant. Elect.*, vol. 27, pp. 1511–1519, June 1991.

[44] T. Takagi, F. Koyama, and K. Iga, "Photoluminescence study of electron wave confinement in multi-quantum barrier (MQB)," *Jpn. J. Appl. Phys.*, vol. 29, pp. L1969–L1972, Nov. 1990.

[45] T. Takagi, F. Koyama, and K. Iga, "Electron-wave reflection by multi-quantum barrier in n-GaAs/i-AlGaAs/n-GaAs tunnelling diode," *Appl. Phys. Lett.*, vol. 59, pp. 2877–2879, Nov. 1991.

[46] T. Takagi, F. Koyama, and K. Iga, "Electron wave reflection by multiquantum barrier," *Jpn. J. Appl. Phys.*, vol. 31, pp. 197–200, Feb. 1992.

[47] C. B. Duke, *Tunneling in Solids.* Solid State Physics: Advances in Research and Applications, Academic Press, 1969.

[48] S. T. Yen, C. M. Tsai, C. P. Lee, and D. C. Liu, "Enhancement of electron-wave reflection by superlattices with multiple stacks of multiquantum barriers," *Appl. Phys. Lett.*, vol. 64, pp. 1108–1110, Feb. 1994.

[49] S. T. Yen, C. P. Lee, C. M. Tsai, and H. R. Chen, "Influence of X-valley superlattice on electron blocking by multiquantum barriers," *Appl. Phys. Lett.*, vol. 65, pp. 2720–2722, Nov. 1994.

[50] L. D. Landau and E. M. Lifshitz, *A Shorter Course of Theoretical Physics Volume 2: Quantum Mechanics*, vol. 2. Pergamon Press, 2 ed., 1985.

[51] S. Datta, *Quantum Phenomena*, vol. VIII of *Modular Series on Solid State Devices.* Addison-Wesley Publishing Company, 1989.

[52] A. Furuya and H. Tanaka, "Superposed multiquantum barriers for InGaAlP heterojunctions," *IEEE J. Quantum Elect.*, vol. 28, pp. 1977–1982, Oct. 1992.

[53] J. Salzman, G. Lenz, E. Baruch, and E. Finkman, "Bragg confinement of carriers in a shallow quantum well," *Appl. Phys. Lett.*, vol. 59, pp. 1858–1860, Oct. 1991.

[54] E. E. Mendez, F. Aguiló-Rueda, and J. M. Hong, "Temperature dependence of the electronic coherence of GaAs-GaAlAs superlattices," *Appl. Phys. Lett.*, vol. 56, pp. 2545–2547, June 1990.

[55] T. Takagi, F. Koyami, and K. Iga, "Modified multiquantum barrier for 600 nm range AlGaInP lasers," *Elect. Lett.*, vol. 27, pp. 1081–1082, June 1991.

[56] J. M. Dallesasse, W. E. Plano, D. W. Nam, K. C. Hsieh, J. E. Baker, and N. H. Jr., "Impurity-induced layer disordering in $In_{0.5}(Al_xGa_{1-x})_{0.5}P - InGaP$ quantum-well heterostructures: Visible-spectrum-buried heterostructure lasers," *J. Appl. Phys.*, vol. 66, pp. 482–487, July 1989.

[57] C. J. van der Poel, "Bandgap equation for $(Al_xGa_{1-x})_{0.5}In_{0.5}P$." Private Communication, Nov. 1994.

[58] S. P. Najda, A. H. Kean, M. D. Dawson, and G. Duggan, "Optical measurements of electronic bandstructure in AlGaInP alloys grown by gas source molecular beam epitaxy," *J. Appl. Phys.*, vol. 77, pp. 3412–3415, Apr. 1995.

[59] C. T. H. F. Liedenbaum, A. Valster, A. L. G. J. Severens, and G. W. 't Hooft, "Determination of the GaInP/AlGaInP band offset," *Appl. Phys. Lett.*, vol. 57, pp. 2698–2700, Dec. 1990.

[60] K. F. Brennan and P.-K. Chiang, "Calculated electron and hole steady-state drift velocities in lattice matched GaInP and AlGaInP," *J. Appl. Phys.*, vol. 71, pp. 1055–1057, Jan. 1992.

[61] E. O'Sullivan, "Multichannel barrier transmission," final year degree project, Department of Physics, University College, Cork., Mar. 1994.

[62] P. Tangney, "The effect of carrier decay on transmission through semiconductor multiquantum barriers," final year degree project report, Department of Physics, University College, Cork., Mar. 1996.

[63] H. A. Macleod, *Thin Film Optical Filters.* Adam Hilger, 1969.

[64] A. C. Marsh, "Electron tunnelling in GaAs/AlGaAs heterostructures," *IEEE J. Quantum Electron.*, vol. QE-23, no. 4, pp. 371–376, 1987.

[65] A. C. Marsh and J. C. Inkson, "An empirical pseudopotential analysis of (100) and (110) $GaAs/Al_xGa_{1-x}As$ heterojunctions," *J. Phys. C: Solid State Phys.*, vol. 19, pp. 43–52, 1986.

[66] A. C. Marsh and J. C. Inkson, "Electron scattering from heterojunctions," *J. Phys. C: Solid State Phys.*, vol. 17, pp. 6561–6571, 1984.

[67] M. U. Erdoğan, K. W. Kim, M. A. Stroscio, and M. Dutta, "Extension of the Kronig-Penney model for , $-X$ mixing in superlattices," *J. Appl. Phys.*, vol. 74, pp. 4777–4779, Oct. 1993.

[68] M. R. Islam, R. V. Chelakara, and R. D. Dupuis, "InAlP/InGaP strain-modulated aperiodic superlattice heterobarrier for enhanced electron confinement in visible ($\lambda \sim$ 650nm) light-emitting devices," *Appl. Phys. Lett.*, vol. 67, pp. 2057–2059, Oct. 1995.

[69] E. M. Daly, T. J. Glynn, J. D. Lambkin, L. Considine, and S. Walsh, "Behaviour of $In_{0.48}Ga_{0.52}P/(Al_{0.2}Ga_{0.8})_{0.52}In_{0.48}P$ quantum-well luminescence as a function of temperature," *Phys. Rev. B*, vol. 52, pp. 4696–4699, Aug. 1995.

[70] J. D. Lambkin, D. J. Dunstan, K. P. Homewood, L. K. Howard, and M. T. Emeny, "Thermal quenching of the photoluminescence of InGaAs/GaAs and InGaAs/AlGaAs strained-layer quantum wells," *Appl. Phys. Lett.*, vol. 57, pp. 1986–1988, Nov. 1990.

[71] J. D. Lambkin, L. Considine, S. Walsh, G. M. O'Connor, C. J. McDonagh, and T. J. Glynn, "Temperature dependence of the photoluminescence intensity of ordered and disordered $In_{0.48}Ga_{0.52}P$," *Appl. Phys. Lett.*, vol. 65, pp. 73–75, July 1994.

[72] O. Madelung, ed., *Landolt-Bornstein New Series*, vol. 22a. Springer, Berlin, 1992.

[73] M. Vening, D. J. Dunstan, and K. P. Homewood *Phys. Rev. B*, vol. 48, p. 2412, 1993.

[74] H. Chaabane and J. C. Bourgoin, "Role of defects on electron transport through semiconductor barriers," *J. Appl. Phys.*, vol. 76, pp. 315–318, July 1994.

[75] H. Chaabane, M. Zazoui, J. C. Bourgoin, and V. Donchev, "Electronic transport through semiconductor barriers," *Semicond. Sci. Technol.*, vol. 8, pp. 2077–2084, 1993.

[76] H. Chaabane and J. C. Bourgoin, "Irradiation effect on electron transport through GaAlAs barriers," *Appl. Phys. Lett.*, vol. 64, pp. 1006–1008, Feb. 1994.

[77] S. S. Lu, K. Lee, M. I. Nathan, and S. L. Wright, "Resonant indirect Fowler-Nordheim tunneling in $Al_{0.8}Ga_{0.2}As$ barrier," *Appl. Phys. Lett.*, vol. 58, pp. 266–268, Jan. 1991.

[78] B. Zimmerman, E. Marclay, M. Ilegems, and P. Guéret, "Self-consistent calculations of tunneling currents in $n^+ - GaAs/i - Al_xGa_{1-x}As/n^+ - GaAs$ structures and comparison with measurements," *J. Appl. Phys.*, vol. 64, pp. 3581–3588, Oct. 1988.

[79] M. Rossmanith, J. Leo, and K. von Klitzing, "Model of , to X transition in thermally activated tunnel currents across $Al_xGa_{1-x}As$ single barriers," *J. Appl. Phys.*, vol. 69, pp. 3641–3645, Mar. 1991.

[80] T. W. Hicknott, p. M. Solomon, R. Fischer, and H. Morkoç, "Negative charge, barrier height, and the conduction-band discontinuity in $Al_xGa_{1-x}As$ capacitors," *J. Appl. Phys.*, vol. 57, pp. 2844–2853, Apr. 1985.

[81] D. Arnold, A. Ketterson, T. Henderson, J. Klem, and H. Morkoç, "Electrical characterization of GaAs/AlGaAs semiconductor-insulator-semiconductor capacitors

and application to the measurement of the GaAs/AlGaAs band-gap discontinuity," *J. Appl. Phys.*, vol. 57, pp. 2880–2885, Apr. 1985.

[82] M. Lenzlinger and E. H. Snow, "Fowler-Nordheim Tunnelling into Thermally Grown SiO_2," *J. Appl. Phys.*, vol. 40, pp. 278–283, Jan. 1969.

[83] M. F. C. Schemmann, *Waveguiding in High Power Short Wavelength Semiconductor Lasers*. PhD thesis, Technische Universiteit Eindhoven, 1994.

[84] S. H. Hagen, A. Valster, M. J. B. Boermans, and J. van der Heyden, "Investigation of the temperature dependence of the threshold current density of GaInP/AlGaInP double-heterostructure lasers," *Appl. Phys. Lett.*, vol. 57, pp. 2291–2293, Nov. 1990.

[85] J. D. Lambkin, "Discussions on the operation of MQB structures." Private Communication, Oct. 1996.